Numerical Modelling and Experimental Measurement of the Temperature Distribution in a Rolling Tire

by

Johannes Christoffel Maritz

Thesis presented in partial fulfilment of the requirements for the degree of Master of Engineering (Mechanical) in the Faculty of Engineering at Stellenbosch University

Supervisor: Prof. G. Venter

March 2015

Declaration

By submitting this thesis electronically, I declare that the entirety of the work contained therein is my own, original work, that I am the sole author thereof (save to the extent explicitly otherwise stated), that reproduction and publication thereof by Stellenbosch University will not infringe any third party rights and that I have not previously in its entirety or in part submitted it for obtaining any qualification.

Signature: .....
J.C. Maritz

Date: 2014/12/02 .....

Abstract

Rubber is the main component of the pneumatic tire. When rubber is put under cyclic loading, like when a tire is rolled, heat is generated and stored in the rubber, due to hysteresis. Heat stored in the tire is increased by factors like under-inflation, overloading, speeding and defects in the tire. The heat causes high temperatures in the tire due to the poor thermal conductivity of rubber. When the temperature in the rubber increases to 185 °C, pyrolysis and thermo-oxidation starts and can cause the tire to eventually explode.

A numerical model of a rolling passenger vehicle tire was developed to calculate the temperature distribution inside the tire and analyse the effect of different operating conditions on the temperature. Operating conditions include loading, inflation pressure, rolling velocity and ambient temperature. The tire was modelled by a single rubber type, using the Mooney-Rivlin material model. The bead wire was modelled using an isotropic material model, while the body and steel cord plies were modelled as rebars. The cavity, used to inflate the tire, included the pressure increase due to the volume change, when the tire is loaded.

The numerical model was validated using experimental data from tests done on an actual tire. These tests included deformation and contact stress analysis, as well as surface temperature measurements.

Numerical results showed an increase in temperature when the load, rolling velocity and the ambient temperature were increased, as well as when the inflation pressure was decreased. The trends of the numerical data matched the trends of the experimental data. However, the values of the numerical model were not consistent with the experimental data due to material properties from literature being used to model the tire.

Opsomming

Rubber is die hoofkomponent in die pneumatiese band. As rubber onder 'n sikliese las geplaas word, soos wanneer 'n band rol, word hitte gegenereer en in die rubber gestoor as gevolg van histerese. Die hitte wat in die band gestoor word, word verhoog deur faktore soos lae inflasiedruk, hoë las, hoë rol snelhede en gebreke in die band. Die hitte veroorsaak hoë temperature in die band weens die swak termiese geleiding van rubber. As die temperatuur in die band hoër as 185 °C raak, vind piroliese en termo-oksidasie plaas en die band kan uiteindelik ontplof.

'n Numeriese model van 'n passasiersmotorband is ontwikkel om die temperatuurverspreiding te bepaal, asook om die effek van verskillende werkstoestande op die temperatuur te analiseer. Die band is gemodelleer met een tipe rubber en die Mooney-Rivlin materiaal-model is gebruik om die rubber te beskryf. Die spanrand van die band is deur 'n isotropiese materiaalmodel gemodelleer, terwyl die hoof- en staalkoordlae as bewapening gemodelleer is. Die holte wat gebruik word om die band op te blaas, neem die druk toename as gevolg van die verandering in volume in ag wanneer die band belas word.

Die numeriese model was bekragtig met eksperimentele data wat deur toetse op 'n werklike band onttrek is. Die toetse sluit die volgende in: vervorming- en kontakspanninganalises, asook temperature wat op die oppervlak van die band gemeet is.

Die numeriese resultate toon 'n toename in temperatuur wanneer die las, rolsnelheid en omgewingstemperatuur verhoog word, asook waneer die inflasiedruk verlaag word. Die numeriese model se tendense stem ooreen met die eksperimentele data, maar die waardes van die numeriese model is nie in ooreenstemmig met die eksperimentele data nie. Die verskil is as gevolg van die materiaaleienskappe wat uit die literatuur geneem is.

Acknowledgements

I would like to express my sincere gratitude to the following people and organisations:

- Anglo American for the financial backing for this project
- Prof. Gerhard Venter for his guidance and knowledge
- Department of Mechanical and Mechatronic Engineering staff for the help with the test and calibration equipment

Contents

List of Figures

List of Tables

Chapter 1

Introduction

1.1 Background

The main component of the pneumatic tire is rubber. Rubber is supported by body plies and other materials to carry the load and withstand the impacts on the tire. Rubber is an elastic material with hyper-viscoelastic material properties. When the rubber is put under cyclic loading, a phenomenon known as hysteresis occurs. Hysteresis happens when the rubber releases less energy during relaxing than what it received when it was stretched. The difference in energy is known as hysteresis loss and is stored in the rubber as heat. The heat generated in the rubber increases with larger deformations and faster cyclic loading.

Vehicle fuel consumption is also linked to the hysteresis loss. When the hysteresis loss is high, the fuel consumption increases due to the rolling resistance of the tire being higher. It is possible to decrease this rolling resistance and ultimately the fuel consumption of the vehicle by using different types of rubber in the tire.

Heat generation in the tire is increased by parameters like under-inflation, overloading, speeding or defects in the tire. The increase in heat generation leads to higher temperatures in the tire due to the poor thermal conductivity of rubber. If the temperature in the tire rise above 185 °C, two chemical degrading processes known as pyrolysis and thermo-oxidation start (Chen, Chen and Tong, 2001). Pyrolysis and thermo-oxidation are the irreversible chemical decomposition of materials under the sole action of heat. However, pyrolysis happens in the absence of oxygen, while thermo-oxidation happens in the presence of oxygen, but not enough for combustion to start (Dolez, Nohile, Ha Anh, Vu-Khanh, Benoît and Bellavigna-Ladoux, 2008).

Gases produced by the two processes lead to an increase in inflation pressure, which can lead to a tire blow-out (burst). However, if the concentration of the gases is sufficient, the inflation pressure and temperature are equal to or above the auto-ignition pressure and temperature of the gases and the oxygen

concentration is above 5,5 %, the tire could explode (Benoît, Lafrance, Malo and Baron, 2009). Therefore, the calculation of these temperatures under the different operating parameters are important in the transporting and mining industry, due to the cost of the tires, the machines they could destroy and the safety hazard that goes with the explosion of tires.

The numerical modelling of tires is becoming more popular, not only for the advantages it has for tire manufacturers, but also in other research areas like vehicle dynamics. The numerical modelling is more cost-effective than actual tests and is also less time consuming. Numerical models also give results on the inside of the tire geometry, while it is not always possible to measure these results with actual tests. This is advantageous, because the high temperature can be inside the tire geometry. Finite element software, used to model the structure of the tire, is also becoming more advanced in the modelling of complex problems, making it easier to include all the effects that have an influence on the mechanics inside the tire.

1.2 Project Description

Explosion of haul truck tires at some of Anglo American's (Anglo) mines raised a concern over the safety hazard the tires hold for employees when the tires overheat. Anglo approached Stellenbosch University to do numerical modelling of the haul truck tires in order to determine under which operating conditions the temperature in the tire rises to critical values.

The first step in the development of a numerical model for the haul truck tire was to develop a base model for a passenger vehicle tire. The base model had to be able to determine the temperature distribution in the tire, using material properties from literature. The second step was to compare the base numerical model against experimental data generated from actual tire tests. The comparison of the base model revealed if there were any deficiencies that need to be addressed in order to generate more accurate results. Only these two steps were completed in this project.

The third step will be to determine the properties of the materials used in the manufacturing of the tire. The material properties will then be used in the base model, with the recommendations made for any deficiencies, to generate a representative model of the passenger vehicle tire. The last step is to scale the representative model to the size of the haul truck tire and do numerical simulations under different operating conditions.

1.3 Project Objectives

The project has two outcomes namely:

1. Generate a numerical model of a passenger vehicle tire that can determine the temperature distribution in the tire. Temperatures should be determined for a set of different operating conditions, using material properties from literature. The model should represent the setup used for the actual tests in order to do the compare the results. Operating conditions that should be accounted for, includes the inflation pressure of the tire, the load applied to the tire and the rolling velocity of the tire as well as the ambient temperature.

2. Compare the numerical data against experimental data collected from tests on an actual tire. Experimental data used for comparison, includes the deformation of the tire, the contact stress between the tire and road surface and the temperature on the internal and external surface of the tire. The experimental data should be generated under the same conditions as the numerical simulations.

1.4 Project Overview

In order to reach the objectives set for this project, the following steps were followed:

- A literature study on numerical modelling of tires was done
- Geometry of the actual tire and rim was measured and used to create a 2-D mesh of the tire
- A base numerical model was generated and simulations were run for different operating conditions
- Measuring devices on the test bench and thermocouples were calibrated
- The test bench was used to collect experimental data
- Data from the numerical model were compared to experimental
- Conclusions and recommendations were made

The literature study in Chapter 2 will present research that has already been done on the numerical modelling of tires and includes the different approaches followed, the effects of different operating conditions and the effects of different materials and designs.

Chapter 3 looks at the modelling complications that should be considered before the numerical modelling of a tire can begin. This includes material nonlinearity, nonlinear boundary conditions, as well as the complex structure of the tire.

Chapter 4 describes the material model used for the modelling of rubber. The chapter also shows how the hysteresis coefficient, total strain energy density and the heat generation rate is calculated.

Chapter 5 describes the setup of the numerical model and the material properties used in the model. The boundary conditions and simulation parameters used in the numerical modelling is also described.

Chapter 6 shows the results from the numerical model as well as observations made from the results. The effects of the different operating conditions are also discussed.

Chapter 7 describes the experimental tests done on the tire, experimental data gathered, as well as the comparison with the numerical results. The shortcomings of the numerical model are also addressed in this chapter.

The final conclusion of the project and recommendations made for further research on the numerical modelling of tires are discussed in Chapter 8.

Chapter 2

Literature Review

This chapter aims to provide the reader with a better understanding of the tire, as well as previous research done on the numerical modelling of tires. The components of the tire's construction and their functions will be discussed, followed by various ways in which modelling of tires have been approached. This includes the effect of different operating parameters, material properties and designs on the deformation and heat generation inside the tire.

2.1 Tire Construction

Construction of the pneumatic tire is complex and consists of different materials carrying the load, maintaining the shape and sealing the tire. These components are shown in Figure 2.1 and can be divided into four sections, namely: tread, shoulder, sidewall and bead.

The body ply, also called the carcass, is the main load carrier of the tire and typically consists of rubber-coated fabric, like polyester or nylon. The body plies run from bead to bead in a radial direction. It turns-up around the bead and back to the top of the bead filler, where the end points are secured. Body plies hold the shape of the tire while it is inflated and absorb the impact and forces from the road. The tire in Figure 2.1 has two body plies, but this can vary from tire to tire, depending on the load-carrying capability of the tire.

Two steel belt plies are located under the tread area, at opposite angles to one another and on top of the body plies (Gent and Walter, 2006). These plies consist of rubber-laminated steel wire sheets. They provide stiffness in the tread area and protect the body plies from damage. The ride quality and handling characteristics of the tire can be varied by changing the angles and the width of the belt plies (Gent and Walter, 2006).

Some tires, especially high speed tires, have a nylon cap ply wrapped circumferentially on top of the steel belt plies. The cap ply reinforces the tire further as it prevents expansion due to centrifugal forces (Gent and Walter, 2006).

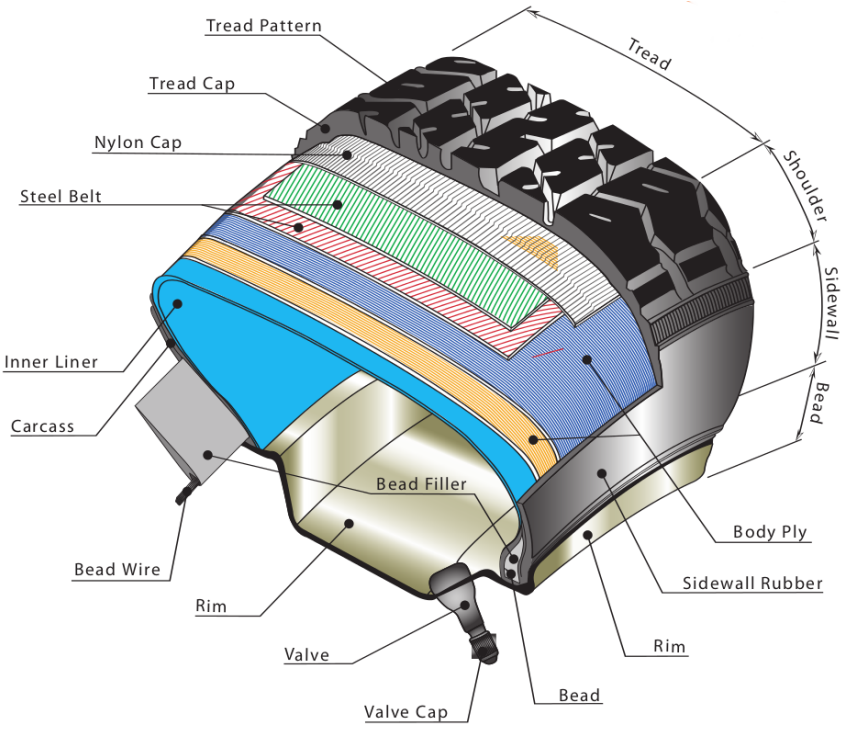

Figure 2.1: Radial tire construction (Maxxis, 2014)

The inner liner is a rubber layer consisting of low permeable rubber on the inside of a tubeless tire. It replaces the tube in a tubeless tire; therefore the function of the inner liner is to retain air when the tire is inflated.

The bead is the part of the tire in contact with the rim and is fabricated from a bead wire, an abrasion gum strip and bead filler. The bead wire secures the tire to the rim and maintains the shape of the tire. It consists of wound-up steel wire that forms a high strength cable. The abrasion gum strip is a rubber layer between the body plies and the rim, where the body plies turn-up around the bead wire. This provides an airtight seal between the tire and the rim (Gent and Walter, 2006). The bead filler consists of stiff rubber and fills the void between the inner body plies and the turned-up body plies. The bead filler assists in handling and stability characteristics of the tire (Gent and Walter, 2006).

The sidewall is the most flexible part of the tire and consists of flexible rubber and the body plies. The sidewall protects the body plies from abrasion and impact as well as flex fatigue (Gent and Walter, 2006). The sidewall also serves as the information placement area, i.e. tire branding, tire size etc.

The tire shoulder is the thickest part of the tire and consists of rubber and body plies, as well as steel belt plies, which end at the shoulder. It forms the transition from the flexible sidewall to the stiffer tread. The shoulder protects the body plies from external shocks and damage.

The tread is the component that comes in contact with the road. It provides

traction and durability, defines tire life and protects the body plies. The tread is fabricated from durable rubber that is formulated to provide a balance between wear, traction, handling and rolling resistance (Gent and Walter, 2006). Tires designed for different conditions have different tread patterns to provide better traction, better durability and reduce pattern noise. Pattern noise is the noise generated by the tire pattern while it is rolling.

2.2 Numerical Modelling

The first application of numerical modelling of tires dates back to the early 1970s (Ghoreishy, 2008). Since then, different approaches have been used to model tires numerically. The factors contributing to these different approaches included the desired results, computational power available, software packages and the challenges of modelling the geometry of the tire.

2.2.1 Numerical Modelling Approaches

Numerical modelling of tires has been approached by a number of different techniques in an attempt to solve the rolling of the tire numerically. These techniques are used to simplify the modelling of the tire geometry and to save on computational time when solving the rolling tire model as well as the thermal analysis of the tire.

In most of the models it is assumed the tire is fabricated from only one type of rubber (Lin and Hwang, 2004; Cho, Lee, Jeong, Jeong and Kim, 2013; Tang, Johnson, Smith and Felicelli, 2014). This approach was followed due to the material properties of rubber being difficult to determine. This also simplifies the meshing of the tire geometry. However, Kováč and Krmela (2012) modelled the tire with three types of rubber. In their case, the sidewall, inner liner and bead filler was modelled by the same rubber. The tread and base, located under the tread, were modelled using different rubbers. This made the meshing of the model more complex, as the elements had to follow the boundary locations of the different rubbers. However, this influenced the deformation of the model because the sidewall rubber is more flexible than, for example, the tread rubber. Therefore, the deformation of the tire using Kováč and Krmela's (2012) model will be more accurate.

The placement of the plies in the tire geometry during meshing is a difficultly. The easiest and most common technique used to solve this difficulty is to place the plies on the inside of the rubber elements as a layer of quad elements (Lin and Hwang, 2004; Tang *et al.*, 2014). This influences the deformation of the tire because the placement of the plies is not at the correct location, the plies are modelled using isotropic material properties and the orientation of the plies can not be specified. Another option is to place the plies as composite shells between the rubber elements, as was done by Cho *et al.*

(2013). This makes the meshing of the geometry more complicated when the plies are placed at their exact locations. However, the composite shell describes the behaviour of the plies better, since only the individual ply fibers are modelled using isotropic material properties and the orientation of the plies can be specified in the composite. Kováč and Krmela (2012) used the `Insert` option in MSC.Marc to place the plies, modelled as `Rebar` elements inside the rubber elements. This was the easiest way to model the plies and it ensured that the plies are at the correct location in the model.

The bead wire was modelled using a single element by Lin and Hwang (2004) and Kováč and Krmela (2012), as shown in Figure 2.2a. However, to fit in with their mesh, Cho *et al.* (2013) modelled the bead wire using four elements, as seen in Figure 2.2b. Furthermore, the bead region, where the bead wire is located, was completely ignored by Tang *et al.* (2014) for simplification of their geometry.

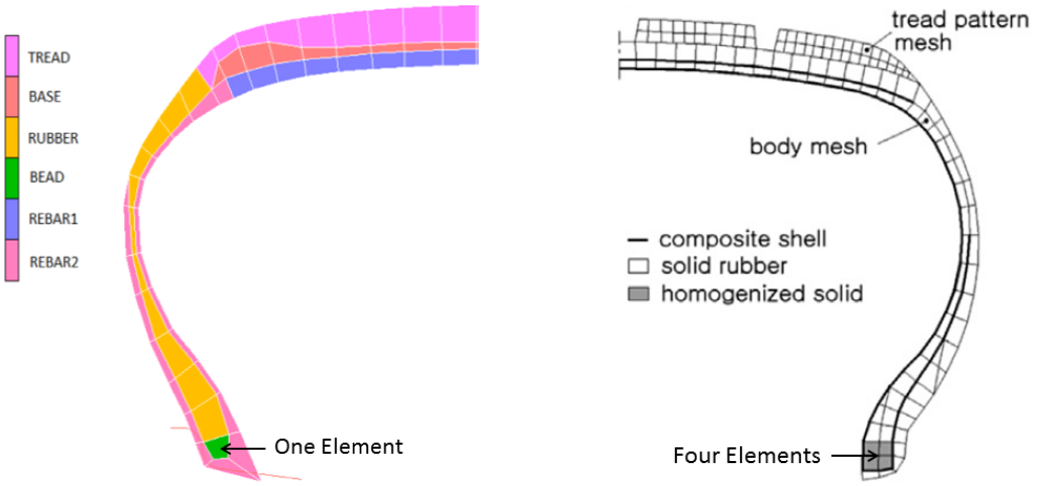

(a) Single element bead wire (b) Four element bead wire

Figure 2.2: 2-D mesh with different bead wire configurations (Kováč and Krmela, 2012; Cho *et al.*, 2013)

Modelling the tread pattern of the tire is probably the most difficult part in the meshing process. That is why Lin and Hwang (2004) and Kováč and Krmela (2012) decided to assume the tire has a smooth tread. This simplifies the meshing of the geometry substantially, although it will add more rubber to the tire. This extra rubber will generate more heat and increase the temperature, when a thermal analysis is done. Tang *et al.* (2014) used a model with only circumferential grooves in the tread area. This made the meshing a bit more complicated, although it resembled the actual tire more accurately. The complete tread pattern was modelled by Cho *et al.* (2013), as shown in Figure 2.3. This was done using 3-D periodic meshes, as displayed in Figure 2.3a, that is duplicated to complete the tire, as shown in Figure 2.3b. This is more

complicated to mesh, but will be the most accurate when a thermal analysis is done.

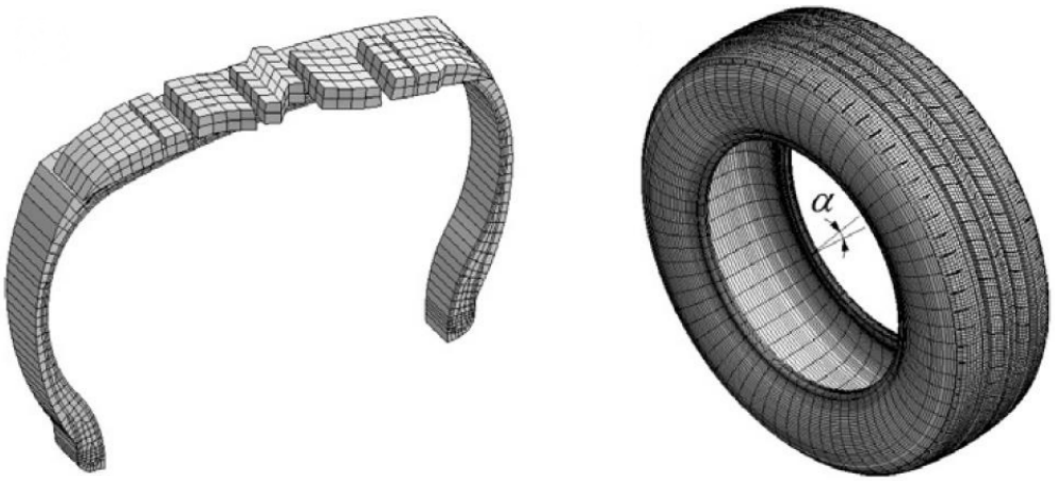

(a) 1-sector patterned mesh (b) 3-D patterned tire mesh

Figure 2.3: 3-D periodic-patterned tire mesh (Cho *et al.*, 2013)

Next, looking at the different techniques used to solve the rolling tire model, Lin and Hwang (2004) divided the dynamic rolling of the tire into two steps to save on computational time. They modelled half of the 3-D tire model, due to symmetry, as shown in Figure 2.4. The loading analysis was done first by inflating the tire to a specific pressure and then applying the load on the tire using load control (as shown in Figure 2.4a). Thereafter, the rolling analysis was done using the displacement of the tire in the loading analysis to displace the road and apply the force. The road is also given a velocity, as shown in Figure 2.4b that rotates the tire, due to the friction between the road and the tire.

According to Lin and Hwang (2004) this technique saves computational time due to displacement control converging faster than the load control. A drawback on the displacement control was that it does not reflect "true" dynamic results, because the force on the tire increased due to rolling resistance (Lin and Hwang, 2004).

Lin and Hwang (2004) solved the steady-state thermal analysis for a half 2-D axisymmetric model of the tire. The heat generated in each element was calculated using the total strain energy density from the rolling analysis, the hysteresis coefficient and the rolling frequency of the tire. Furthermore, the inside of the tire model was insulated, while there was forced convection, which was a function of the rolling velocity applied on the outside of the model. The boundary conditions for the thermal analysis are shown in Figure 2.5. The thermal analysis was executed to determine the temperature distribution in the tire.

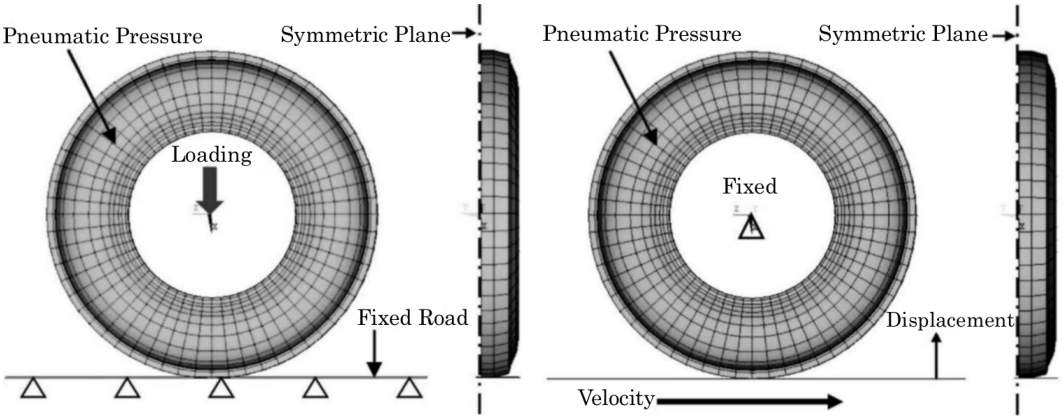

(a) Loading analysis (b) Rolling analysis

Figure 2.4: Boundary conditions for dynamic rolling analysis (Adapted from Lin and Hwang, 2004)

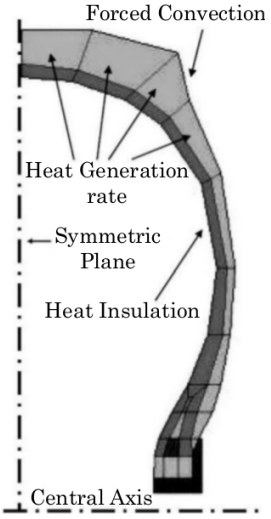

Figure 2.5: Boundary condition for the 2-D thermal analysis (Adapted from Lin and Hwang, 2004)

A similar technique was followed by Kováč and Krmela (2012) to conduct a vertical loading analysis on a tire model in contact with a rigid surface. They started with a full 2-D axisymmetric model to solve the mounting and inflation of the tire. Next, they expanded the 2-D axisymmetric model to a 3-D model with the `Axisymmetric Model To 3-D` expand option in MSC.Marc. The results of the 2-D axisymmetric model were used as an initial condition for the 3-D model. Kováč and Krmela (2012) also used position control to apply the load on the tire. They only recorded the stress and deformation in the tire.

Tang *et al.* (2014) used a technique similar to the previous techniques to solve a rolling tire model. They used a half 2-D axisymmetric model to inflate

the tire. Next, the 2-D axisymmetric model was revolved to a half 3-D tire model, using the `Revolve` feature in Tire Wizard, a plug-in to ABAQUS. The pressure, load and contact condition were applied on the tire model, after which the `Steady State Transport` option of Tire Wizard was used to evaluate the tire under steady-state rolling conditions (Tang *et al.*, 2014).

Tang *et al.* (2014) also did a thermal analysis to determine the temperature distribution in the tire. The heat generation rate in each element was calculated for the 2-D axisymmetric thermal analysis using the elastic strain energy density calculated from the steady-state rolling analysis, the hysteresis coefficient and the rolling frequency of the tire (Tang *et al.*, 2014). They ignored the heat generated by the friction between the tire and the road.

Cho *et al.* (2013) first inflated the 3-D tire model, consisting of 3-D periodic sections, to a specified pressure, with all the nodes that would be in contact with the rim fixed. They then applied a load to the rigid body that came in contact with the tire to deform it. Cho *et al.* (2013) developed an in-house dissipation module to determine the hysteresis loss, rolling resistance and heat generation rate during the rolling of a tire. As a quick summary of the steps used to calculate the hysteresis loss and heat generation rate, they first approximated the strain along a circular path for one 3-D periodic sector of the tire, using the 3-D static contact analysis, neglecting the effect of rolling. Next, they determined the half-amplitude of the six strain components at the Gaussian points of the elements in the sector, for one revolution and averaged it over the element. They then calculated the maximum principal strain value from the element-wise averaged half-amplitude strain components within one sector. This is done by solving the characteristic polynomial of the principal strains using the well-known closed-form formulas (Cho *et al.*, 2013). Next, the total hysteresis loss of the elements during one revolution is calculated using the maximum principal strain and the loss modulus (G''). The loss modulus was the fraction of energy dissipated as heat.

During the thermal analysis, Cho *et al.* (2013) included convection as well as radiation heat transfer. The convection coefficient in the sidewall region was a function of the radius of the tire, seeing that the relative air flow velocity around the sidewall was assumed to be linear, when the tire is rolling. The dissipation module they developed to compute the hysteresis loss was a function of temperature, thus, the dissipation and thermal calculation was an iterative process, resulting in a convergence criterion that must be satisfied for the temperature.

2.2.2 Effect of Different Operating Parameters

Deformation and heat generation in a tire are influenced by changing the operating parameters to meet the requirements for a specific operation, for example, decreasing the inflation pressure of the tire when driving on sand to enlarge the footprint and increase traction. Changing these parameters

influences the deformation of the tire, which then influence the temperature distribution in the tire. The three main parameters that can be changed during a rolling analysis of a tire are the load, inflation pressure and rolling velocity. The effect of the parameters on the temperature distribution in a rolling tire will be investigated.

First, the effect of the load on the temperature distribution is considered. The research done by Lin and Hwang (2004) and Tang *et al.* (2014) showed that with a heavier load, the average temperature in the tire increases. This is due to the tire deforming more under a heavier load, thus, the strain in the tire will be larger and consequently the heat generation as well. Tang *et al.* (2014) further showed that the load shifts the high temperature region (shown in Figure 2.6). In Figure 2.6a, where the load is 3 kN, the high temperature region is in the centre of the tread. Whereas, in Figure 2.6b, where the load is 6 kN, the high temperature region is on the shoulder of the tire. Figure 2.6 also shows the increase in temperature, due to the increase in load.

Next, looking at the effect of the inflation pressure on the temperature distribution in the tire, decreasing the inflation pressure increases the average temperature in the tire, as determined by Lin and Hwang (2004) and Tang *et al.* (2014). Figure 2.6 shows that as the pressure is decreased, the temperature increased in some locations, while it also decreased in other locations. This was due to the tire deforming different, thus, the strain field in the tire changes. The temperature distribution will thus also change, due to the heat generation being determined from the strain.

Lastly, considering the effect of the rolling velocity on the temperature distribution in the tire, Lin and Hwang (2004) and Cho *et al.* (2013) determined that the temperature will increase with an increase in rolling velocity. This is shown in Figure 2.7, where the tire is rolling at 40 km/h in Figure 2.7a and 140 km/h in Figure 2.7b. The increase in temperature is due to the increase in deformation frequency of the tire, resulting from the higher rolling velocity.

2.2.3 Effect of Different Material Properties and Designs

Strength and flexibility of the tire can be adjusted by using different materials in the tire construction. In addition, the design of the tread can be adapted for different operating conditions. This will influence the ride comfort, load carrying capability of the tire and the temperature distribution in the tire.

Body plies are the main load carrier in the tire, as stated earlier. Therefore, if the stiffness of the body plies is increased, the deformation of the tire would decrease. However, this will also cause the ride to be less comfortable due to the tire losing flexibility, but will increase the load carrying capability. Tang *et al.* (2014) did a study on the effect of the stiffness of the body plies on the temperature in the tire during rolling. They studied four different body

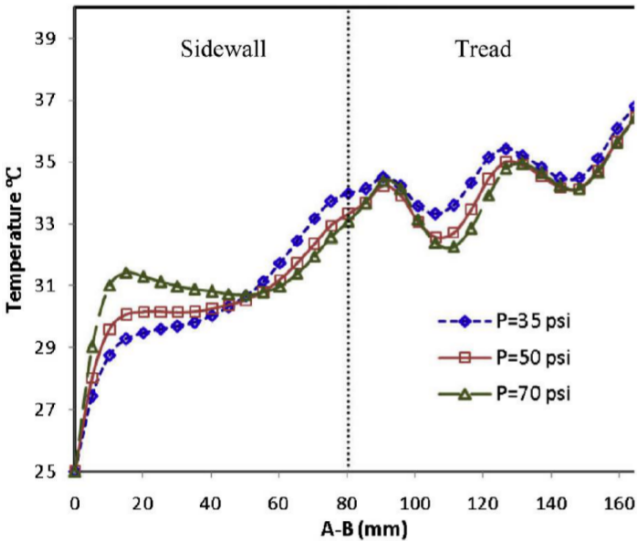

(a) Temperature distribution for a load of 3 kN

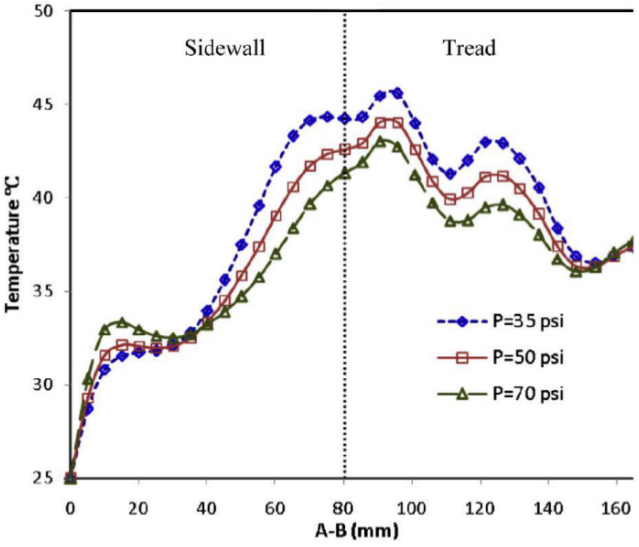

(b) Temperature distribution for a load of 6 kN

Figure 2.6: Temperature distribution for different pressures from the sidewall to the tread (Tang *et al.*, 2014)

plies with a stiffness of 500 MPa, 1 500 MPa, 3 000 MPa and 4 000 MPa. They determined that increasing the body ply stiffness does not only lower the average temperature, it also shifts the high temperature region from the sidewall to the tread, as shown in Figure 2.8. The high temperature in the sidewall is a result of severe deformation that occurs when the stiffness of the body plies are low (Tang *et al.*, 2014). If the body plies are stiffer, the deformation in the sidewall will decrease. The decrease in sidewall deformation leads to a decrease in heat generation and ultimately lower temperatures in the sidewall of the tire (Tang *et al.*, 2014). This shows that a balance between

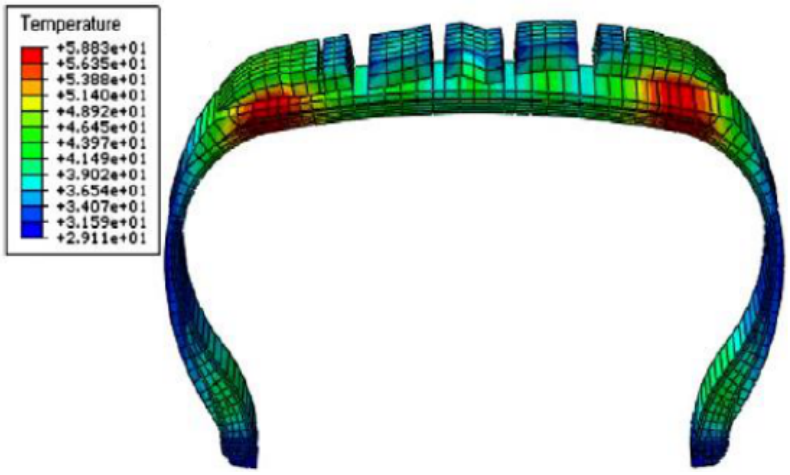

(a) Rolling velocity of 40 km/h

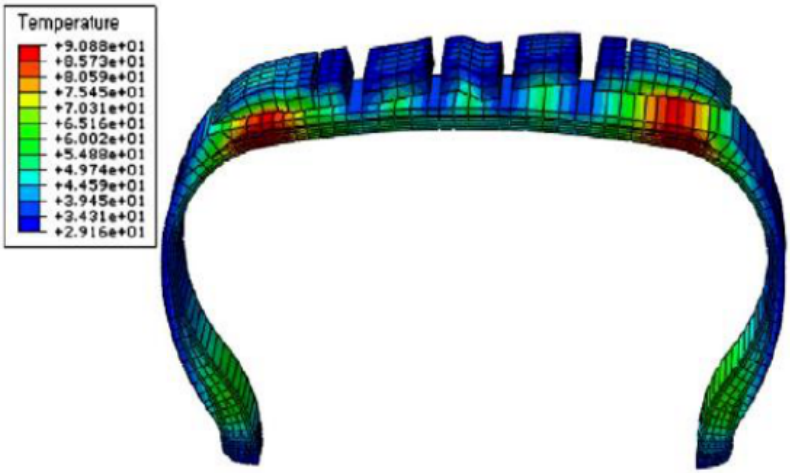

(b) Rolling velocity of 140 km/h

Figure 2.7: Temperature distribution (°C) for different rolling velocities (Cho *et al.*, 2013)

load carrying capacity and ride quality can be achieved by varying the stiffness of the body plies.

Tread designs can also influence the heat generation in the tire, taking into account that more rubber will generate more heat. Cho *et al.* (2013) did a study on two different tread patterns to determine the effect the tread's design has on the heat generation. Figure 2.9 shows the temperature distribution for the two different tread designs. Tread pattern one had a high temperature region at the belt edge, as seen in Figure 2.9a, while tread pattern two distributed the temperature uniformly over the tread region (Cho *et al.*, 2013). There was also a decrease of 26,85 % in the peak temperature in tread pattern two, according to Cho *et al.* (2013). This study showed that the correct tread design is crucial to minimise the average and peak temperatures in the tire,

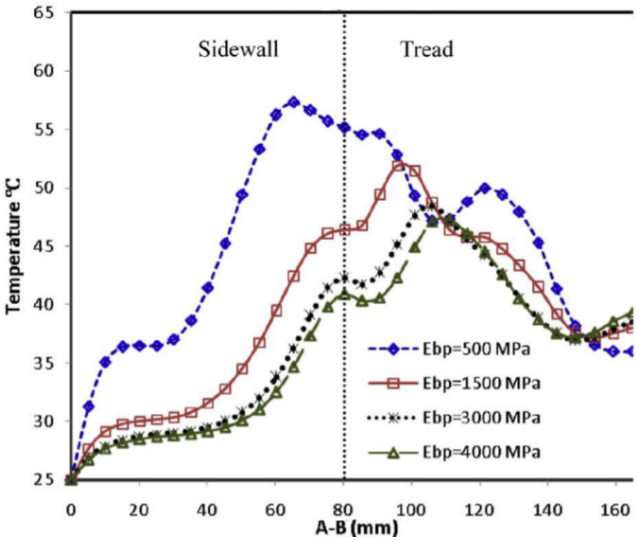

Figure 2.8: Temperature distributions for different body ply stiffness (Tang *et al.*, 2014)

but it is possible that it would increase the pattern noise.

2.3 Conclusion

Research done on the numerical modelling of tires showed that it is possible to determine the temperature distribution through numerical simulations. However, the geometry of the tire is complex to model due to the different materials in the tire and how the materials interact with each other. The material properties of rubber are time consuming to determine through experimental tests, therefore, material properties from literature are used for the initial modelling of tire. The modelling of the rolling tire is divided into three steps, namely: loading, rolling and thermal analysis in most cases. The research done on rolling tires indicated the temperature in the tire is influenced by different parameters, including: the load, rolling velocity, inflation pressure, tread pattern and materials. However, these parameters also influence the ride quality, load rating and pattern noise created by the tire. Therefore, it is a trade-off between these parameters to determine the optimal operating conditions and design for the tire.

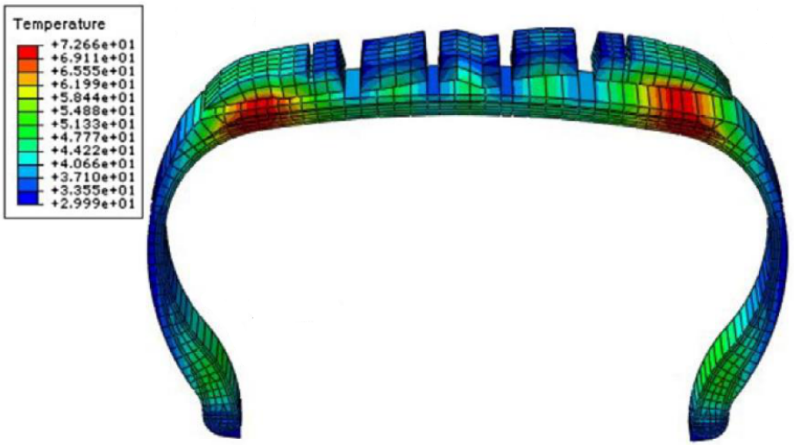

(a) Tread pattern one

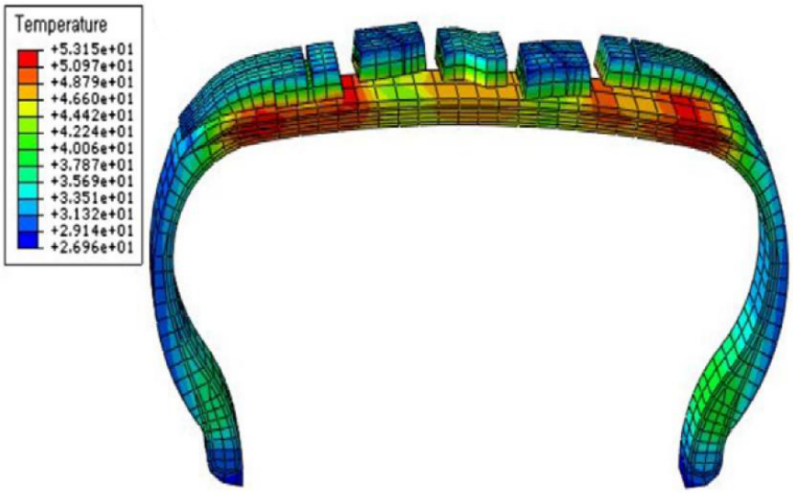

(b) Tread pattern two

Figure 2.9: Temperature distribution (°C) of different tread pattern tire models (Cho *et al.*, 2013)

Chapter 3

Considerations for Numerical Modelling of a Rolling Tire

Certain modelling complications should be considered in preparation for the numerical modelling of a tire. Considerations include the nonlinear materials, nonlinear boundary conditions, as well as the complex construction of the tire geometry. Assumptions and solutions that have been identified when MSC.Marc 2014.0.0 is used as a solver for the nonlinear tire model will also be discussed.

3.1 Nonlinear Analysis

The computational requirements for solving a nonlinear model are significantly higher than that of a linear model. While a linear model only requires one iteration to solve the model, a nonlinear model must be divided into a series of incremental linear models. In a nonlinear model, the first incremental linear model is solved, after which the results of the first increment are used to update the subsequent linear models. This updated incremental linear model is then solved, from where the process continues until convergence is reached. Another difference between a linear and nonlinear model is that the linear model provides one answer, whereas the nonlinear model provides a answer depending on the convergence criteria used.

3.2 Rubber Behaviour

Rubber is an isotropic hyper-viscoelastic material that has a nonlinear stress-strain relationship. Rubber is also incompressible, resulting in the Poisson's ratio (ν) being 0,5. Rubber experiences large strains and deformations under normal loads while hysteresis and softening occur during cyclic loading (Ghoreishy *et al.*, 2014). The nonlinear stress-strain relationship and incompressibility of rubber causes difficulty to model it numerically.

There are different material models that can be used for the analysis of rubber in MSC.Marc. These include the Mooney, Ogden, Arruba Boyce, Gent, Bergstrom Boyce, Marlow and Anisotropic hyperelastic material models (MSC, 2014). These models are used in conjunction with experimental results of rubber to determine the model parameters and eventually determine the best model for the specific application. However, the required experimental data are time consuming and costly to obtain and are thus not always available. Therefore, a material model with available parameters is often used in literature to model the rubber in the tire. The limited availability of these material parameters is also why the tire is modelled by only one type of rubber in most cases. In this project the Mooney-Rivlin material model will be used to model the rubber and only one type of rubber will be used to model the sidewall and tread.

3.3 Reinforcement by Bead Wire and Plies

The reinforcement of the tire is important, as it is the main load carrier and it helps to maintain the shape of the tire, as discussed in Chapter 2. The main reinforcement components of the tire are the bead wire, body and steel belt plies.

In this project the bead wire is modelled as a solid ring with isotropic material properties and not a wound-up wire cable as discussed in Chapter 2. The precise modelling of the bead wire is not essential in the model. However, the strength of the bead wire is fundamental, since, it holds the tire on the rim after inflation, as well as when the tire is rolling.

On the contrary, the modelling of the body and steel belt plies are crucial because they carry the load, inflation pressure and maintain the shape of the tire. Furthermore, the strain rubber experiences under loading and inflation, depends on the flexibility and strength of the plies. Therefore, in order to determine accurate deformations and temperatures, the correct modelling of the plies are important.

For this project the body and steel belt plies will be modelled using `Rebar` elements in MSC.Marc. The rebar material, rebar area, number of rebar layers, number of rebars per length and rebar orientation for the plies needs to be specified for the `Rebar` element. Furthermore, the plies are placed at their precise locations inside the rubber elements by using the `Insert` option in MSC.Marc. This definition ties the degrees of freedom of the nodes in the inserted element list to the degrees of freedom of the nodes in the host body elements, based on the isoparametric location within the host elements (MSC, 2014).

3.4 Inflation Pressure

The mass of the gas inside an inflated tire remains constant; therefore, the pressure will rise when the volume or the temperature of the tire is changed. This is achieved in the numerical model by using the `Cavity` function in MSC.Marc. A cavity is specified with a reference pressure, temperature and density that are used to calculate the specific gas constant (R) and also the mass of the gas inside the tire, using the volume of the cavity (MSC, 2014). During inflation, the mass of the gas in the cavity rises, but after inflation the mass stays constant. The mass of the gas is used to calculate the increase in pressure from the change in volume when the load is applied to the tire. In the case of a tire, the temperature of the gas inside the tire will rise as the temperature of the tire rises. In the numerical model, this pressure increase will be ignored, as it is not possible to model the gas inside the tire, capturing this temperature increase using MSC.Marc.

3.5 Contact between Tire, Rim and Road

The modelling of contact between bodies is complex, seeing, the motion of multiple bodies needs to be tracked, as well as the motion due to the interaction of the bodies after contact occurs and includes the friction between surfaces (MSC, 2014). Friction increases the complexity of modelling contact due to the discontinuity in the friction value, as shown by the Coulomb friction model in Figure 3.1. From Figure 3.1 it is evident that the friction stress or force has a step function behaviour based on the value of the relative sliding velocity (v_r) or the tangential relative incremental displacement (Δu_t) for a given normal stress or force (MSC, 2014). To overcome this discontinuity, different approximations for the step function is implemented in MSC.Marc. Examples include the `Coulomb Arctangent` model, the `Coulomb Stick-Slip` model and the `Coulomb Bilinear` model. The `Coulomb Bilinear` friction model, as shown in Figure 3.1, is the recommended model by MSC.Marc and will be used for the tire modelling in this project.

The contact between the actual tire and rim is a glued type of contact, because the tire does not slip on the rim. Therefore, the friction between the tire and the rim in the numerical model, will be modelled by a touching contact with a high friction coefficient. This assumption is made due to the tire not being in contact with the rim at the start of the simulation, thus, glued contact can not be used. The contact between the actual tire and the road is a touching contact with a high friction coefficient. The same conditions will be applied in the numerical model between the tire and the drum.

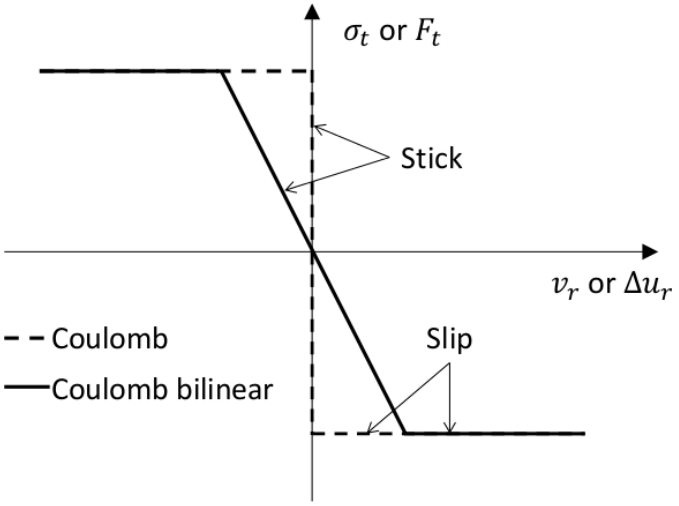

Figure 3.1: Coulomb and Coulomb bilinear friction model

3.6 Heat Generation

The heat generated by the hysteresis effect in the rubber can be calculated using two methods, namely: a coupled structural and thermal analysis or an uncoupled analysis. In the coupled analysis, a structural and thermal analysis is done for each increment, whereas for an uncoupled analysis, separate structural and thermal models are solved.

When a coupled structural and thermal analysis are done, the heat generated within an element is calculated by the viscoelastic material properties of the rubber. However, this analysis is computationally expensive seeing that the tire must be rolled for many revolutions until the temperatures stabilise. Therefore, this method is not suitable for the type of numerical procedure considered here.

The uncoupled analysis requires more steps to solve the model, but it is not as computationally expensive as the coupled analysis. In the uncoupled analysis a structural model is solved first. After that, the results of the structural model are used to calculate the heat generated from the rolling. Then, a thermal analysis is done to determine the temperature distribution in the tire. This analysis saves on computational time, as the tire is only rolled for a few revolutions. The uncoupled analysis will be used in this project, dividing the model into a rolling and thermal analysis.

The heat generated from the friction between the tire and the road are difficult to obtain and is a function of the operating conditions. Therefore, the heat generated from friction will be ignored in this project.

3.7 Heat Transfer

Heat transfer between the tire and the surrounding air, as well as between the tire and inflation air, are through convection and radiation. Radiation will not have a notable effect on the heat transfer due to the temperature difference between the tire surface and the surrounding surfaces being small. Thus, radiation heat transfer will be ignored in this project. However, convection heat transfer will be notable because of the potentially high rolling velocity of the tire.

The forced convection coefficient is a function of the rolling velocity of the tire, as well as the temperature. Furthermore, the convection coefficient on the outside of the tire will be higher at the shoulder, compared to the convection coefficient at the bead, due to the larger velocity at the shoulder. This will, however, be ignored because it makes the generation of the thermal model difficult, while not adding to the model. It will also be assumed the temperature does not have an effect on the convection coefficient on the outside of the tire due to the small temperature changes on the outside surface of the tire. On the inside of the tire, a natural convection coefficient is assumed, with an internal temperature determined from the experimental tests.

3.8 Conclusion

Complications in the modelling of a rolling tire were discussed in this chapter and the assumptions that will be used to simplify these complications were considered. The modelling of rubber is difficult due to the nonlinear stress-strain relationship and incompressible behaviour. Based on data reported in literature the rubber will be modelled using the Mooney-Rivlin material model and only one type of rubber is used in this project. The bead wire will be modelled as an isotropic material, while the body and steel belt plies are modelled using `Rebar` elements and placed in position using the `Insert` option. Furthermore, a `Cavity` function is used to model the inflation of the tire and the model is solved as an uncoupled structural/thermal analysis and only the convection heat transfer is modelled.

Chapter 4

Theoretical Models for the Modelling of Hyperelastic Materials

Hyperelastic materials like rubber have a nonlinear stress-strain relationship and are also incompressible, as discussed in Chapter 3. These properties have an influence on the modelling of hyperelastic materials, causing it to become computationally expensive, since nonlinear models must be used. The aim of this chapter is to discuss the material model used to model the rubber and how the hysteresis coefficient is calculated. In addition, the calculation of the total strain energy density and the lost strain energy density from the material model will be discussed, as well as how the heat generation rate ($\dot{q}_g$) in each element is calculated.

4.1 Material Model

The Mooney-Rivlin material model was used to model the rubber in the tire. It is important to know the Mooney-Rivlin model is not based on any physical understanding of the material behaviour; it is only a curve fit of various polynomials to test data. The Mooney-Rivlin strain energy density function is described

$$U = C_{10}(I_1 - 3) + C_{01}(I_2 - 3) \tag{4.1}$$

where U is the strain energy density ($\mathrm{J/m^3}$), C_{10} and C_{01} are the Mooney-Rivlin material constants, determined by curve fitting to test data and I_1 and I_2 are the first and second deviatoric strain invariants. The strain invariants are defined as

$$I_1 = \lambda_1^2 + \lambda_2^2 + \lambda_3^2 \quad \text{and} \quad I_2 = \lambda_1^2\lambda_2^2 + \lambda_2^2\lambda_3^2 + \lambda_3^2\lambda_1^2 \tag{4.2}$$

where λ_i are the principal stretch ratios. The stretch ratio is defined as the ratio between the deformed length (l) and the undeformed length (L) (Kelly, 2012)

$$\lambda = \frac{l}{L}. \tag{4.3}$$

The principal stretch ratios are in the principal directions of the model. Since rubber is incompressible, the constraint equation $\lambda_1\lambda_2\lambda_3 = 1$, must also be satisfied.

4.2 Hysteresis

The heat generated during the deformation of an elastic material, like rubber, is due to the hysteresis loss of the material. Hysteresis is present in a material when the amount of energy recovered from deformation is less than the amount of energy put into deforming the material. The energy that is not recovered from the deformation is stored in the object as heat.

The hysteresis coefficient (H) of a material is determined through a dynamic material analysis (DMA) test. The DMA test measures the storage modulus ($E^{'}$) and the loss modulus ($E^{''}$) of the material by applying a cyclic deformation (PerkinElmer, 2013). The hysteresis coefficient is then calculated by dividing the lost energy by the total energy (Lin and Hwang, 2004) i.e.

$$H = \frac{\text{Energy lost}}{\text{Total energy}} = \frac{E^{''}}{E^{*}} \tag{4.4}$$

where E^* is the total energy input described by

$$E^{*} = \sqrt{(E^{'})^2 + (E^{''})^2}. \tag{4.5}$$

4.3 Total Strain Energy

Total strain energy is the amount of energy stored in an element due to the deformation of the element when external forces act on it. In the numerical simulation of rubber, the Mooney-Rivlin strain energy density, also known as the elastic strain energy density, is the strain energy per unit volume ($\frac{dU}{dV}$) in the rubber.

The elastic strain energy density is calculated for each increment using equation 4.1 and is shown for one revolution of the tire in Figure 4.1. The elastic strain energy density is then used to calculate the total strain energy density for a node by taking the sum of the difference between the increments where the elastic strain energy density is increasing, i.e.

$$U_{tsed} = \sum_{i=1}^{n} \Delta U_i \tag{4.6}$$

where U_{tsed} is the total strain energy density ($\mathrm{J/m^3}$) of a node, n is the number of times the elastic strain energy increases from increment to increment and ΔU_i is the increase in elastic strain energy density ($\mathrm{J/m^3}$) from increment to increment, this is demonstrated in Figure 4.1. The total strain energy density of an element is calculated by averaging the nodal values over the element. For example, if it is a quad four element, the sum of the nodal values is divided by four.

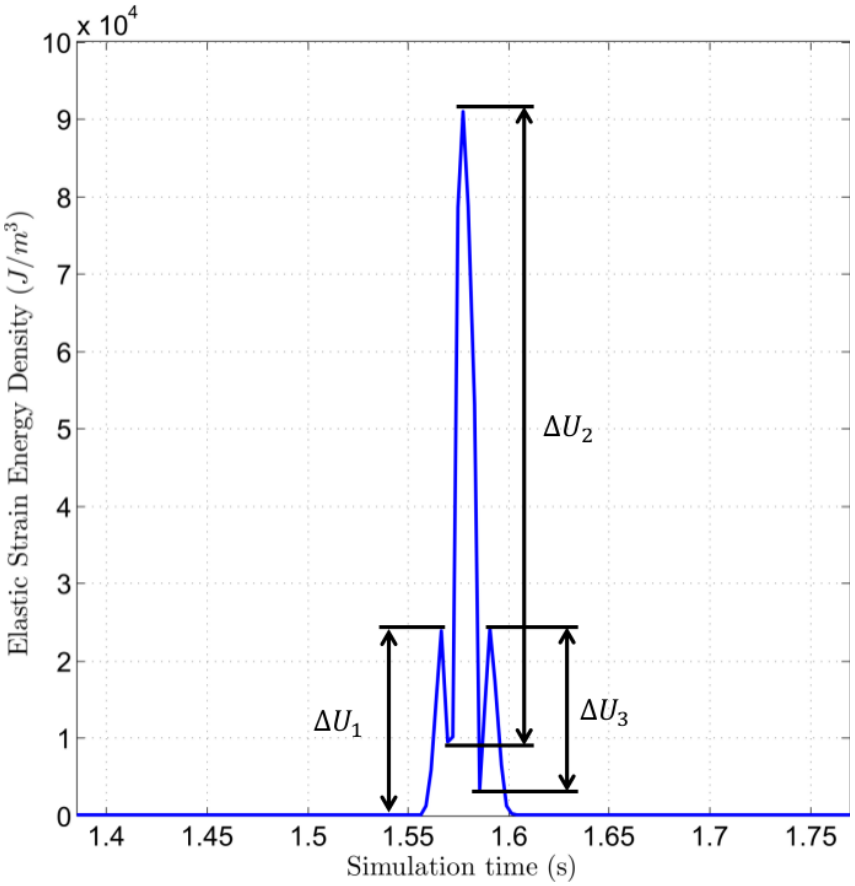

Figure 4.1: Elastic strain energy density at a node for one revolution

The total energy referred to in equation 4.4 is replaced by the total strain energy density in order to calculate the lost strain energy density for the element. The lost strain energy density can this be calculated by

$$U_{LSED} = HU_{TSED} \tag{4.7}$$

where U_{LSED} is the lost strain energy density (J/m^3), H is the hysteresis coefficient and U_{TSED} is the total strain energy density (J/m^3) for an element.

4.4 Heat Generation Rate

The heat generated or the energy lost during the deformation of the rubber in the tire is used to determine the temperature distribution in the tire. The lost strain energy density calculated from equation 4.7 and the frequency at which the tire is rolling will be used to calculate the heat generation rate in the elements. The frequency is calculated by dividing the rolling velocity of the tire by the circumferential length of the tire (Lin and Hwang, 2004),

$$f = \frac{v}{L_r} \tag{4.8}$$

$$L_r = 2\pi R_r \tag{4.9}$$

where f is the rolling frequency (Hz), v is the rolling velocity (m/s), L_r is the circumferential length (m) of the tire and R_r is the radius (m) of the rolling tire. The heat generated in each element is calculated by multiplying the lost strain energy density with the frequency the tire is rolling at,

$$\dot{q}_g = U_{LSED} f \tag{4.10}$$

where $\dot{q}_g$ is the heat generation rate (W/m^3) in the element, U_{LSED} is the lost strain energy density (J/m^3) and f is the rolling frequency (Hz). The frequency is proportional to the rolling velocity of the tire, thus the heat generated will also be proportional to the rolling velocity. The heat generation rate will be used as the heat source in the thermal analysis of the tire.

4.5 Conclusion

This chapter focused on the Mooney-Rivlin strain energy density function (eq. 4.1), which is used to calculate the total strain energy density at each node. The nodal total strain energy density is then averaged over the element to get the total strain energy density for the element. How the hysteresis coefficient can be calculated (eq. 4.4) were also discussed. The hysteresis coefficient and the total strain energy are then used to calculate the lost strain energy density. Lastly, the calculation of the heat generation rate from the lost strain energy density and the frequency were investigated.

Chapter 5

Numerical Analysis

The numerical modelling of a rolling tire was divided into two major steps, the dynamic rolling analysis and the steady-state thermal analysis. The rolling analysis was done in three steps: inflation of the tire using a cavity pressure load; loading of the tire using load control; as well as loading and rolling of the tire using velocity control. The modelling procedures and parameters used to model each of these steps in MSC.Marc 2014.0.0, as well as the material properties for the model, will be discussed in this chapter.

5.1 Tire Geometry

The tire used for the numerical modelling was a 215/70R15 Maxtrek SU-830 passenger vehicle tire. The geometry of the rim and a slice of the tire were measured using a touch probe CNC digitizing machine. The tread pattern of the tire was not measured and was also not modelled, seeing that it only had small grooves and therefore would not have a significant effect on the deformation and heat generation of the tire. The measured geometries were refined and meshed using SimXpert 2012. The meshed models were used for the numerical modelling of the tire and rim.

5.2 Dynamic Rolling Analysis

The rolling of the tire was modelled as an implicit nonlinear structural finite element model. Thermal effects of the materials were ignored in the rolling analysis due to a coupled structural-thermal analysis being too computationally expensive, as discussed in Chapter 3. The three steps in the modelling of the rolling tire, as well as the settings and parameters used will be discussed in this section.

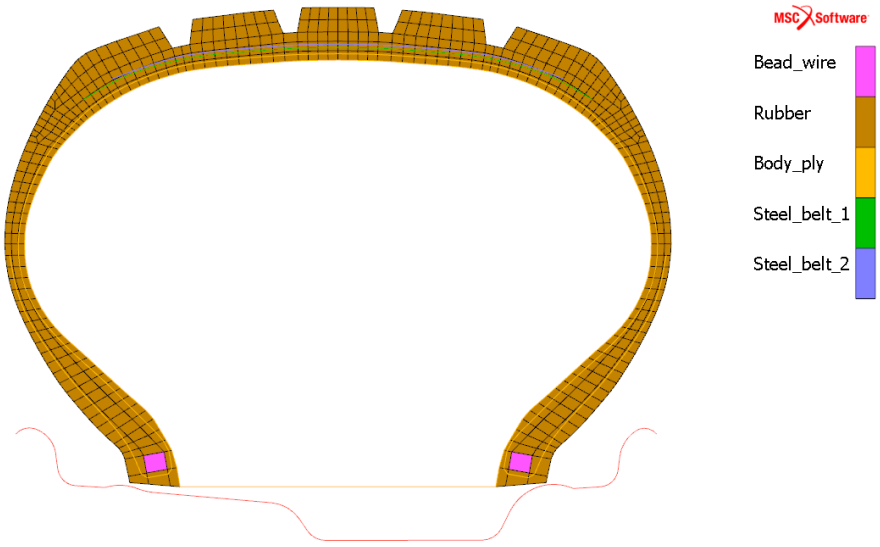

Figure 5.1: Meshed 2-D axisymmetric model before inflation

5.2.1 Inflation Analysis

Inflation of the tire was the first step in the modelling process. The inflation was done on a 2-D axisymmetric model, as shown in Figure 5.1. Figure 5.1 also shows the different materials used in the modelling of the tire, as well as the location of the materials inside the tire.

The bead wire was modelled as an isotropic linear elastic material in the numerical model, while the rubber was modelled using the Mooney-Rivlin material model as discussed in Chapter 4. Furthermore, the body and steel belt plies were modelled as linear elastic materials using the `Rebar` element option in MSC.Marc and placed inside the rubber elements using the `Insert` option, as discussed in Chapter 3. The bead wire and rubber was meshed using `Full & Herrmann Formulation` linear quad elements, while the body ply and steel belts were meshed by two node `Membrane Rebar` elements. The 2-D axisymmetric model consisted of 801 elements and 953 nodes. The material properties used are shown in Table 5.1 and the parameters used to model the `Rebar` elements are shown in Table 5.2. Material properties from literature were used for this study (Tang *et al.*, 2014; Lin and Hwang, 2004). The parameters in Tabel 5.2 for the modelling of the body plies and the steel belt plies, were obtained from the geometry of the tire.

The inflation of the tire was modelled by a `Cavity Pressure Load`, with a reference pressure, temperature and density, as referred to in Chapter 3. To ensure that the model inflates when the pressure was applied, the cavity was closed by placing a `Cavity Surface Element` between the beads of the tire. This element does not add any stiffness to the model, although it closes the cavity, therefore, the volume of the cavity can be calculated. The `Cavity Surface Element`, as well as the pressure applied by the cavity is shown in

Table 5.1: Material properties for tire model

Material	Bead wire	Rubber	Body ply	Steel belt
Young's modulus (MPa)	207 000	-	500	207 000
Poison's ratio	0,3	-	0,3	0,3
Mooney-Rivlin constants	-	C_{10}=8,061	-	-
(MPa)	-	C_{01}=1,805	-	-
Thermal conductivity (W/m°C)	60,5	0,293	0,293	60,5

Table 5.2: Modelling parameters for the `Rebar` elements

Material	Body ply	Steel belt 1	Steel belt 2
Number of layers	2	1	1
Rebar area (10^{-6} m^2)	3,14159	250	250
Number of rebars per length (#/m)	667	714	714
Rebar Angle (°)	0	60	-60

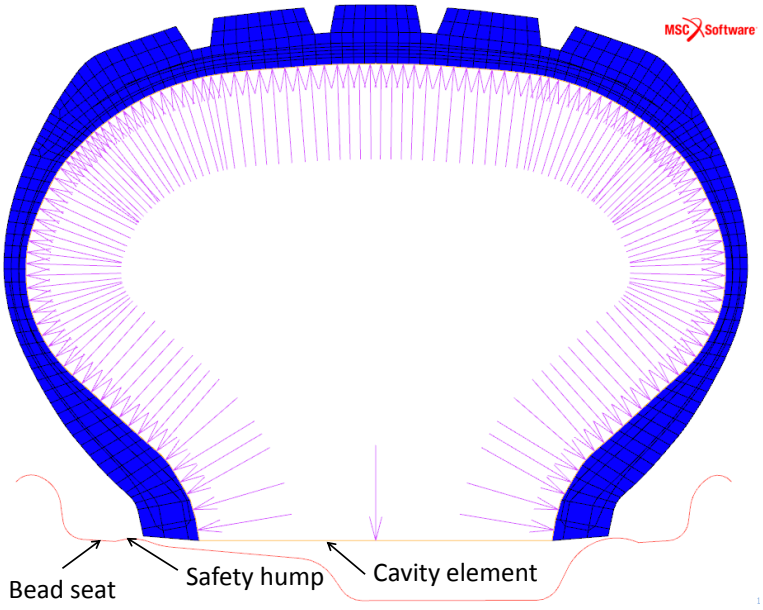

Figure 5.2: Boundary conditions for the inflation analysis

Figure 5.2. Table 5.3 summarises the parameters used for the modelling of the cavity. Air was used as the inflation gas for the model, with the reference properties for the three modelling pressures shown in Table 5.4.

In order to inflate the tire, the pressure was increased as a linear function of time. As the pressure increased, the volume of the cavity increase with it. This volume increase allowed the bead and side wall of the tire to expand

Table 5.3: Modelling parameters for the `Cavity`

Solution procedure	Iterative
Polytropic process exponent	1
Ambient pressure (kPa)	101,325

Table 5.4: Reference properties for the air inflated cavity

Pressure (kPa)	100	300	450
Reference pressure (kPa)	100	300	450
Reference temperature (K)	298,15	298,15	298,15
Reference density (kg/m^3)	1,13865	3,50594	5,25891

sideways and forced the bead over the safety hump on the rim, onto the bead seat. The bead seat ensures an airtight seal between the tire and the rim. The safety hump and bead seat on the rim are shown in Figure 5.2. The tire was modelled as a deformable contact body, while the rim was modelled as a rigid contact body. The outside edges of the tire and the curves of the rim were described by an `Analytical Boundary` description. The analytical boundary description made the edges and curves smooth and saved on computational time due to fewer curves being modelled. In the inflation analysis there was only one contact interaction between the tire and the rim. There was also no friction between the tire and the rim. Therefore, the tire can move freely when in contact with the rim. However, this is a simplification, seeing that the focus is not on how the tire is inflated, but rather the deformation after inflation.

The inflation model was solved using an `Adaptive Multi-Criteria` stepping procedure. The loadcase parameters used for the stepping procedure are summarised in Table 5.5. The convergence of the model was determined using relative residual force convergence criterion, with a convergence ratio of 10^{-3}. The contact between the tire and the rim was modelled using the `Node To Segment` method. Furthermore, the strain, displacement and rotation of the elements in the model were large due to the rubber in the model, therefore, the `Large Strain` structural analysis formulation was used. In this formulation the updated Lagrange framework was used to formulate the governing equations (MSC, 2014).

The results extracted from the inflation analysis were used as the initial condition in the loading and rolling analysis. These results were the deformation gradient, determinant of the deformation gradient and the elastic left Cauchy-Green deformation. The equivalent Cauchy stress and total strain results were also obtained.

Table 5.5: Loadcase stepping parameters for the inflation analysis

Loadcase time (s)	1
Initial fraction of loadcase time	0,01
Minimum fraction of loadcase time	10^{-5}
Maximum fraction of loadcase time	0,5
Desired number of recycles/increment	5
Time step increase factor	1,2
Max number of recycles	10
Iterative procedure	Full Newton-Raphson

5.2.2 Loading Analysis

The second step in the modelling process was the loading analysis of the tire. In this step a load was applied to a 3-D expanded tire model, as shown in Figure 5.3.

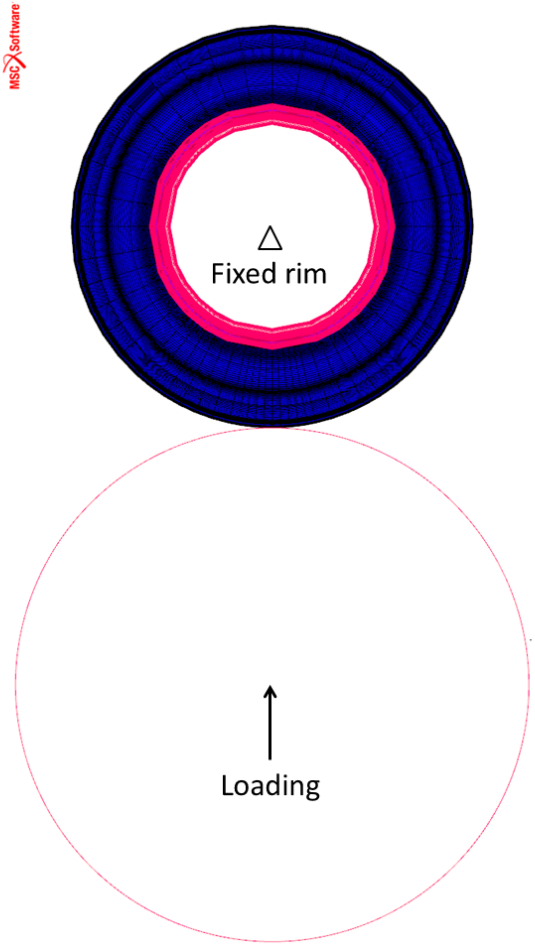

Figure 5.3: Boundary conditions for the loading analysis

The 3-D model was created by expanding the 2-D axisymmetric model used in the inflation analysis. In order to decrease the number of elements in the model, the model was expanded into different repetition angles, as seen in Figure 5.3. The repetition angles and number of repetitions for each angle are shown in Table 5.6. The bead wire and rubber were meshed in the 3-D model using `Full & Herrmann Formulation` linear hexagon elements, while the body ply and steel belts were meshed by quad `Membrane Rebar` elements. The 3-D model consisted of 41 652 elements and 30 212 nodes.

Table 5.6: Repetition angle and number of repetitions for the 3-D model

Repetition angle	Number of repetitions
$2,5°$	5
$5°$	6
$7,5°$	5
$10°$	20
$7,5°$	5
$5°$	6
$2,5°$	5

The road surface was modelled as a cylinder with a radius of 0,87 m and not as a flat surface for the experimental setup and numerical model to be executed under the same conditions. The cylinder is a rigid contact body and the surface of the cylinder is modelled by an `Analytical Boundary` description. The cylinder was located below the tire where the expanded repetitions of the tire model are small, in order to get accurate displacement results, as shown in Figure 5.3. The `3-D C0-Continuity` option was used as the `Analytical Boundary` description of the deformable tire contact body in the loading analysis. This option modified the in-plane description of the segments, where the boundary normals were discontinuous by taking the curved shape of the edge into account (MSC, 2014). In the loading analysis there were two contact interactions, one between the tire and the rim and the other between the tire and the cylinder. The friction coefficient between the tire and the rim was 0,9 and between the tire and the road 0,7 (Nave, 2014).

The results from the 2-D axisymmetric inflation analysis were used as an initial condition for the loading analysis; therefore, the tire was already inflated before the start of the loading. However, to ensure that the inflation pressure was correct after the expansion, a `Cavity Pressure Load` was applied to the cavity first. The pressure was held constant for a short time period, enabling any pressure change that could have resulted to be corrected. Thereafter, the `Cavity Pressure Load` was changed to a `Cavity Mass Load`. The `Cavity Mass Load` closed the cavity and held the mass of air inside the tire constant. Therefore, if the volume of the tire changed, the pressure in the tire changed

as well. After the tire was inflated to the correct pressure, the tire could be loaded.

The load was applied using the `Load Control Rigid Body` option. This option allowed a point load to be applied to a control node that transferred the load to the rigid cylinder body (shown in Figure 5.3). The cylinder came in contact with the tire and deformed it. The load was increased linearly as a function of time. The tire was loaded with three loads: 300 kg, 500 kg and 700 kg.

The loading analysis was divided into two loadcases, namely: the inflation loadcase and the loading loadcase. The same stepping procedure and convergence criterion used for the inflation analysis was used for the loading analysis. The parameters used for the inflation loadcase are summarised in Table 5.7 and for the loading loadcase in Table 5.8.

Table 5.7: Stepping parameters for the inflation loadcase

Loadcase time (s)	0,5
Initial fraction of loadcase time	0,5
Minimum fraction of loadcase time	10^{-5}
Maximum fraction of loadcase time	0,75
Desired number of recycles/increment	5
Time step increase factor	1,2
Max number of recycles	10
Iterative procedure	Full Newton-Raphson

Table 5.8: Stepping parameters for the loading loadcase

Loadcase time (s)	1,5
Initial fraction of loadcase time	0,1
Minimum fraction of loadcase time	10^{-5}
Maximum fraction of loadcase time	0,5
Desired number of recycles/increment	10
Time step increase factor	1,2
Max number of recycles	20
Iterative procedure	Full Newton-Raphson

The contact between the tire and the rim and between the tire and the cylinder were modelled using the `Node To Segment` method, with the `Coulomb Bilinear (Displacement)` friction model (as discussed in Chapter 3). The parameters for the friction model is summarised in Table 5.9. The `Large Strain` structural analysis formulation was also used for the loading analysis.

Table 5.9: Parameters for the `Coulomb Bilinear (Displacement)` friction model

Friction force tolerance	0,05
Slip threshold	Automatic

The displacement results of the cylinder during the loading analysis was needed, as the load was applied using displacement control during the rolling analysis. This was done due to the load control being more computationally expensive. The deformation, total strain and contact normal stress results were also obtained.

5.2.3 Rolling Analysis

The last step in the dynamic rolling analysis was the actual rolling of the tire. The same 3-D tire model was used for the rolling analysis, as used in the loading analysis. However, the tire was rotated by 180° around the axial axis, so the nodes where the results were extracted start rolling from the top (as shown in Figure 5.4).

The following parameters of the rolling analysis were the same as for the loading analysis:

- Contact model
- Contact body definitions
- Contact body boundary descriptions
- Contact interactions
- Friction model
- Friction coefficients
- Initial condition
- Initial `Cavity Pressure Load`
- Switch to a `Cavity Mass Load`
- `Large Strain` formulation
- `Adaptive Multi-Criteria` stepping procedure
- Convergence criteria for the loadcases
- Parameters for the inflation loadcase

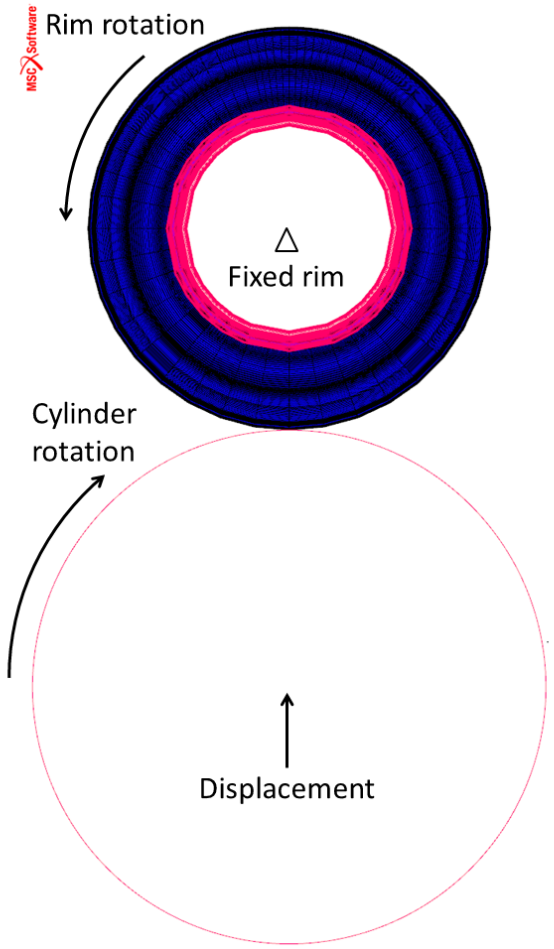

Figure 5.4: Boundary conditions for the rolling analysis

The load in the rolling analysis was applied as a displacement of the cylinder and not a force. The rotation of the rim and cylinder, as well as the displacement of the cylinder, was applied using the `Velocity Control Rigid Body` option. In this option, a velocity or a rotational velocity were applied to the rigid body in the direction specified. The velocities were held constant for a specified duration during the displacement and rolling steps. The velocity of the tire was 20 km/h in the rolling analysis. Therefore, the rotational velocity of the rim and the cylinder was 16,307 rad/s and 12,771 rad/s in different directions respectively. The tire was rolled for approximately two revolutions, so the results can settle before it was extracted. The boundary conditions for the rolling analysis are shown in Figure 5.4.

The rolling analysis was divided into three loadcases, namely: the inflation loadcase, the displacement loadcase and the rolling loadcase. The parameters used for the displacement loadcase was the same as in Table 5.8, with only the loadcase time that changed from 1,5 s to 0,5 s. The parameters for the rolling loadcase are summarised in Table 5.10.

Table 5.10: Stepping parameters for the rolling loadcase

Loadcase time (s)	0,85
Initial fraction of loadcase time	0,001
Minimum fraction of loadcase time	10^{-6}
Maximum fraction of loadcase time	0,05
Desired number of recycles/increment	15
Time step increase factor	1,2
Max number of recycles	30
Iterative procedure	Full Newton-Raphson

The elastic strain energy density in the elements was the main result obtained from the rolling analysis. The tire was rolled for one revolution before the results extraction commenced at the start of the next revolution. The deformation, equivalent Cauchy stress, total strain and contact normal stress results were also obtained during the rolling analysis.

5.3 Steady-State Thermal Analysis

The steady-state thermal analysis was modelled as an implicit, nonlinear, thermal/structural, 2-D axisymmetric model of the tire. A 2-D axisymmetric model was used due to the temperature distribution in the circumferential direction being the same. The settings and parameters used for the thermal analysis are discussed in this section.

The 2-D axisymmetric model used in the thermal analysis was adapted from the inflation model in the dynamic rolling analysis. The thermal conductivities of the materials were added to the thermal material properties of the model, as shown in Table 5.1 and a uniform initial temperature distribution of 20 °C was applied to all the nodes. Furthermore, a `Volume Flux`, calculated by the steps discussed in Chapter 4, was added to each of the rubber elements in the model. The rolling speed of the tire used to calculate the heat flux and the ambient temperature on the outside of the tire, was varied to determine the effect it has on the maximum temperature. Convection heat transfer was added to the inside and outside of the tire as an `Edge Film`, with the parameters shown in Table 5.11 and Table 5.12 respectively. The forced convective heat transfer coefficient on the outside of the tire was calculated using equation 5.1 obtained from Lin and Hwang (2004).

$$h_o = 5,9 + 3,7v \tag{5.1}$$

where h_o is the convection coefficient (W/m^2 °C) on the outside of the tire and v is the rolling velocity (m/s). The film coefficient in Table 5.12 was calculated for a rolling velocity of 60 km/h. A natural convection coefficient was used

for the convection on the inside of the tire. The ambient temperature (in Table 5.11) was determined from the experimental tests done on the tire. The boundary conditions for the thermal analysis are shown in Figure 5.5.

Table 5.11: Inside `Edge Film` parameters

Ambient temperature settings method	Single sink point
Ambient temperature (°C)	35
Evaluation temperature	Ambient
Film coefficient (W/m^2 °C)	5,9

Table 5.12: Outside `Edge Film` parameters

Ambient temperature settings method	Single sink point
Ambient temperature (°C)	20
Evaluation temperature	Ambient
Film coefficient (W/m^2 °C)	67,778

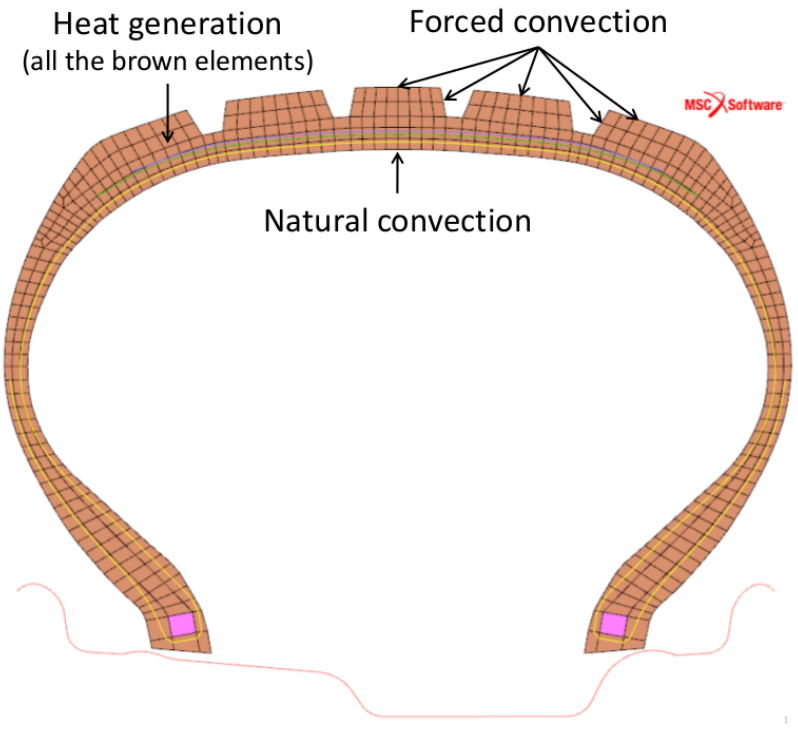

Figure 5.5: Boundary conditions for the thermal analysis

The thermal analysis was divided into two loadcases, namely: the inflation loadcase and the heating loadcase. Both loadcases used the `Adaptive Multi-Criteria` stepping procedure to solve the model. The structural convergence of both loadcases was determined using a relative residual force convergence criteria, with a convergence ratio of 10^{-3}. Thermal convergence was achieved using a `max error` in the temperature estimate of `zero`. The parameters used for the inflation loadcase are summarised in Table 5.5 and for the heating loadcase in Table 5.13.

Table 5.13: Stepping parameters for the heating loadcase

Loadcase time (s)	10 000
Initial fraction of loadcase time	0,01
Minimum fraction of loadcase time	10^{-5}
Maximum fraction of loadcase time	0,1
Desired number of recycles/increment	5
Time step increase factor	1,2
Max number of recycles	10
Iterative procedure	Full Newton-Raphson

The results obtained from this analysis included the temperature distribution and the heat source distribution inside the tire for the operating conditions used in the rolling analysis. These conditions were varied to determine the effect on the temperature distribution inside the tire.

5.4 Conclusion

The steps used to do the numerical modelling of the tire were discussed in detail in this chapter. These steps are the inflation, loading, rolling and thermal analyses. The meshed model with the location of the different materials and material parameters was shown. The elements used for the 2-D axisymmetric and 3-D model were also discussed. In addition, the parameters of the `Cavity`, friction model, contact model, contact conditions, `Edge Film` and loadcases for each of the steps, were provided.

Chapter 6

Numerical Results

The temperature distribution in the rolling tire was the primary result determined through the numerical modelling. The deformation of the tire, as well as the tire footprint or the contact stress distribution between the tire and road surface, are the secondary results obtained from the numerical model, used for comparison the results. The deformation and contact stress distribution were validated using experimental results. The results were evaluated under different operating conditions, including inflation pressure, loading force and rolling velocity. The results from the numerical modelling of the tire, as discussed in Chapter 5, will be addressed in this chapter.

6.1 Dynamic Rolling Results

The inflation, loading and rolling of the numerical tire model was executed in the dynamic rolling analysis. The deformation of the 2D-axisymmetric tire model, before and after inflation to a pressure of 300 kPa, are shown in Figure 6.1. After inflation, the bead of the tire moved over the safety hump and onto the bead seat. The deformation result of the 2D-axisymmetric model was used as an initial condition for the loading and rolling analysis, as referred to in Chapter 5. In this section the deformation of the tire, contact stress distribution and elastic strain energy density results are discussed.

6.1.1 Loading Analysis Results

In the loading analysis, the load was applied to the inflated tire model. The inflated tire deformed under the load, creating a contact stress distribution on the road surface, in this model the rigid cylinder. Deformation of the tire and the contact stress distribution varied in relation to the inflation pressure and the load applied to the tire, as discussed in this section.

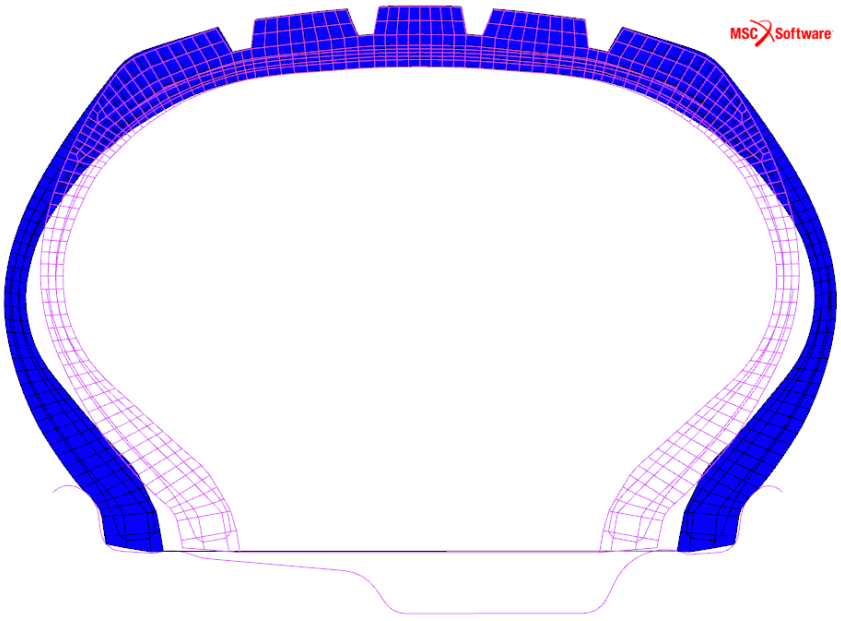

Figure 6.1: 2D-axisymmetric tire model before and after inflated to 300 kPa

6.1.1.1 Deformation of Tire

The principal stretch ratios used to calculate the elastic strain energy density in the tire, were determined from the deformation of the tire. Therefore, the correct deformation of the numerical model was essential in the calculation of the elastic strain energy density, which was used to determine the heat generated during the rolling of the tire.

The deformation and nodal displacement of the tire, with a load of 500 kg and inflated to a pressure of 300 kPa, is shown in Figure 6.2. All the displacements were measured from after inflation to the end of loading. Figure 6.2 shows the displacement of the tire was symmetric around the middle of the tire. However, the symmetry was expected, seeing that the numerical model of the tire was symmetric around the middle of the tire.

When the inflation pressure was decreased to 100 kPa and the load stayed at 500 kg, the tire deformed more and the displacement of the tire was larger, as shown in Figure 6.3. In contrast, when the inflation pressure was increased to 450 kPa, the displacement and deformation of the tire were less, as seen in Figure 6.4. The decrease in deformation due to the increase in inflation pressure was expected since the density of the air inside the tire increased, therefore, restricting the deformation. The increased inflation pressure resulted in a better load carrying capability of the tire, although it will reduce the ride quality of the tire.

The volume of the tire changed when the tire was loaded with different loads; therefore, the inflation pressure in the cavity also changed. However, the pressure change was not significant in these simulations, although it could make

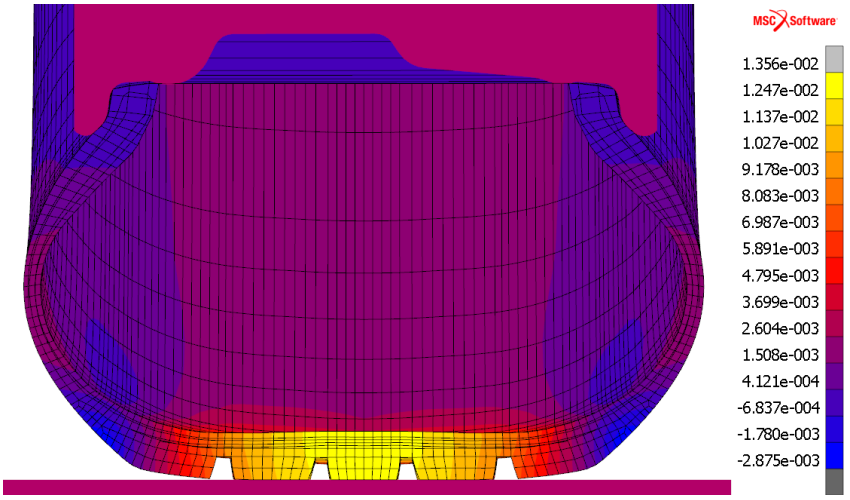

Figure 6.2: Nodal displacement (m) of the tire under a load of 500 kg and a pressure of 300 kPa

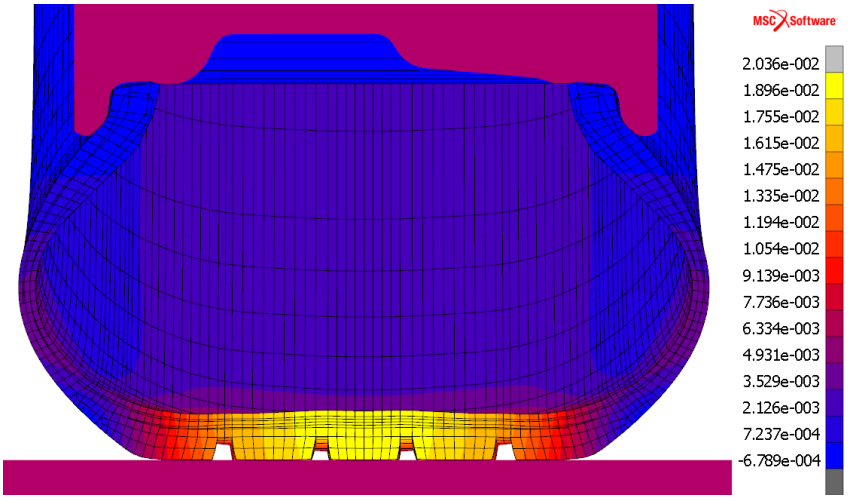

Figure 6.3: Nodal displacement (m) of the tire under a load of 500 kg and a pressure of 100 kPa

a difference if the deformation of the tire becomes large. The inflation pressure after loading, maximum nodal displacement of the tire and displacement of the rigid cylinder after the loading analysis for the different operating conditions are shown in Table 6.1. In Table 6.1 it is evident that the pressure inside the tire did not change significantly during the loading, due to the deformation of the tire being small. The displacement of the cylinder was used to apply the force to the tire in the rolling analysis, as discussed in Chapter 5.

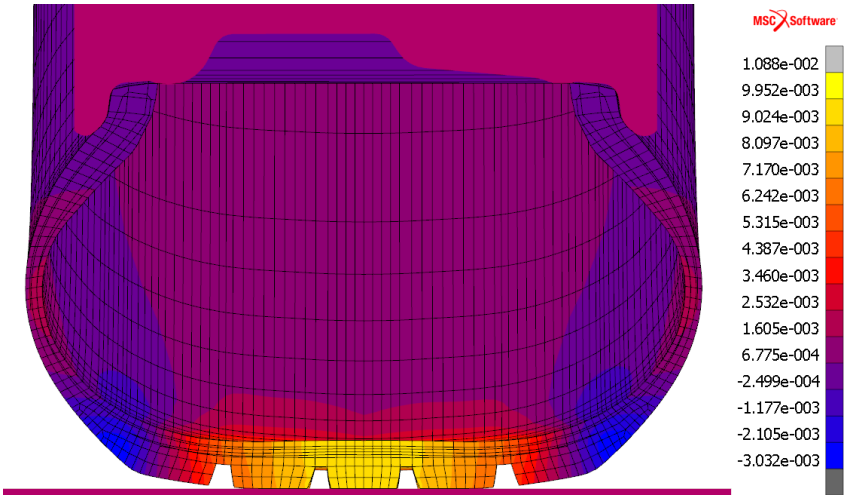

Figure 6.4: Nodal displacement (m) of the tire under a load of 500 kg and a pressure of 450 kPa

Table 6.1: Loading results for the different operating conditions

Load (kg)	Inflation pressure (kPa)	Pressure after loading (kPa)	Max nodal displacement of tire (mm)	Displacement of cylinder (mm)
300	100	100,2	11,5	11,2
	300	300,2	7,8	7,8
	450	450,2	6,6	6,6
500	100	100,5	20,4	19,4
	300	300,5	13,6	13,6
	450	450,4	10,9	10,9
700	100	101,0	26,8	26,1
	300	301,0	19,2	19,2
	450	451,0	16,7	15,7

6.1.1.2 Contact Stress

The contact stress distribution between the tire and the rigid cylinder, gives an indication of how well the tire distributes the load applied to it on the road surface. The distribution of the load is optimal when the whole tread is in contact with the road surface and the stress is evenly distributed over the contact area. For example, if the inflation pressure of the tire is too high, the tire will not be able to flex enough to make good contact with the road and distribute the load evenly. Furthermore, a good contact distribution will increase the contact area and therefore increase the traction of the tire. An

even load distribution will also allow the tire to wear more evenly.

The contact stress distribution of the tire with a load of 500 kg and an inflation pressure of 300 kPa is shown in Figure 6.5. The contact stress distribution was not ideal for this operating condition, taking into account that only three of the five grooves on the tire was in contact with the cylinder. Therefore, the tire will not wear evenly and the traction of the tire will not be optimal. The undesirable load distribution could be due to different factors, including: the sidewall or tread being too stiff, or the tire not being operated at the optimal inflation pressure for the applied load. Thus, the inflation pressure of the tire should be lowered in order to find a better contact distribution for the applied load.

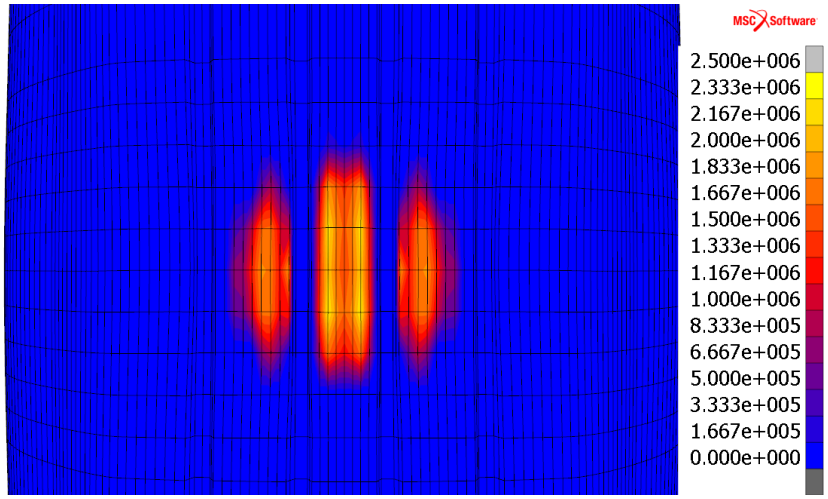

Figure 6.5: Contact stress distribution (Pa) of the tire under a load of 500 kg and a pressure of 300 kPa

Figure 6.6 shows the contact stress distribution of the tire for a load of 500 kg and an inflation pressure of 100 kPa. The contact stress distribution was better for these operating conditions. However, the tire bent away from the cylinder in the middle of the tread, leading to lower contact stress in the middle of the tread. The tire deformed so much under the load that the stiffness of the tread or the sidewall pushed the middle of the tread upwards. The problem could be solved by increasing the inflation pressure of the tire, resulting in a decreased tire deformation.

The contact stress distribution of the tire under a load of 700 kg and an inflation pressure of 300 kPa is shown in Figure 6.7. The contact distribution in this case was sufficient, because the contact area was large and the contact stress is distributed over the tread area. Therefore, the tire will wear evenly and it will also have optimal traction.

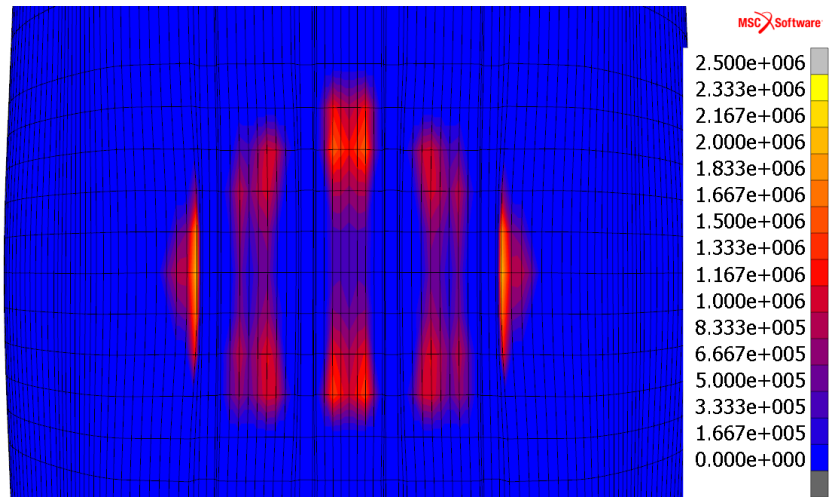

Figure 6.6: Contact stress distribution (Pa) of the tire under a load of 500 kg and a pressure of 100 kPa

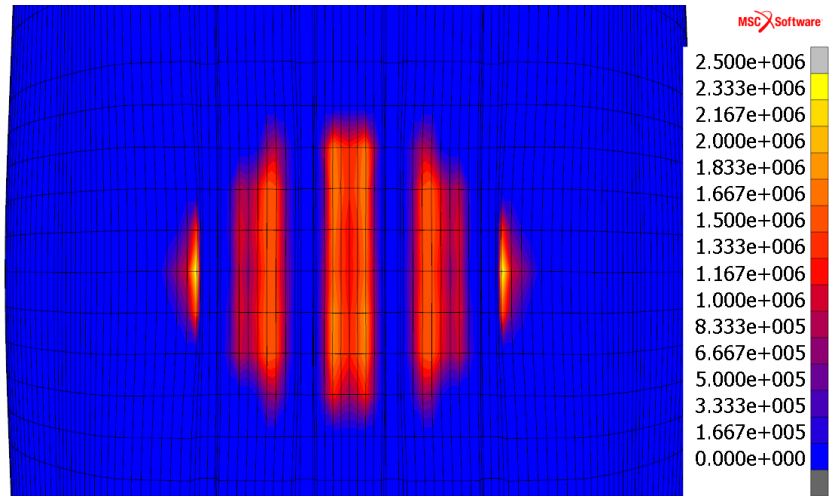

Figure 6.7: Contact stress distribution (Pa) of the tire under a load of 700 kg and a pressure of 300 kPa

6.1.2 Rolling Analysis Results

In the rolling analysis the displacement of the rigid cylinder was used to apply the load to the tire. After the load was applied, the tire was rolled for approximately two revolutions. The elastic strain energy density was then extracted for the last revolution of the tire, at the section shown in Figure 6.8.

The elastic strain energy density, when the extraction point was in contact with the cylinder, for a load of 500 kg and inflation pressure of 300 kPa is shown in Figure 6.9. The elastic strain energy density was concentrated where the tread was in contact with the cylinder, but there were also concentration points where the steel belt plies ended and at the root of the outside grooves.

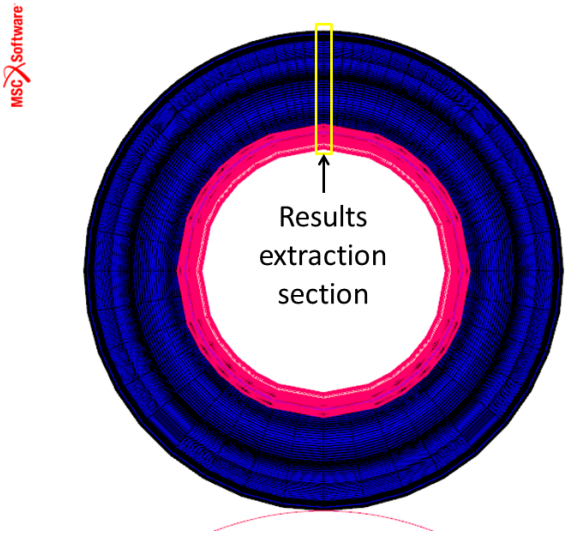

Figure 6.8: Results extraction section for rolling analysis

Elastic strain energy density was the highest where the tire was in contact with the rim, due to the local deformation being high in the bead. The elastic strain energy density, of the nodes shown in Figure 6.9 for one revolution of the tire, was plotted in Figure 6.10. The plot showed the increase in strain energy when the tire started to deform before it came in contact with the cylinder. Node 13 had almost zero strain energy until the tire started to deform, while the other two node's strain energy decreased to almost zero after deforming back and then started to rise again before the tire deformed again.

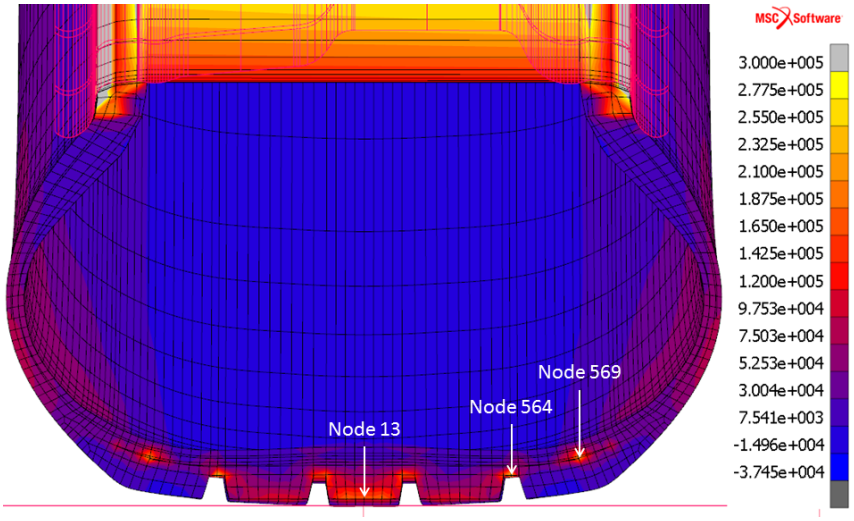

Figure 6.9: Elastic strain energy density (J/m^3) for a load of 500 kg, inflation pressure of 300 kPa and rolling velocity of 20 km/h

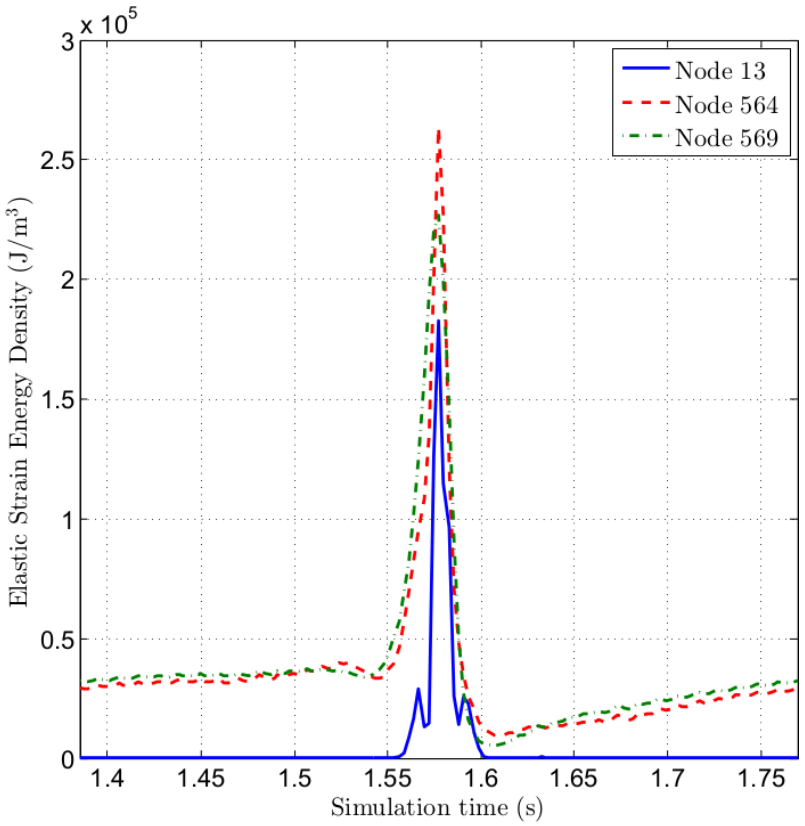

Figure 6.10: Plot of the elastic strain energy density, for one revolution, of three nodes for a load of 500 kg, inflation pressure of 300 kPa and rolling velocity of 20 km/h

The elastic strain energy density increased when the inflation pressure decreased to 100 kPa, as shown in Figure 6.11. This increase in strain energy density was expected due to the tire deforming more when the inflation pressure was decreased. The distribution of the elastic strain energy density stayed relatively identical in the tread area, but the highest elastic strain energy density were at the roots of outside grooves and not at the bead of the tire.

To ensure that the rolling velocity of the tire during the rolling analysis did not have an effect on the elastic strain energy density, the tire was also simulated at a rolling velocity of 60 km/h, instead of 20 km/h used for the other simulations. The elastic strain energy density of the tire at a rolling velocity of 60 km/h with a load of 500 kg and an inflation pressure of 300 kPa, is shown in Figure 6.12. If the elastic strain energy density is compared to that in Figure 6.9, the average difference is 2,15 %. Thus, the rolling velocity during the rolling analysis did not have a significant effect on the elastic strain energy density in the tire.

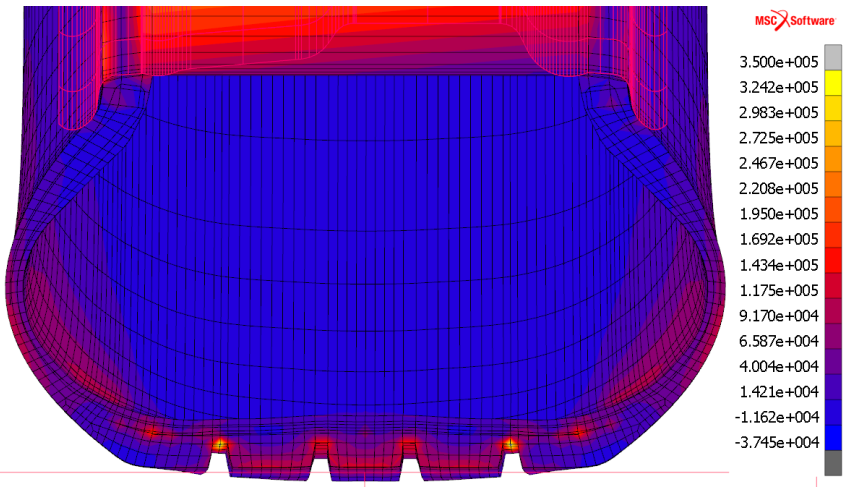

Figure 6.11: Elastic strain energy density (J/m^3) for a load of 500 kg, inflation pressure of 100 kPa and rolling velocity of 20 km/h

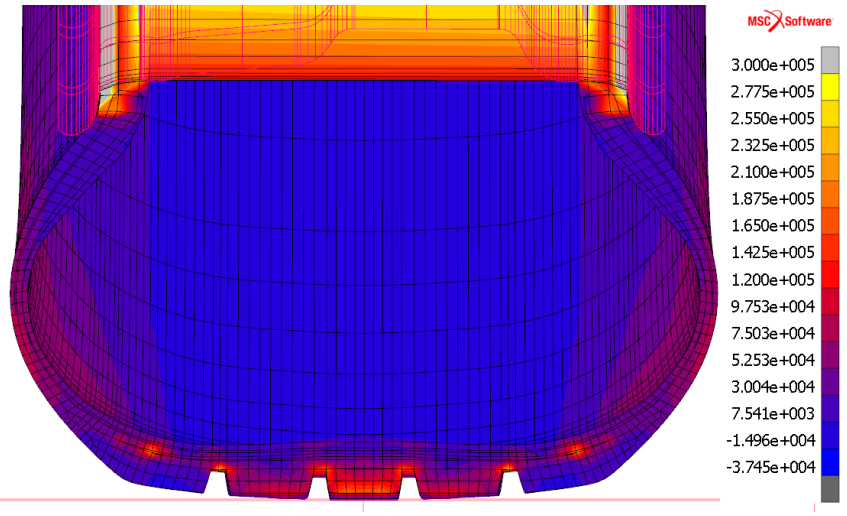

Figure 6.12: Elastic strain energy density (J/m^3) for a load of 500 kg, an inflation pressure of 300 kPa and rolling velocity of 60 km/h

6.2 Thermal Analysis Results

The heat generated during the rolling of the tire was applied during the thermal analysis in order to calculate the temperature distribution inside the tire. The heat generation varied with the inflation pressure, the load, and the speed the tire is rolling at; therefore, the temperature distribution also varied. In the following section the temperature distribution obtained from the different operating conditions will be discussed.

The temperature distribution in the tire for a load of 500 kg, an inflation pressure of 300 kPa and a rolling velocity of 60 km/h is shown in Figure 6.13. The high temperatures were in the middle of the tread and at the bead of the

tire. The high temperature in the middle of the tread was due to the large deformation in the middle of the tread, as Figure 6.2 showed. Furthermore, the high temperature in the bead was due to the load being concentrated on the small point that pushed against the safety hump during the rolling of the tire.

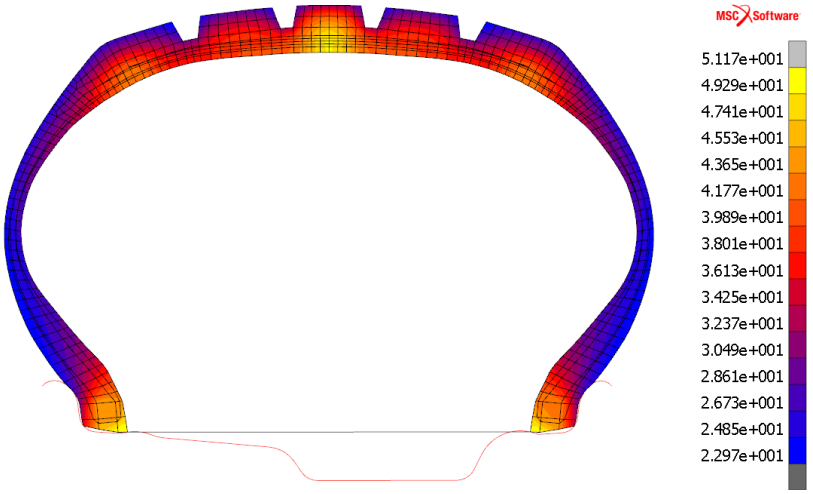

Figure 6.13: Temperature distribution (°C) for a load of 500 kg, an inflation pressure of 300 kPa and rolling velocity of 60 km/h

When the inflation pressure was decreased to 100 kPa, the temperature in the tire increased, as shown in Figure 6.14. However, the profile of the temperature distribution was relatively identical. The increase in deformation of the tire thus leads to an increase in temperature, but does not have a significant effect on the temperature distribution profile.

The temperature distribution on the inside edge of the tire for a load of 500 kg, rolling velocity of 60 km/h and different inflation pressures, is plotted in Figure 6.15. The results in Figure 6.15 are plotted along the path A-B as shown in Figure 6.16. The temperature profile on the inside edge of the tire stayed the same for different inflation pressures. However, when the inflation pressure was decreased from 300 kPa to 100 kPa, the average temperature between the A-B path increased by 5,3 °C. The temperature for the 450 kPa inflation pressure was higher in the middle due to a small area carrying the load and thus deforming more, while the temperature was lower before the shoulder due to less deformation.

When the load was decreased to 300 kg and the rolling speed remained 60 km/h, the temperature distribution profile stayed relatively the same for the different pressures, as shown in Figure 6.17. However, the temperature for the 100 kPa inflation pressure was higher before the shoulder due to the large deformation in that area.

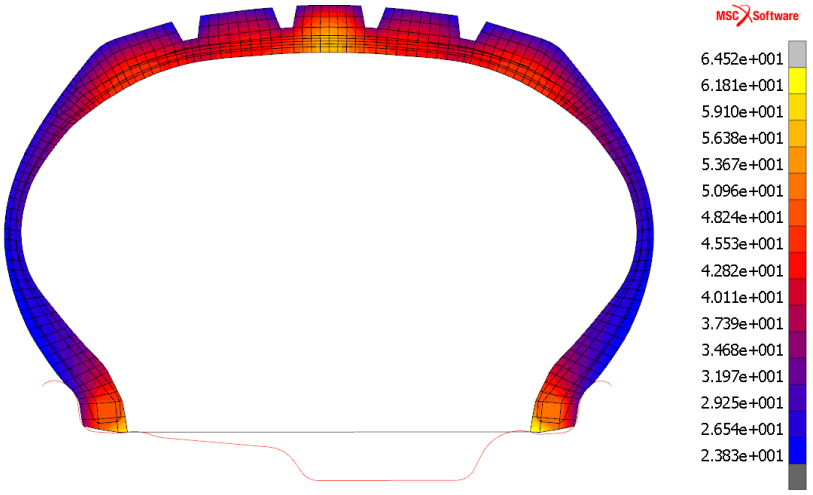

Figure 6.14: Temperature distribution (°C) for a load of 500 kg, an inflation pressure of 100 kPa and rolling velocity of 60 km/h

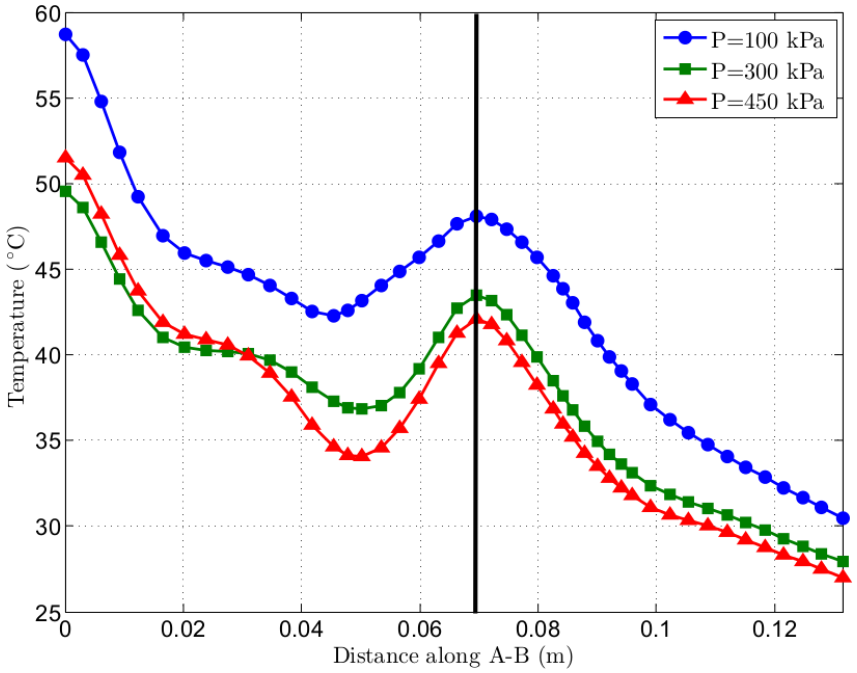

Figure 6.15: Temperature distribution along path A-B for a load of 500 kg, rolling velocity of 60 km/h and different inflation pressures

The temperature distribution for an inflation pressure of 300 kPa, rolling velocity of 60 km/h and different loads, is plotted along path A-B in Figure 6.18. The temperatures increased as the load on the tire is increased, because the tire deformed more under the high load. Furthermore, as the load increased, the temperature at the shoulder of the tire also increased compared to the temperature in the tread. The temperature increase in the shoulder was

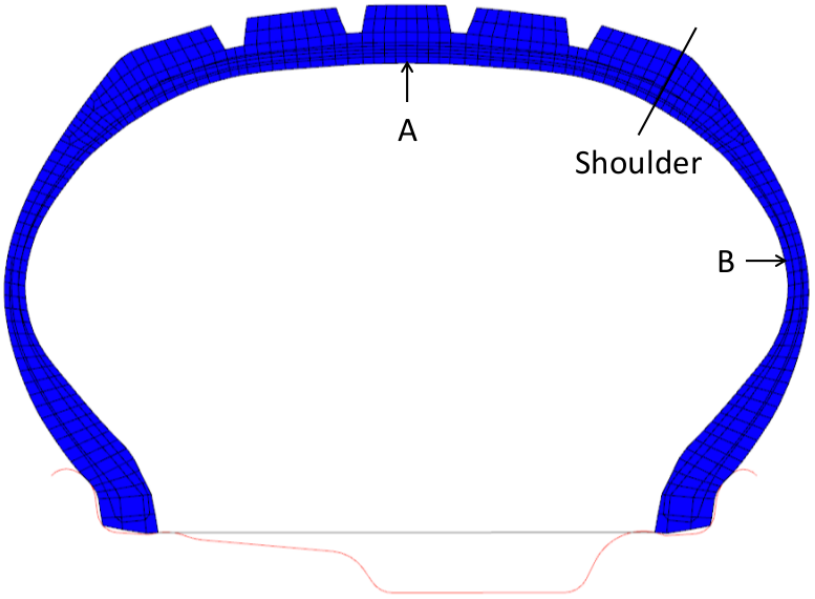

Figure 6.16: Plot path A-B for temperature distribution

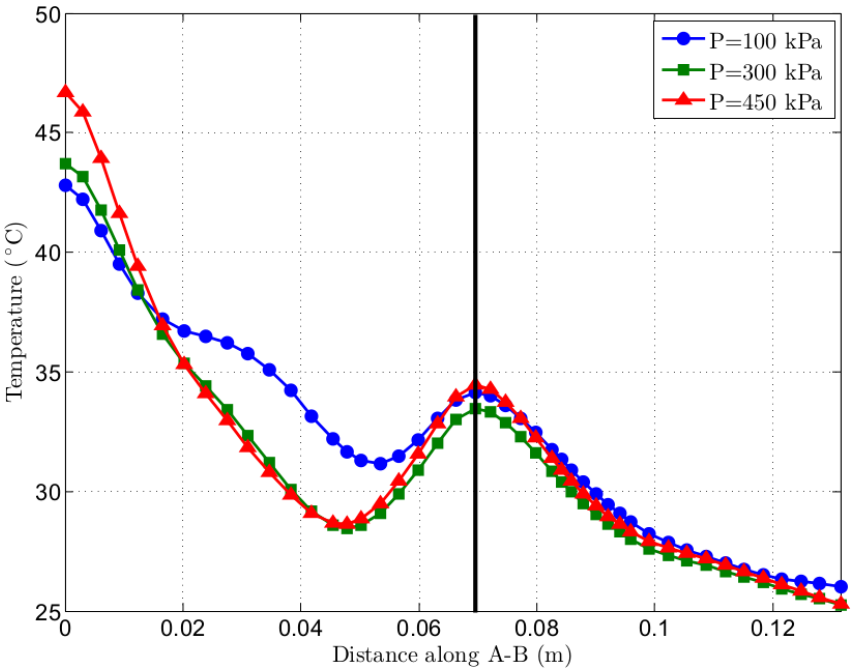

Figure 6.17: Temperature distribution along path A-B for a load of 300 kg, rolling velocity of 60 km/h and different inflation pressures

due to the increase in deformation in the shoulder of the tire under the higher load.

The temperature distribution along path A-B of the tire for a load of 500 kg, with inflation pressure of 300 kPa and different rolling velocities, is plotted in

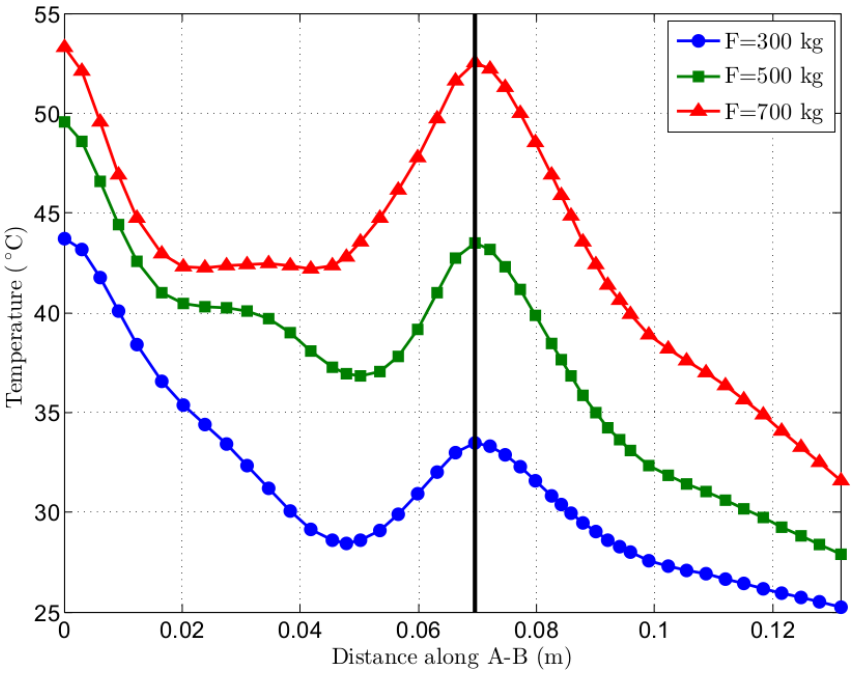

Figure 6.18: Temperature distribution along path A-B for an inflation pressure of 300 kPa, rolling velocity of 60 km/h and different loads

Figure 6.19. The temperatures increased as the rolling velocity of the tire increased, since the rate of deformation increased proportional to the rolling velocity of the tire. However, the distribution profile did not change with an increase in rolling velocity.

The maximum temperature in the tire for a rolling velocity of 120 km/h at different loads and inflation pressures is shown in Table 6.2. The maximum temperature inside the tire for a rolling velocity of 120 km/h is 107,2 °C at a load of 700 kg and pressure of 100 kPa. The increase in temperature with an increase in inflation pressure for a load of 300 kg was due to the deformation of the tire being concentrated in the middle of the tire. This deformation was more concentrated with the higher inflation pressures and led to the higher temperature.

Lastly, the temperature distribution along path A-B of the tire for a load of 500 kg, inflation pressure of 300 kPa, rolling velocity of 60 km/h and different ambient temperatures, are plotted in Figure 6.20. The temperatures in the tire increased linearly as the ambient temperature increased, due to the convection heat transfer being a linear function. Therefore, the profile of the temperature distribution stayed the same with the increase in ambient temperature.

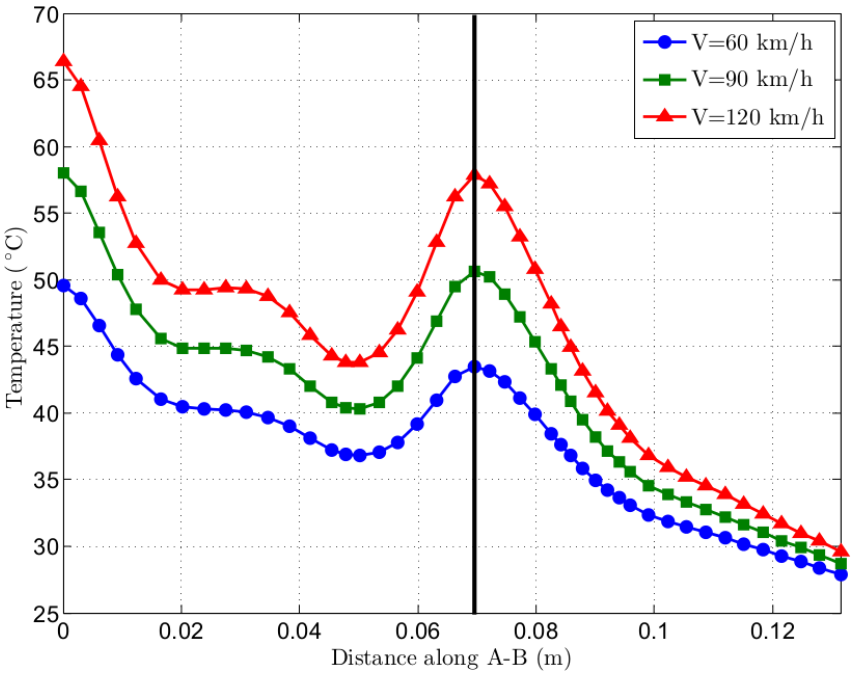

Figure 6.19: Temperature distribution along path A-B for a load of 500 kg, inflation pressure of 300 kPa, and different rolling velocities

Table 6.2: Maximum temperature in tire with a rolling velocity of 120 km/h and different loads and inflation pressures

Load (kg)	Inflation pressure (kPa)	Max temperature (°C)
300	100	57,7
	300	59,7
	450	65,7
500	100	87,7
	300	67,5
	450	74,6
700	100	107,2
	300	77,7
	450	79,7

6.3 Conclusion

The results from the numerical analysis showed that the temperature distribution, deformation and contact stress distribution in the tire are influenced by the load, pressure and rolling velocity applied to the tire. The deformation and displacement of the tire become larger as the load is increased and the inflation pressure is decreased. Furthermore, the amount of displacement in

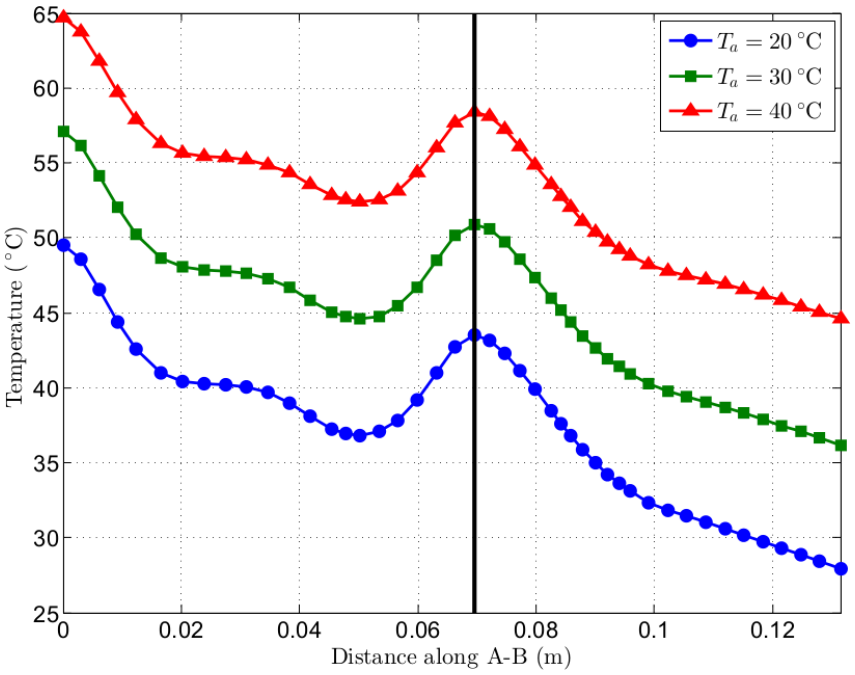

Figure 6.20: Temperature distribution along path A-B for a load of 500 kg, inflation pressure of 300 kPa, rolling velocity of 60 km/h and different ambient temperatures

the tire affects the contact stress distribution. If the displacement of the tire is too large, the contact stress distribution is not optimal, because the tire bends away from the contact in the middle of the tread. Also, if the displacement is too small, the contact stress distribution is not ideal, because the whole tread area is not utilised and the tire will wear unevenly. Therefore, the inflation pressure must be optimised to ensure adequate deformation for the applied load. The temperature in the tire increased with an increase in deformation, rolling velocity and ambient temperature. Therefore, if the load is increased and the inflation pressure decreased the temperature distribution changes and the maximum temperature increases. The rolling velocity of the tire and the ambient temperature influences the maximum temperature in the tire, whereas the load and inflation pressure influences the distribution of the temperature.

Chapter 7

Experimental Data and Comparison

The numerical model was validated by executing three experimental tests on the actual tire. The experimental tests included measuring the external and internal surface temperatures of the actual tire, the contact stress distribution at the contact point, the tire deformation when it is loaded, internal air pressure and internal air temperature. The operating conditions for the experimental tests were varied in the same way as the numerical model where the load, inflation pressure and rolling velocity of the tire were altered.

7.1 Tire Test Bench

The experimental tests were done on a test bench developed specifically for the testing of tires. The tire rotates against a cylinder, while the air flows over the tire to simulate the rolling of the tire on a vehicle. The test bench is shown in Figure 7.1. The tire was rotated by an electric motor controlled by a variable speed drive, while the tire was loaded with a 0,87 m diameter cylinder that can move up and down to alter the load on the tire. The position of the cylinder was controlled by a mechanical screw, while the load was measured by a load cell. The cylinder imitating the road surface is shown in Figure 7.2. A fan controlled by a variable speed drive moved the air over the tire. The temperature of the air flowing over the tire was controlled by heating elements in the air stream.

The rolling velocity, air velocity and air temperature were controlled by a control panel. The test bench measured the internal air temperature and the inflation pressure of the tire. The measuring devices on the test bench were calibrated before the test bench was used for any tests and are described in Appendix A.

Figure 7.1: Tire test bench

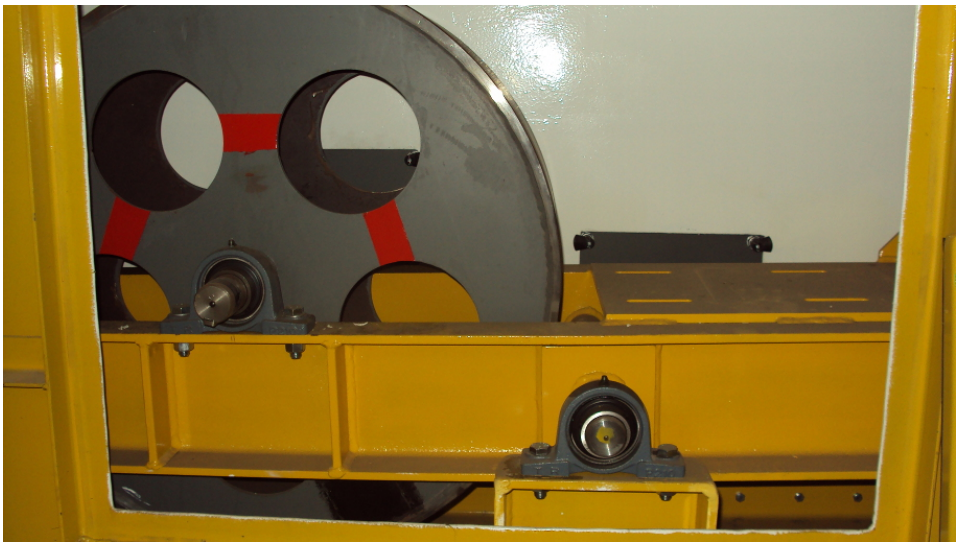

Figure 7.2: Cylinder imitating the road surface

7.2 Tire Deformation

Deformation of the actual tire was measured using digital image correlation (DIC). The DIC system takes pictures of the surface pattern applied to the tire as the tire deforms under the loading. The movement of the pattern is tracked in order to determine the deformation and strain field in the tire. The deformation and strain field calculation process is shown in Figure 7.3. For this study, the LaVision StrainMaster 2D/3D DIC hardware and DaVis software were used, with the specifications shown in Table 7.1.

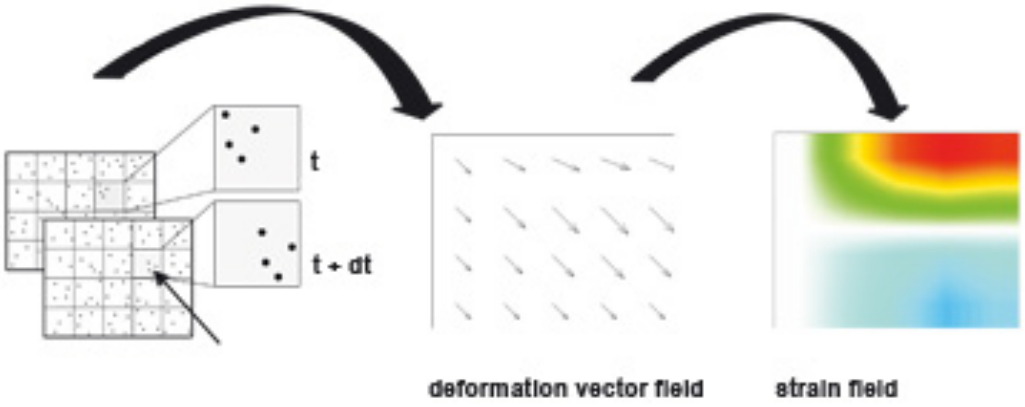

Figure 7.3: The DIC process to calculate the deformation and strain field (LaVision, 2014*a*)

Table 7.1: LaVision Strainmaster 2D/3D DIC specifications (LaVision, 2014*b*)

CCD Camera Resolution (pixels)	1 600 × 1 200
CCD Camera Dynamic (bit)	12
CCD Camer Shutter Gate (μs)	1
Repetition rate (frames/s)	30
Accuracy	down to 0,01 pixel 40 μstrain locally 3 μstrain globally
Optics	f=50 mm; 1:1,8

7.2.1 Experimental Setup

The test bench was used to apply the load on the tire with the door section removed, seeing that it was obstructing the deformation zone. The brake on the test bench was engaged, so the tire could not rotate during the loading.

The first step in the experimental setup was to create a pattern on the tire, so the DIC software could track the deformation. Three different colour spray paints were used to create a pattern on the tire, namely white, black and grey. White speckles were sprayed on first followed by grey speckles and lastly black speckles. The speckle pattern on the tire is shown in Figure 7.4.

The next step was the setup of the DIC hardware by moving and changing the orientation of the cameras and the light sources until the deformation zone was captured. After that, the camera focus and aperture were fine-tuned to make sure that the deformation zone was in focus and the dynamic range was not saturated. The dynamic range must ideally be around 11 bit. The setup of the hardware is shown in Figure 7.5.

Lastly, the cameras were calibrated using a calibration plate. One image was taken, with the calibration plate in front of the tire and is shown in

Figure 7.4: The speckle pattern sprayed on the tire

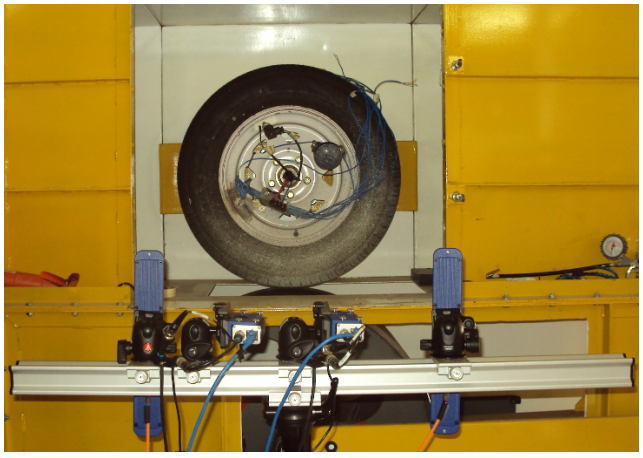

Figure 7.5: The DIC hardware setup with the speckled tire in the middle

Figure 7.6. The image was processed and the system calibrated using the `Strain Calibration` option in DaVis. The system setup and calibration were acceptable if the average deviation of the calibration image for each camera was less than 0,5 pixels. The average deviation for the test setup was 0,44982 pixels and 0,47986 pixels for camera one and two respectively. Therefore, the setup and calibration were acceptable.

7.2.2 Experimental Procedure

The camera frame rate for the experimental test was set to 1 Hz, while the illumination was set to 3 000 μs. A pre-test analysis was done where five images was taken with no deformation, to ensure that the DIC software can map and track the speckle pattern on the tire. The pre-test images were processed using

Figure 7.6: The calibration plate in front of the speckled tire

the `Surf. + Vectors` option in DaVis to determine the deformation and strain field of the tire.

The `Subset Size` and `Step Size` used in the image processing were altered, while the computation quality was kept `Accurate` in order to determine the most accurate processing parameters. The analysis area or mask was defined to calculate the deformation of the tire, with one seeding point inside the calculation area, as shown in Figure 7.7. The images were processed using the `Relative To First` option, where the deformation and strain were calculated relative to the first specified image. After the deformation and strain fields were calculated, the absolute root mean square (rms) of the displacement for the five images was determined from the deformation field. The absolute rms of the displacement give an indication of how accurate the system can measure zero deformation. The results for different processing parameters are shown in Table 7.2.

Table 7.2: Absolute rms displacement with zero deformation for different processing parameters

`Subset Size` (pixel)	`Step Size` (pixel)	rms $\lvert\delta\rvert$ (μm)
30	15	8,93265
60	30	5,42125
120	30	4,17203
120	10	4,08734

The results indicated that when the `Subset Size` was increased, the absolute rms of the displacement decreased and therefore, the accuracy increased.

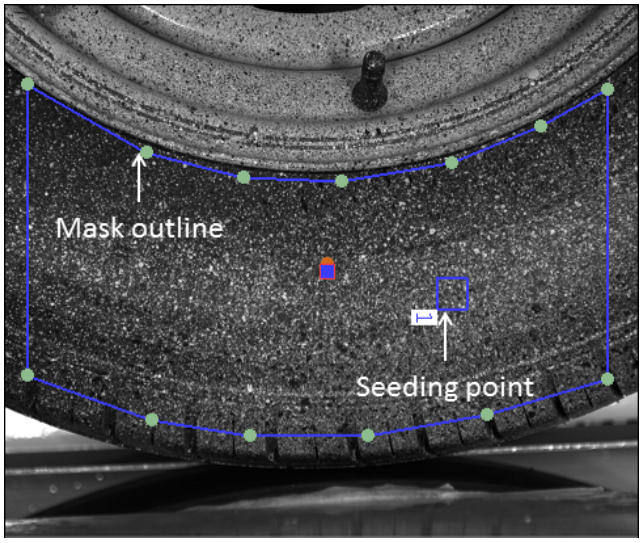

Figure 7.7: The mask and seeding point specified in the calculation area

However, the resolution of the results decreased with an increase of `Subset Size`. Therefore, the `Step Size` must be decreased to obtain results with a higher resolution. The difference in resolution for a `Step Size` of 30 pixels and 10 pixels, when the `Subset Size` was 120 pixels, is shown in Figure 7.8. A `Subset Size` of 120 pixels, `Step Size` of 10 pixels and an `Accurate` computation quality was used as processing parameters in the DaVis software.

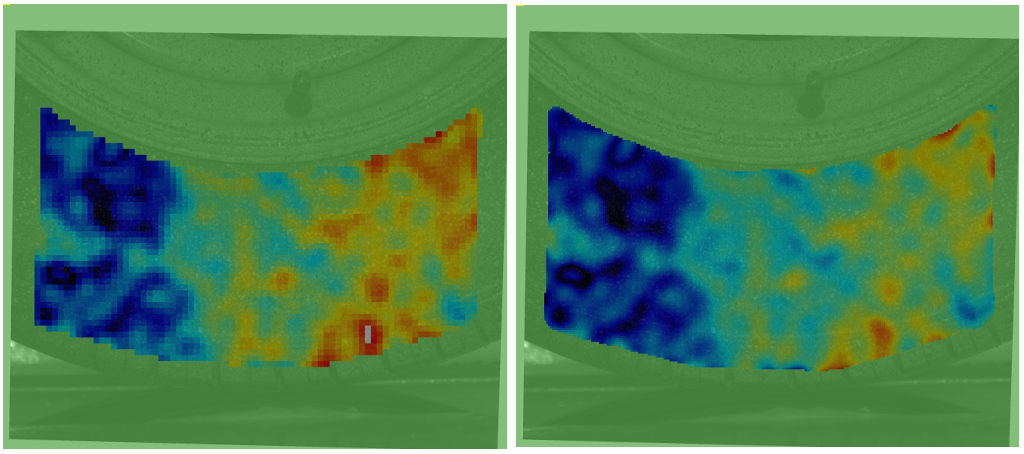

(a) `Step Size` of 30 pixels (b) `Step Size` of 10 pixels

Figure 7.8: The difference in resolution for a `Subset Size` of 120 pixels and different `Step Sizes`

After the pre-test, the tire was inflated to the desired operating pressure. The image capturing started and the load was applied by adjusting the position of the cylinder with the mechanical screw. This process was repeated for

different operating conditions. Thereafter, the captured images were processed using the `Surf. + Vectors` option in DaVis, calculating the deformation and strain field. The images before the start of deformation and the images after deformation were cut off, because there was no change in deformation in these images. The mask and seeding point were the same as for the pre-test image processing.

7.2.3 Results

The deformation measured by the DIC analysis for a load of 500 kg and an inflation pressure of 300 kPa is shown in Figure 7.9. The tire deformed the most in the sidewall, with a maximum deformation of 8,8 mm. The region just under the sidewall showed a large displacement due to the deformation of the sidewall under the load. When the pressure was decreased to 100 kPa, the maximum deformation in the sidewall increased to 22 mm, as seen in Figure 7.10. When the load and pressure was increased to 700 kg and 450 kPa respectively, as shown in Figure 7.11, the deformation of the tire was relatively close to the deformation for a load of 500 kg and an inflation pressure of 300 kPa. The measured results showed that the deformation of the tire was symmetric over the middle of the contact region.

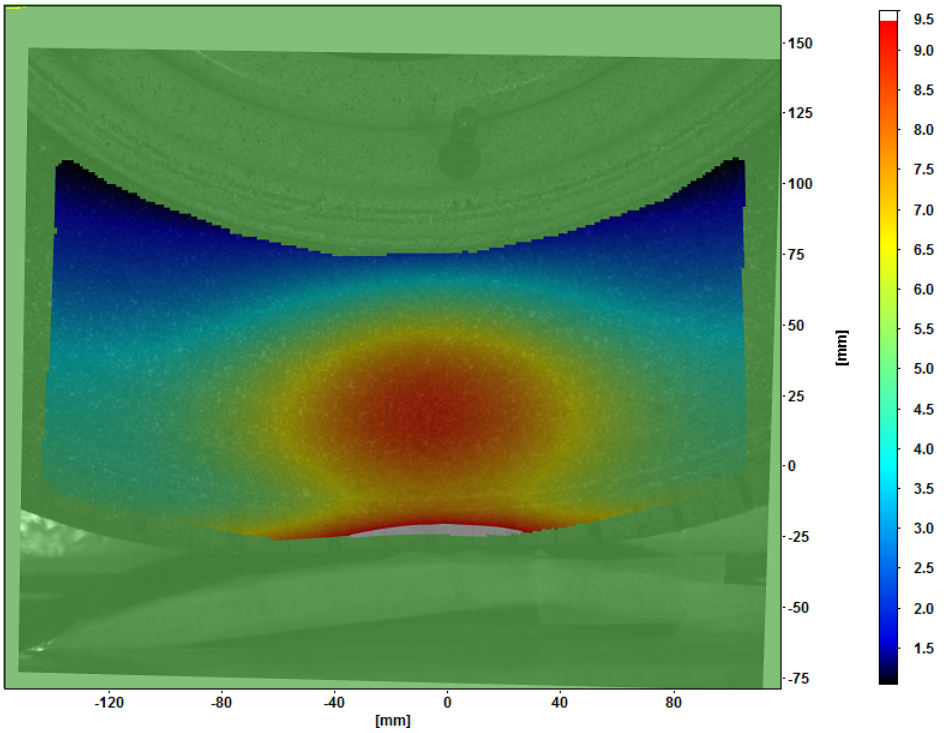

Figure 7.9: Deformation (mm) of the tire for a load of 500 kg and an inflation pressure of 300 kPa

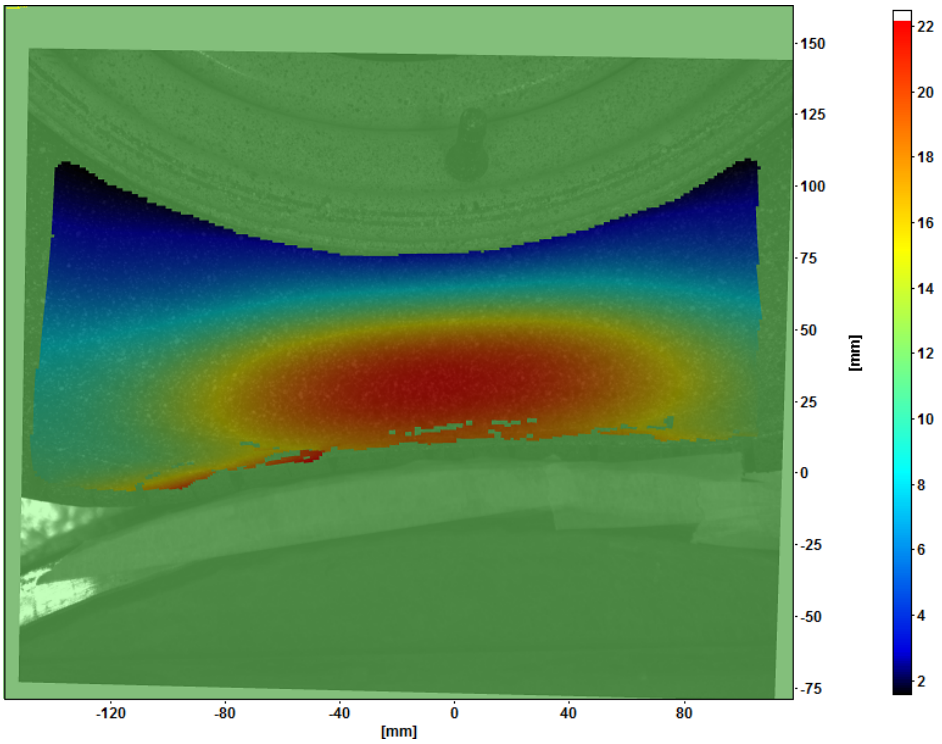

Figure 7.10: Deformation (mm) of the tire for a load of 500 kg and an inflation pressure of 100 kPa

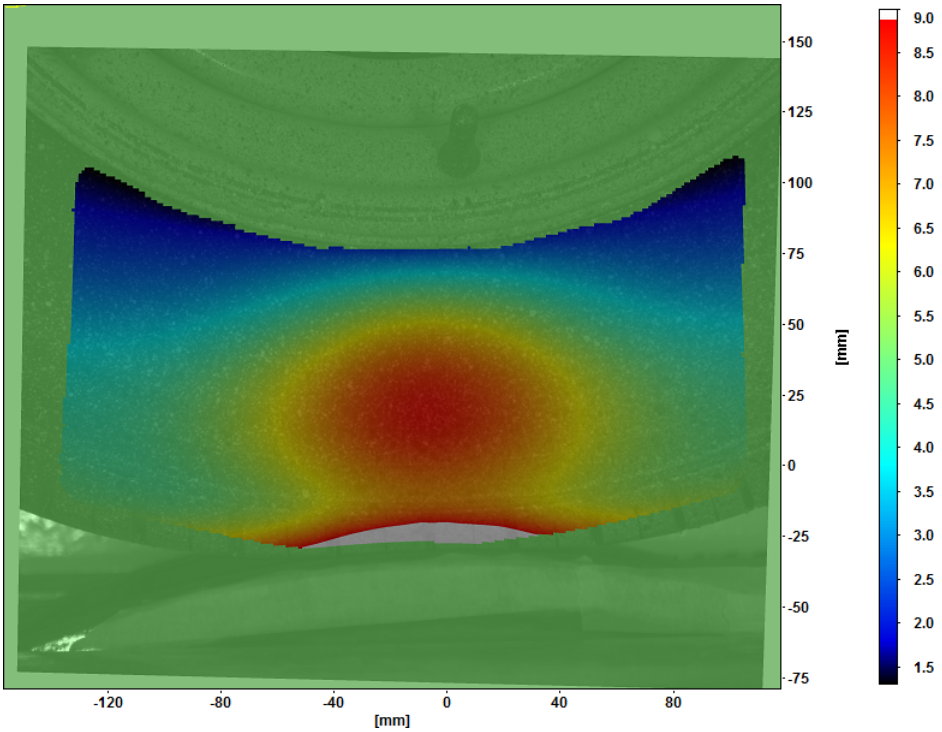

Figure 7.11: Deformation (mm) of the tire for a load of 700 kg and an inflation pressure of 450 kPa

7.2.4 Tire Deformation Comparison

The sidewall deformation of the tire calculated by the numerical model was validated by comparing it to the actual deformation of the tire measured by the DIC analysis. The numerical deformation results were negative at certain nodes, seeing that it was the difference in deformation from after inflation to after loading.

The deformation of the numerical model was less that the actual deformation, as shown in Figure 7.12. However, if the shape and the location of the deformation field are compared, it is identical, with the maximum deformation in the sidewall. The displacement of the nodes at the beginning of the shoulder due to the deformation of the sidewall was also seen in the numerical model. The results were similar when the pressure was decreased to 100 kPa, as seen in Figure 7.13. The maximum displacement of the sidewall in the numerical model and the actual tire, for the different operating conditions, is summarised in Table 7.3. The comparison between the numerical and actual sidewall deformation revealed the rubber used in the modelling of the sidewall was too stiff and prevented the sidewall from deforming. The stiff rubber used for the modelling of the tread, was also used to model the sidewall. Therefore, the sidewall and tread should be modelled using rubber with different stiffness values. These results show the measurement of the material properties, used in the manufacturing of the tire, is important in order to get the correct material properties and ultimately accurate deformation.

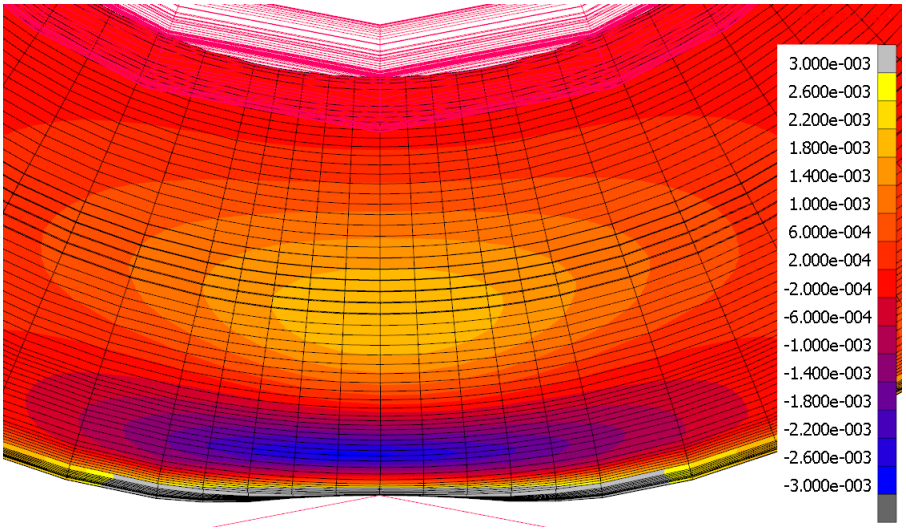

Figure 7.12: Sidewall deformation (m) of the tire for a load of 500 kg and an inflation pressure of 300 kPa

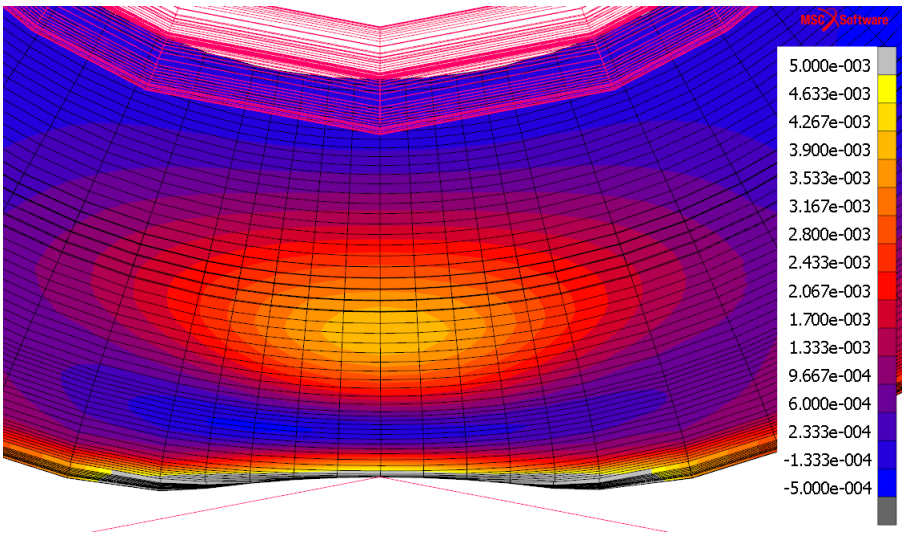

Figure 7.13: Sidewall deformation (m) of the tire for a load of 500 kg and an inflation pressure of 100 kPa

Table 7.3: Maximum displacement of sidewall for different operating conditions

Load (kg)	Inflation Pressure (kPa)	Actual Displacement (mm)	Numerical Model Displacement (mm)	% difference
300	100	12,4	1,9	84,68
500	100	22,0	6,1	72,27
	300	8,8	2,2	75,00
	450	5,7	1,6	71,93
700	300	13,0	4,2	67,69
	450	8,8	2,4	72,72

7.3 Contact Stress

The contact stress distribution between the tire and the cylinder was measured using a pressure mapping system. The Tekscan I-Scan® Evolution mapping system was used for this purpose. The system consists of a sensor, data acquisition electronics and software. The sensor used in this study was the 5150N model, shown in Figure 7.14, with specifications summarised in Table 7.4. A sensel, referred to in the table, is also referred to as a sensing element.

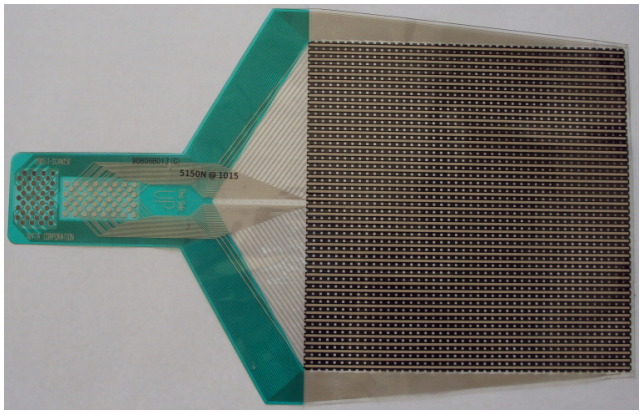

Figure 7.14: Tekscan 5150N pressure sensor

Table 7.4: Tekscan 5150N pressure sensor specifications (Tekscan, 2014)

Matrix Width (mm)	165,1
Matrix Height (mm)	165,1
# Columns	44
# Rows	44
Total # of Sensels	1 936
Resolution (Sensel per cm^2)	7,1
Pressure Range (MPa)	6,998

7.3.1 Experimental Setup

The test bench was used to apply the load on the tire, with the brake on the test bench engaged so the tire could not rotate during the loading. The load was applied to the tire by changing the position of the cylinder with the mechanical screw. The sensor was placed between the tire and the cylinder, as shown in Figure 7.15. The sensor was held in position by sticking it with masking tape to the cylinder, to ensure no movement was possible while the load was applied.

7.3.2 Experimental Procedure

The first step was to inflate the tire to a pressure of 300 kPa. The next step was to calibrate the sensor for the different operating loads by applying a known load to it. The calibration load had to be ±20 % of the operating load. The sensor was calibrated using the `Linear Calibration` option in the Tekscan software. This option performs a linear interpolation between zero load and the calibration load (Tekscan, 2009). Furthermore, the calibration load and loaded sensels were used to calculate the average applied pressure on the sensor. The sensitivity of the system was set to `High` for all the tests. The operating and calibration loads used to calibrate the sensor are shown in

Figure 7.15: Sensor placed between tire and cylinder.

Table 7.5. After the calibration was done, the calibration file for the operating load was loaded. After this, the tire contact stress distribution was determined for the operating load and different inflation pressures. This step was repeated for all the operating loads.

Table 7.5: Loads used for the calibration of the sensor

Operating Load (kg)	Calibration Load (kg)
300	350
500	550
700	750

7.3.3 Results

The contact stress distribution showed how uniform the tire can distribute the load applied to it over the tread area. The results of the contact stress analysis were extracted and contour plots of the pressure between the tire and the drum were created.

The contact stress distribution for a load of 500 kg and an inflation pressure of 300 kPa is shown Figure 7.16. The tire distributed the contact stress uniform over the whole tread area, therefore creating optimal operating conditions. When the inflation pressure was decreased to 100 kPa, the contact stress on the shoulder of the tire was higher than in the middle (as shown by Figure 7.17). This showed the tire deformed too much, thus, the inflation pressure was too low for the applied load and the inflation pressure needed to be increased.

When the inflation pressure was increased to 450 kPa, the high contact stress shifted to the middle of the tire (as shown in Figure 7.18). The inflation pressure needed to be decreased in this case, in order for the tire to deform more so the tread could bend to distribute the load.

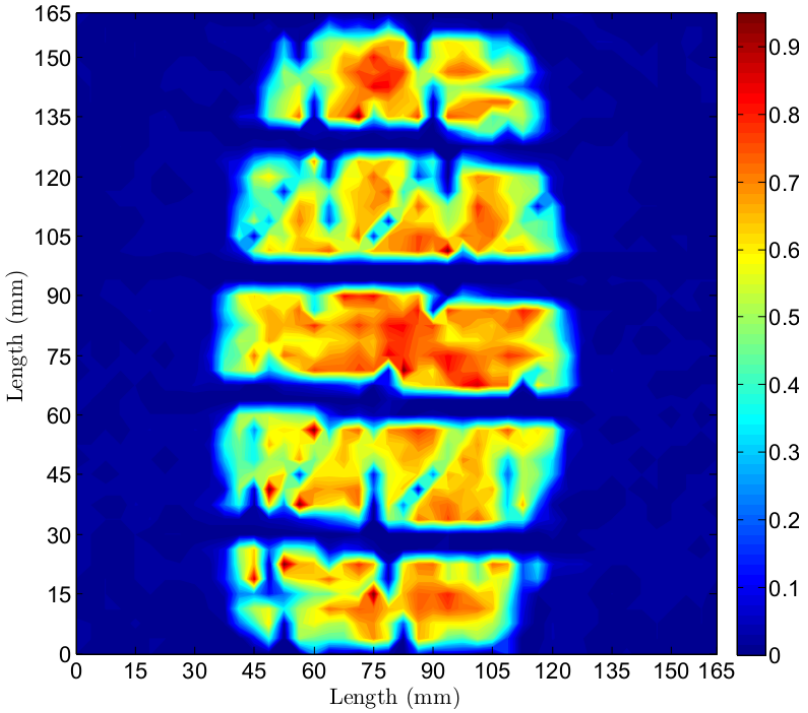

Figure 7.16: Contact stress distribution (MPa) of actual tire for a load of 500 kg and an inflation pressure of 300 kPa

7.3.4 Contact Stress Comparison

The results from the contact stress experimental test were compared to the contact stress distribution from the numerical loading analysis. This comparison indicated whether the stiffness in the tread and sidewall in the numerical tire model was too high or too low, by focusing on the shape of the distribution and the locations of high contact stress areas.

The contact stress distribution of the numerical model did not compare well to the actual tire, as Figure 7.19 shows. The contact area in the numerical model was smaller and this led to higher contact stress. When the inflation pressure was decreased to 100 kPa (as shown in Figure 7.20), the contact area of the numerical model was still smaller, but it was closer to the actual contact area. Also, the high contact stress areas for both are on the shoulder of the tire and it appeared as if the tire deformed upwards in the middle of the tread. The contact stress was also higher in the numerical model due to the contact area being smaller.

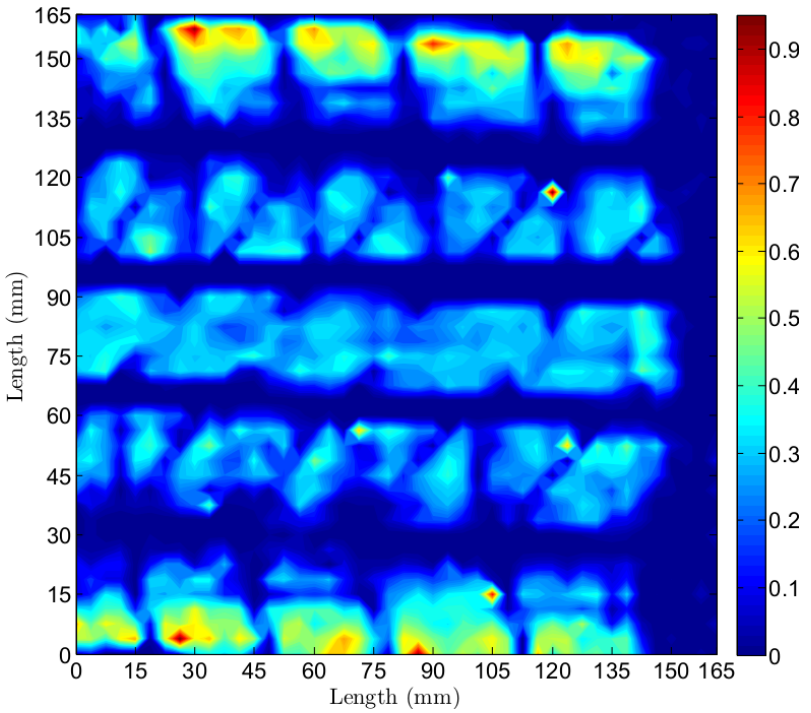

Figure 7.17: Contact stress distribution (MPa) of actual tire for a load of 500 kg and an inflation pressure of 100 kPa

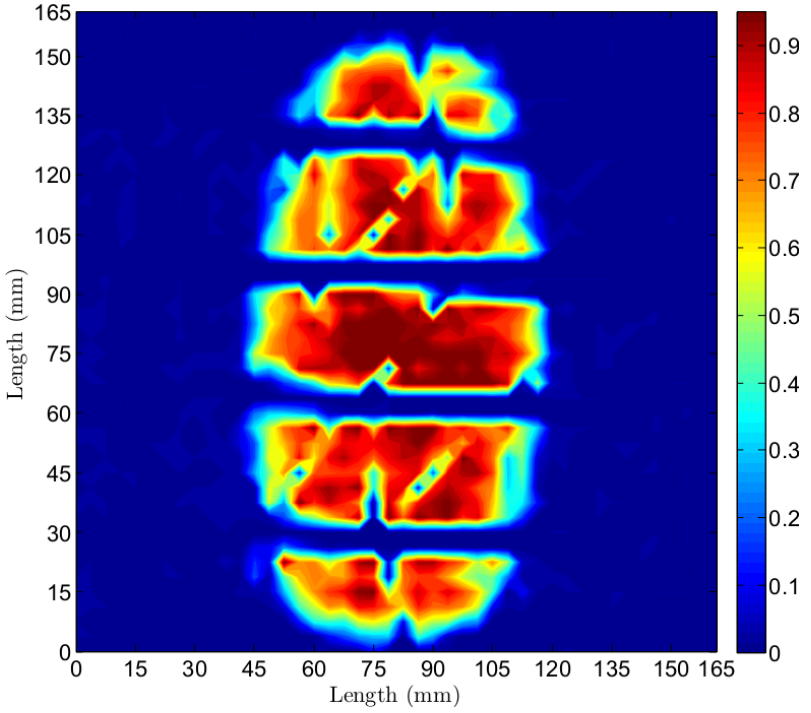

Figure 7.18: Contact stress distribution (MPa) of actual tire for a load of 500 kg and an inflation pressure of 450 kPa

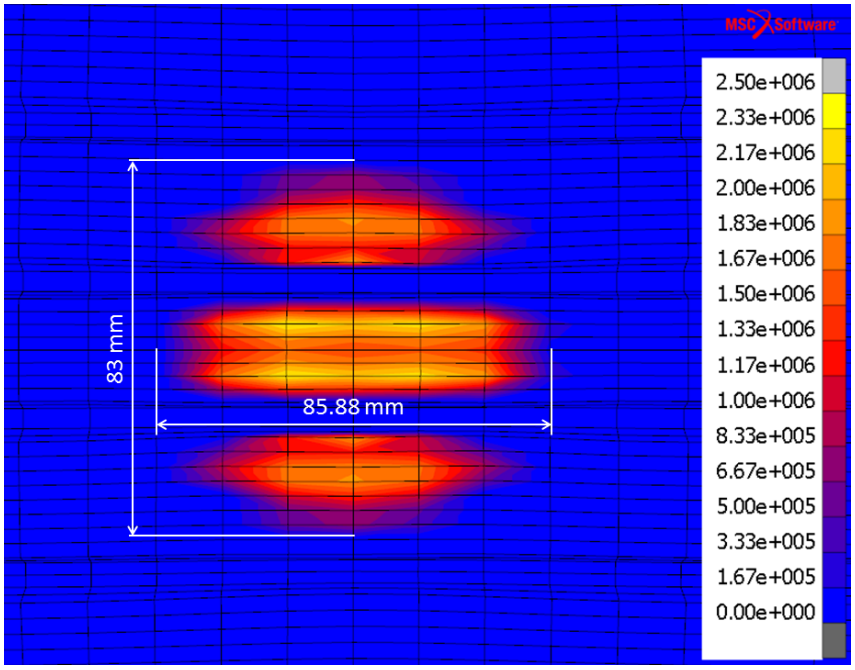

Figure 7.19: Contact stress distribution (Pa) for numerical model, with a load of 500 kg and an inflation pressure of 300 kPa

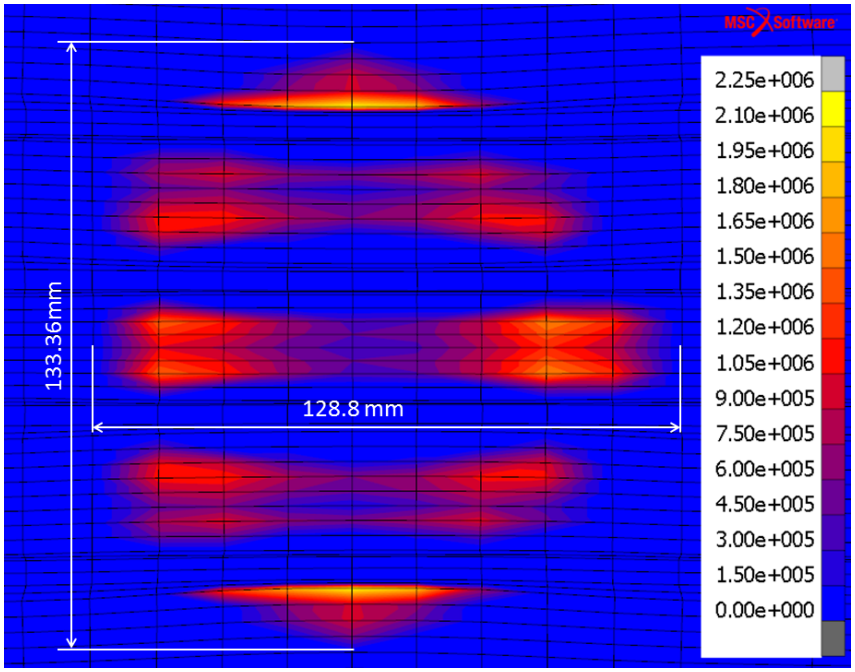

Figure 7.20: Contact stress distribution (Pa) for numerical model, with a load of 500 kg and an inflation pressure of 100 kPa

The comparison showed that the sidewall and the tread of the numerical model were too stiff. Therefore, the numerical model could not deform enough for the whole tread to be utilised in carrying the applied load. The materials contributing to the tire being too stiff may include: the rubber, body plies or steel belt plies. Therefore, the determination of the properties of these materials is important in order to get a representative numerical model.

7.4 External and Internal Surface Temperatures

The temperature of the tire was measured on both the external and the internal surfaces. The external surface temperatures were measured using a Flir E60 infrared camera, with the specifications shown in Table 7.6. The temperatures on the internal surface of the tire were measured by type-T thermocouples bonded to the surface. The temperatures measured during the experimental tests were compared to the numerical results, using the same operating conditions.

Table 7.6: Flir E60 specifications

IR Resolution (pixels)	320 × 240
MSX Resolution	320 × 240
Thermal Sensitivity (°C)	<0,05
Accuracy	±2 °C or ± 2 % of reading
Temperature range (°C)	-20 to 650

7.4.1 Experimental Setup

The test bench was not originally designed for the measurement of the internal surface temperatures of a tire, resulting in the test bench being modified in order to measure these temperatures. The thermocouples were bonded to the inside of the tire by flexible silicone-type glue, at two different sections around the circumference, 45 ° apart. At these sections, the temperature was measured at four locations in the axial direction. The four thermocouples, bonded to the tire at one of these sections are shown in Figure 7.21 and the exact positions of the thermocouples on the numerical model are shown in Figure 7.22. The eight thermocouples were connected to a data logger. A thermocouple glued to the middle of the tire, between the two circumferential positions, goes through the slip rings of the test bench and was connected to a multimeter. The thermocouples exited the tire through the rim and were

sealed by a gland welded onto the rim. The rest of the test bench stayed the same.

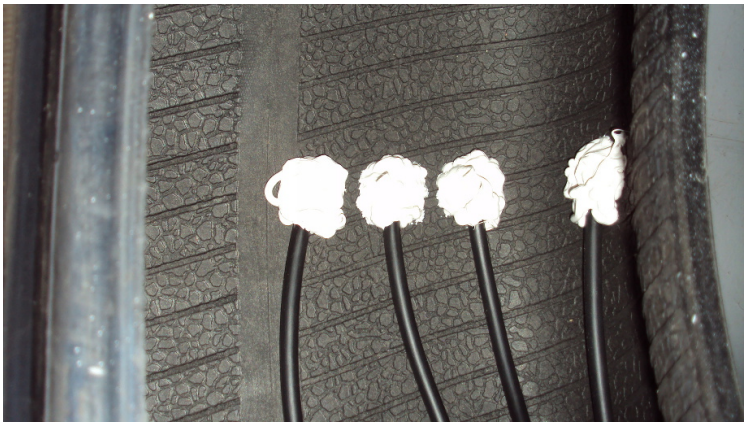

Figure 7.21: Thermocouples bonded to inside surface of tire

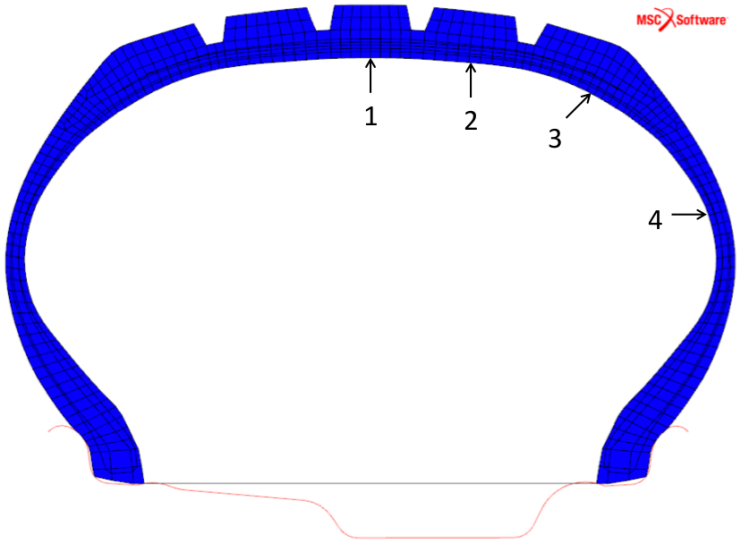

Figure 7.22: Position of thermocouples on numerical model

7.4.2 Experimental Procedure

First, the tire was inflated to the operating pressure needed for testing. This pressure could not be altered during the test, therefore, the pressure was fixed from the start to the end of the test. However, the pressure will increase if the tire is loaded and when the temperature of the air inside the tire increases. After the inflation was completed, the load was applied to the tire by changing the position of the cylinder pressing against the tire. The mechanical screw was

adjusted until the operating load was applied and the screw was then locked, therefore, the position could not change during the test. The load on the tire also increased when the tire started rolling, due to the rolling resistance of the tire.

The rest of the operating parameters were set using the control panel of the test bench. The rolling velocity of the tire and the air flowing over the tire was set to a 60 km/h. The air temperature used in the experimental tests was set to 20 °C. The test was done for a load of 500 kg and two pressures, 300 kPa for test one and 450 kPa for test two. The tests could only be conducted for these two operating conditions, seeing that, the thermocouple wires broke due to high cyclic fatigue.

The thermocouples connected to the multimeter and the temperature of the air inside the tire, measured by the control panel, were used to determine when the temperatures in the tire stabilised. After the temperatures stabilised, the test bench was stopped and the data logger was connected to the computer to log the maximum values measured during the tests. The temperatures could only be measured at the end of the tests and not during the test because the data logger must be connected to the computer in order to log the data. A wireless data logger would have made it possible to take readings during the test, but was not available with enough ports for all the thermocouples.

The temperatures on the sidewall and tread of the tire were measured using the infrared camera. The external temperatures were also measured when the temperatures stabilised and the test bench stopped. The camera was held about 2 m from the tire to measure the sidewall temperature and about 1 m from the tire to measure the tread temperature.

7.4.3 Results

The outside surface temperatures for the first test, measured by the infrared camera, are shown in Figure 7.23 and Figure 7.24. Figure 7.23 shows that the temperature distribution on the sidewall of the tire is relatively uniform from the bead to the shoulder, with a temperature around 33 °C. Furthermore, the temperature increased to around 35 °C at the shoulder and the bead of the tire. The temperature distribution on the tread was also relatively uniform, except for the middle region where the temperature was higher, with a maximum temperature of 45 °C at the root of the middle grooves, as Figure 7.24 shows.

The outside surface temperature distribution on the sidewall, for the second test looked similar to the temperature distribution for the first test, as Figure 7.25 shows. The temperature on the tread of the second test was not evenly distributed (see Figure 7.26). The temperature increased from the shoulder to the middle of the tread, where the maximum temperature was again in the middle grooves, reaching 47,2 °C.

The temperatures were not the only data gathered from the experimental test on the tire. The load of the tire while rolling, inflation pressure and the

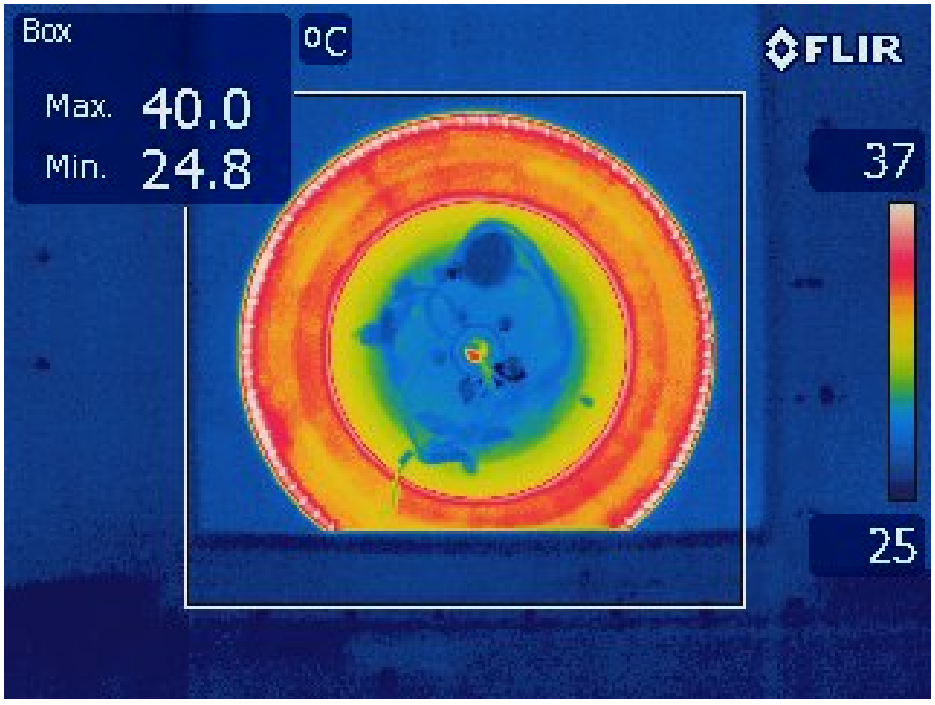

Figure 7.23: Temperature distribution (°C) on the sidewall of the tire for test one

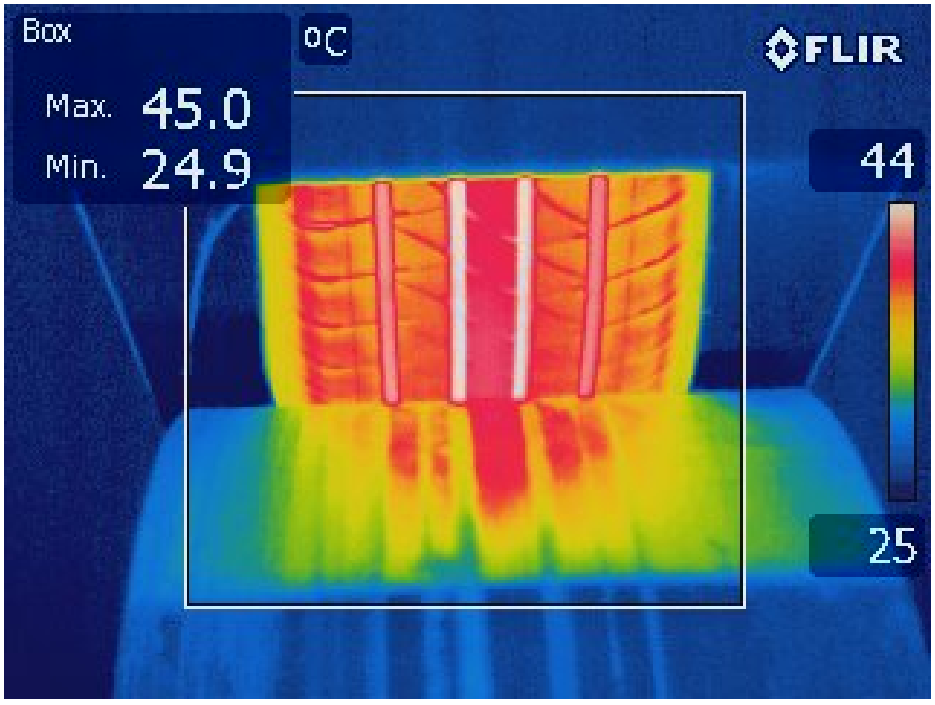

Figure 7.24: Temperature distribution (°C) on the tread of the tire for test one

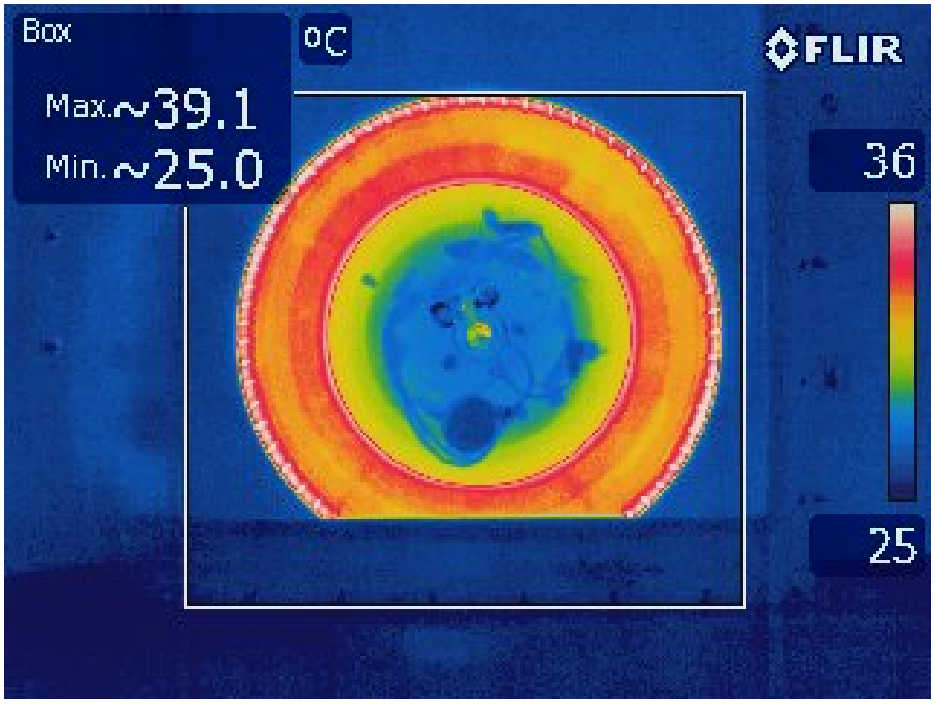

Figure 7.25: Temperature distribution (°C) on the sidewall of the tire for test two

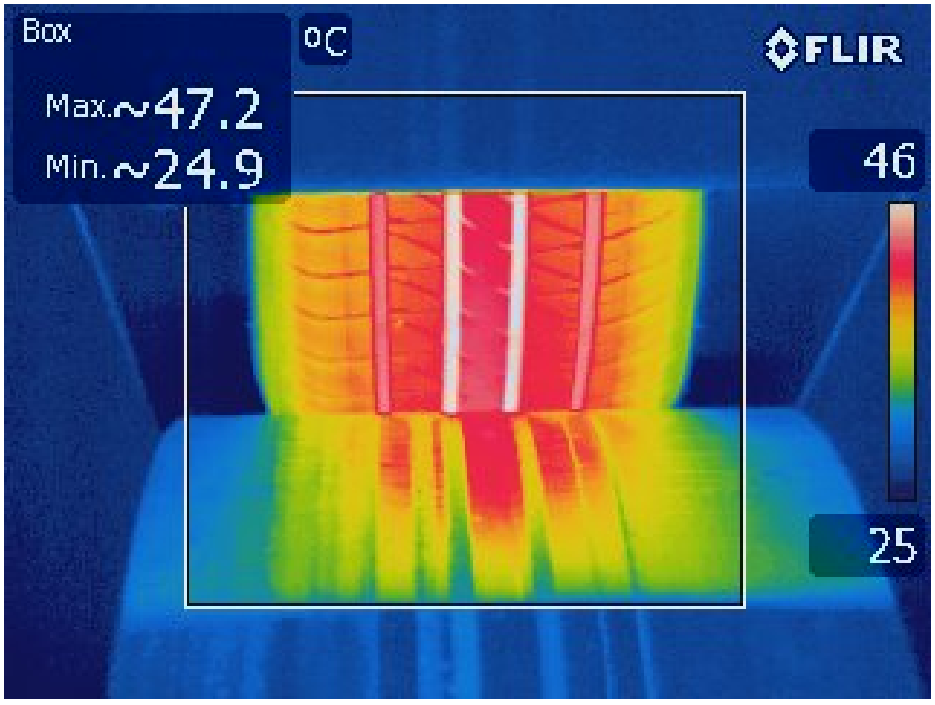

Figure 7.26: Temperature distribution (°C) on the tread of the tire for test two

temperature of the air inside the tire, after the temperatures stabilised, were also gathered. These results are shown in Table 7.7.

Table 7.7: Operating condition after temperatures stabilised

Test #	Load (kg)	Inflation pressure (kPa)	Air temperature (°C)
1	561,3	324,0	39,1
2	583,5	477,2	32,2

The temperatures measured by the thermocouples were averaged between the two sections. The temperatures measured on the inside surface of the tire at the two sections and the average are shown in Table 7.8. The thermocouple number refers to the numbers in Figure 7.22. The temperature on the inside surface of the tire was uniform in the tread region, while the temperature on the sidewall was lower than the temperature in the tread.

Table 7.8: Temperatures measured on the inside of the tire

Test #	Thermocouple #	Temperature section 1 (°C)	Temperature section 2 (°C)	Average temperature (°C)
1	1	45,6	46,4	46,0
	2	45,0	46,0	45,5
	3	46,4	46,6	46,5
	4	41,2	41,0	41,1
2	1	38,4	38,6	38,5
	2	36,1	36,5	36,3
	3	38,3	38,6	38,5
	4	34,3	34,1	34,2

7.4.4 External Surface Temperature Comparison

The temperatures on the external surface of the numerical model were compared to the temperatures measured by the infrared camera during the experimental tests. When the temperature distribution in Figure 7.27 is compared to the temperature distribution on the sidewall for the first experimental test, the high temperature regions for both are at the shoulder and the bead of the tire. However, the temperature distribution of the numerical model was not as uniform on the sidewall and the temperatures were also lower in the numerical model. When the inflation pressure was increased to 450 kPa, the comparison between the numerical model and experimental test was the same

as the 300 kPa case, as seen in Figure 7.28. The lower temperature in the numerical model was due to the rubber in the sidewall being too stiff. Therefore, the sidewall did not deform enough, which led to less heat generation and ultimately, lower temperatures.

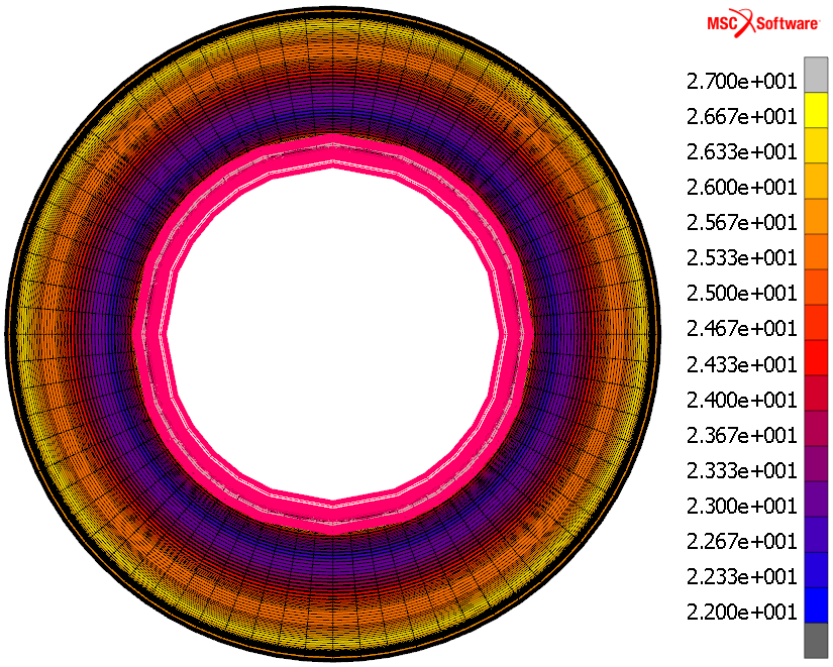

Figure 7.27: Temperature distribution (°C) on the sidewall of the numerical model for a load of 500 kg, inflation pressure of 300 kPa and rolling velocity of 60 km/h

The temperature distribution on the tread for the test was uniform, with a high temperature region in the middle (see Figure 7.24); whereas the temperature distribution of the numerical model only had the high temperature region in the middle of the tire (shown in Figure 7.29). The maximum temperatures for both cases were at the root of the grooves in the middle, with a temperature of 33,8 °C for the numerical model and 45 °C for the test. The non-uniform temperature distribution in the numerical model was due to the tire not deforming enough for the whole tread to be in contact with the cylinder. Therefore, the maximum deformation was where the tire was in contact with the cylinder and this led to the high temperature in the middle. The distribution of the temperatures on the tread compared better between the numerical model and the test, if the inflation pressure is increased to 450 kPa (see Figure 7.30). However, the temperatures in the numerical model were still lower, with a maximum temperature of 34,7 °C, compared to the 47,2 °C for the test. The distribution compared better in the latter case, noting the contact stress distribution of the numerical model and the test was almost the same.

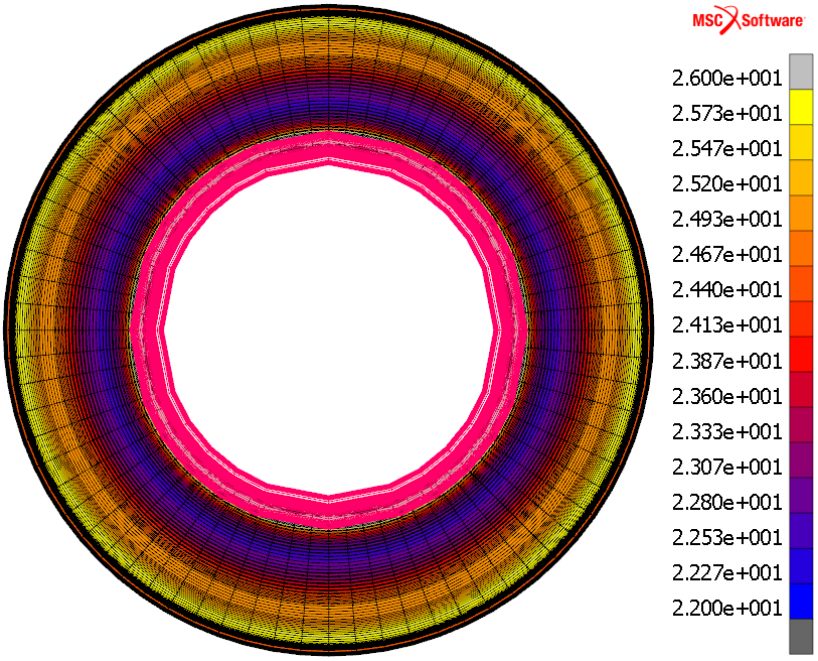

Figure 7.28: Temperature distribution (°C) on the sidewall of the numerical model for a load of 500 kg, inflation pressure of 450 kPa and rolling velocity of 60 km/h

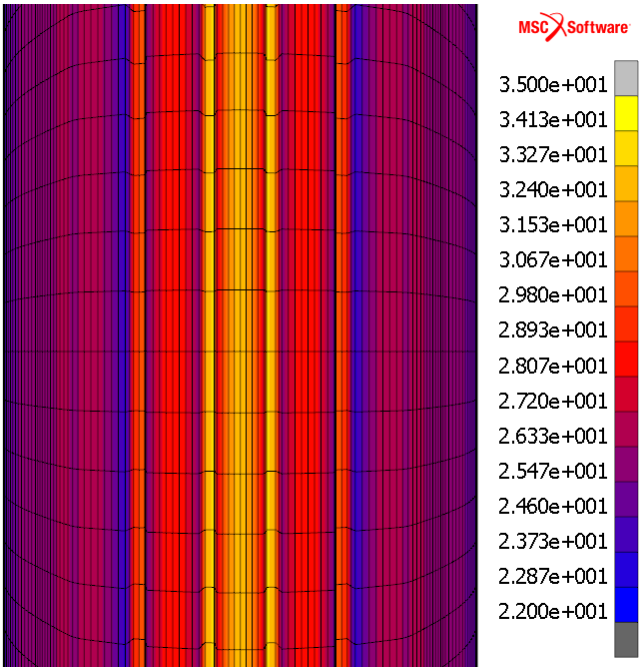

Figure 7.29: Temperature distribution (°C) on the tread of the numerical model for a load of 500 kg, inflation pressure of 300 kPa and rolling velocity of 60 km/h

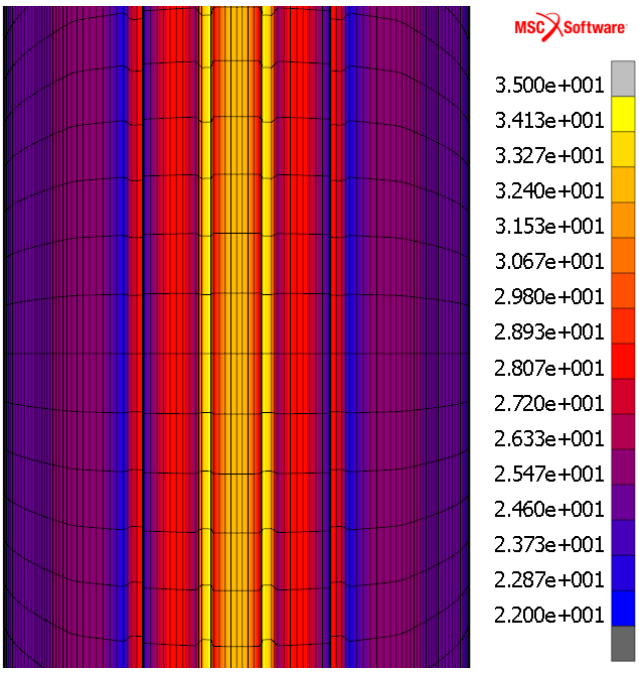

Figure 7.30: Temperature distribution (°C) on the tread of the numerical model for a load of 500 kg, inflation pressure of 450 kPa and rolling velocity of 60 km/h

7.4.5 Internal Surface Temperature Comparison

The temperatures measured on the internal surface of the tire by the thermocouples, were compared to the temperatures determined by the numerical model, along path A-B in Figure 6.16. The trend of the temperatures on the internal surface was the same for the numerical model and the measured results when a load of 500 kg, an inflation pressure of 300 kPa and a rolling velocity of 60 km/h was applied to the tire, as the plot in Figure 7.31 shows. However, the temperatures in the numerical model were lower, except in the middle of the tire, where the temperature of the numerical model was 49,5 °C and the temperature of the test 46 °C.

When the inflation pressure was increased to 450 kPa, the trend of the temperatures still compared well between the numerical model and the measured results. However, the temperatures in the numerical model were higher in this case, except on the sidewall. The comparison of the temperatures showed the sidewall of the numerical model was too stiff. In test one, the temperature on the sidewall in the numerical model was 29,2 °C and the measured temperature was 41,1 °C. The low temperature on the sidewall of the numerical model was due to the sidewall not deforming enough, which led to the elastic strain energy density in the sidewall being lower and ultimately resulted in a lower temperature.

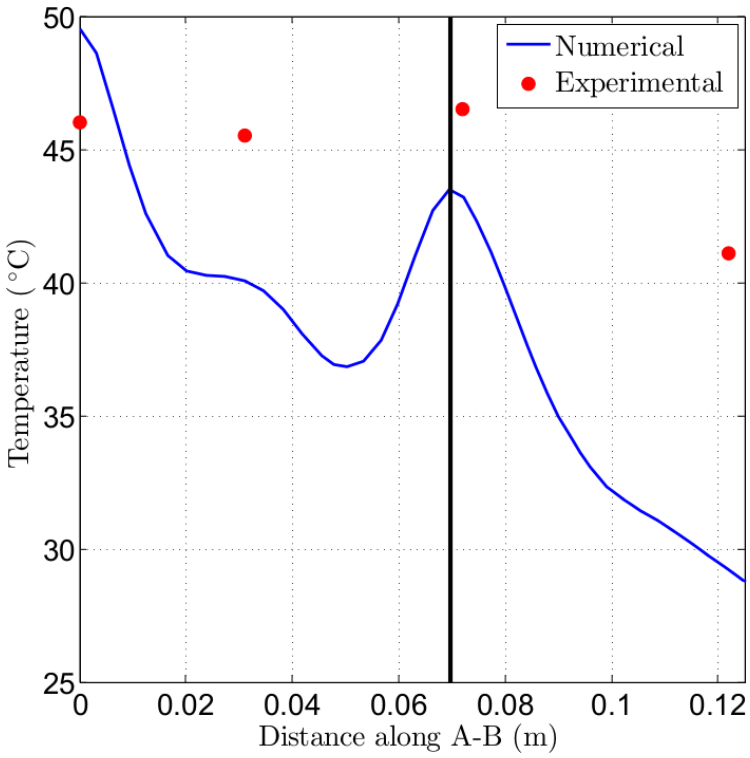

Figure 7.31: Plot of the numerical temperature distribution along line A-B and the measured temperatures for a load of 500 kg, inflation pressure of 300 kPa and rolling velocity of 60 km/h

7.5 Discussion of Comparisons

The comparison of the numerical model to the experimental tests done on the tire showed the numerical model did not capture the deformation and the contact stress distribution of the tire accurately enough. The results showed that the sidewall of the numerical model was too stiff throughout the comparisons of the data. Therefore, the rubber of the tread was too stiff for the sidewall and needed to be modelled by a different rubber, with less stiffness. Furthermore, the tread influenced the contact stress distribution due to the stiffness of the tread being too high. The material properties were gleaned from literature and may differ from the material properties used in the manufacturing of the tire.

The temperature comparison showed the sidewall stiffness did not influence the temperature in the tread region notably, but it would make a difference to the peak temperature in the middle of the tire and the temperature on the sidewall if the sidewall stiffness was lowered. The trends of the numerical and experimental data compared well, which showed that the material properties and modelling of the sidewall with the same rubber as the tread was what caused the difference in the results.

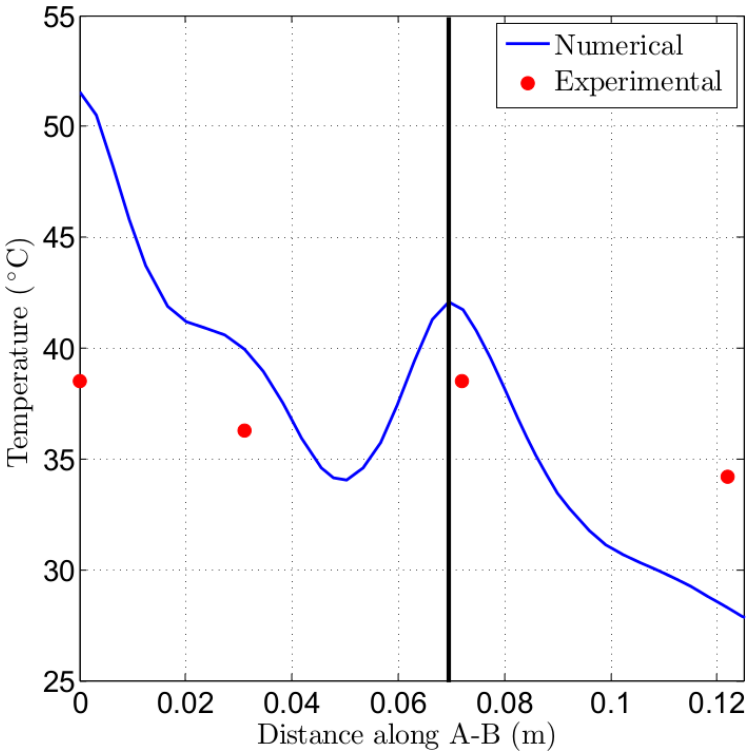

Figure 7.32: Plot of the numerical temperature distribution along line A-B and the measured temperatures for a load of 500 kg, inflation pressure of 450 kPa and rolling velocity of 60 km/h

7.6 Conclusion

This chapter compared the numerical data with experimental data from three tests in this chapter in order to validate the numerical model. The deformation of the tire was the first comparison and showed the numerical model deformed less than the measured deformation, but the shape of the deformation was the same. Next, the contact stress distribution was compared, where the contact area of the numerical model was smaller compared to the measured data, while the contact stress was higher. Lastly, the external and internal temperatures were compared. The temperature on the tread of the tire compared relatively well with the numerical model and the measured data, showing the same trends, although the values fluctuated slightly. The main reason for these differences was due to the sidewall and the tread being modelled with the same rubber and the material properties gleaned from literature and not from tests performed on the tire.

Chapter 8

Conclusion and Recommendations

8.1 Conclusion

The goal for this project was to develop a numerical model of a passenger vehicle tire using finite element analysis and validating the model with experimental data. The numerical model had to calculate the temperature distribution in the tire for different operating conditions, using material properties from literature. The operating conditions included: the load applied to the tire, inflation pressure of the tire, rolling velocity of the tire and the ambient temperature. The experimental data was generated under the same operating conditions as the numerical model.

Rubber, the main component of the tire, is a hyper-viscoelastic material and was modelled using the Mooney-Rivlin material model. Only one type of rubber was used in the numerical model. The body and steel belt plies were modelled using `Rebar` elements, which specified the rebar material, rebar area, number of rebar layers, number of rebars per length and the rebar orientation. The plies were placed inside the rubber elements using the `Insert` option in MSC.Marc. The wound-up bead wire was modelled as an isotropic material.

The rim and the cylinder, imitating the road surface, were modelled as rigid surfaces. The contact between the tire and the two rigid surfaces was modelled using the `Node To Segment` method, with the `Coulomb Bilinear (Displacement)` friction model.

Numerical modelling of the tire was divided into two steps, namely: dynamic rolling analysis and steady-state thermal analysis. In the dynamic rolling analysis the first step was to inflate the tire. After the tire was inflated, the next step was to apply the load on the inflated tire. Lastly, the loaded tire was rotated and the elastic strain energy density calculated. The heat generated due to the rolling of the tire was then calculated from the elastic strain energy density. In the thermal analysis the heat generated during the rolling was applied to determine the temperature distribution in the tire. This process was identified as the best way to generate the temperature

distribution.

The tire was inflated by a `Cavity Pressure Load`, while a `Cavity Mass Load` was used to keep the mass of the air inside the tire constant during the loading and rolling analysis. The cavity showed an increase in pressure when the load was applied due to the volume change. This volume change was, however, insignificant, due to the small deformation of the numerical model. The increase in pressure, due to the increase in air temperature, was not considered in this study.

Temperature results from the numerical model showed a temperature peak in the middle of the tread for this specific tread design. There was also a high temperature at the shoulder and the bead of the tire. When the inflation pressure of the tire was decreased and the load kept constant, the temperature increased. Furthermore, the temperature also increased when the load applied to the tire was increased and the inflation pressure held constant. Increasing the rolling velocity and ambient temperature increased the temperature when the load and inflation pressure was held constant. The rolling velocity of the tire and the ambient temperature influenced the maximum temperature in the tire the most, whereas the load and inflation pressure influenced the distribution of the temperature.

Comparison of the numerical data with the experimental data did not show good consistency. Deformation of the numerical model was considerably lower than the actual deformation of the tire. However, the shape of the deformation was the same. Furthermore, the contact stress area of the numerical model was smaller than the actual contact stress area, which led to the contact stress being higher in the numerical model. Comparison of the temperatures in the tread of the tire was consistent, however, the temperatures in the sidewall was considerably lower in the numerical model.

Comparison of the results showed that the sidewall could not be modelled with the same rubber as the tread. The rubber was too stiff, which decreased the deformation of the sidewall and also the temperature in the sidewall, due to less heat being generated. Furthermore, the steel belt plies over-stiffened the tread of the tire, which lead to the tread not being able to deform enough to distribute the load over the whole tread area. Therefore, tests need to be performed on the actual materials used in the construction of the tire in order to determine accurate material properties.

The numerical model was able to predict the temperature distribution in the tire geometry using material properties from literature under different operating conditions. However, the model was not able to predict the deformation and the contact stress distribution accurately enough. The temperature in the tread of the numerical model was predicted reasonably accurate, considering that material properties from literature were used. Therefore, the model can be used to determine the temperature distribution in the tire.

8.2 Recommendations

Rubber played an integral role in the numerical model results. Therefore, to get more accurate numerical results, the material properties of the rubber in the actual tire need to be determined. The different types of rubber and the location of the rubber in the tire geometry need to be identified in order to add them to the numerical model. Thereafter, the numerical model needs to be adapted to model all the different rubbers. The hysteresis coefficient used in this project also came from literature. The coefficient needs to be determined for all the different rubbers in the tire, using dynamical material analysis tests. The dynamical material analysis tests should be conducted under different strain rates to determine if the strain rate has an influence on the hysteresis coefficient.

The `Rebar` element and `Insert` option works well to model the body plies and steel belt plies in the tire. However, the material properties for the plies need to be determined from the materials used in the actual tire due to the material properties from literature being too stiff. The parameters used for the modelling of the `Rebar` element, which includes the ply area, number of ply layers, number of threads per length and the ply orientation need to be determined more accurately from the tire geometry.

The forced convection coefficients for the thermal analysis were calculated from a formula coming from literature. The formula needs to be validated or a new formula must be derived to calculate the convection coefficient as a function of rolling velocity using computational fluid dynamic (CFD). The thermal analysis of the tire can also be solved using a CFD analysis. The CFD analysis is able to model the air inside of the tire; therefore, more accurate temperature distribution can be determined.

Appendices

Appendix A

Calibration of Experimental Setup

Calibration of all the measurement devices on the tire test bench are described in this appendix. Specifications of the equipment used to calibrate the devices are summarised and the calibration curves and functions are shown.

A.1 Load Cell

The 2 t CNCELL PA6140W load cell on the test bench was calibrated using a 10 kN calibrated load cell, HBM Spider8 data acquisition system and catman® Easy software. The specifications for the CNCELL PA6140W load cell is shown in Table A.1 and the specifications for the HBM Spider8 is summarised in Table A.2.

Table A.1: CNCELL PA6140W load cell specifications

Load Rating (t)	2
Accuracy Class	0,03 C3
Nonlinearity	0,03 % Full Scale
Hysteretic	0,03 % Full Scale
Non-Repeatability	0,02 % Full Scale
Creep In 30 Minutes	0,03 % Full Scale

Table A.2: HBM Spider8 specifications

# Measuring Channels	4
Carrier Frequency (Hz)	4,8

First, the tire was removed from the test bench for the calibration of the load cell. Next, the calibrated load cell was bolted to the axis in order to measure the load on the tire, as shown in Figure A.1. A load was applied by the

mechanical screw in increments of 50 kg till 200 kg, thereafter the increments were increased to 100 kg till 800 kg. After each increment the logged file was saved and a new log file was started for the next increment. The calibration curve for the load cell is shown in Figure A.2 and the calibration function is shown in equation A.1.

$$m_l = 1,0063m_r + 13,2879 \tag{A.1}$$

where m_l is the load (kg) measured by the load cell and m_r is the real load (kg) on the tire.

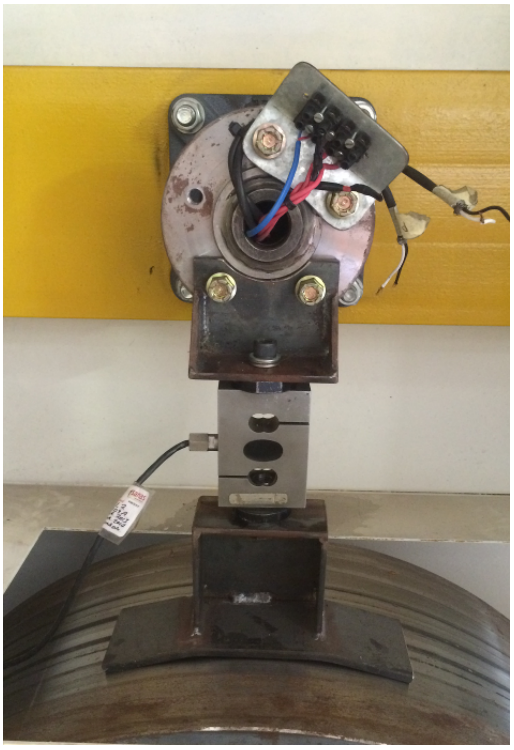

Figure A.1: Calibration setup for the load cell

A.2 Thermocouples

The thermocouples were calibrated using a Fluke 9142 field metrology well, Isotech 935-14-72 platinum resistance thermometer, HP 34401A multimeter and the systems that log the temperature data. The Fluke 9142 metrology well specification is shown in Table A.3. The calibration equation for the platinum resistance thermometer, to calculate the temperature (°C) from the resistance (Ω), is shown in equation A.2.

$$T = 0,00111611\Omega^2 + 2,32652102\Omega - 243,7648049 \tag{A.2}$$

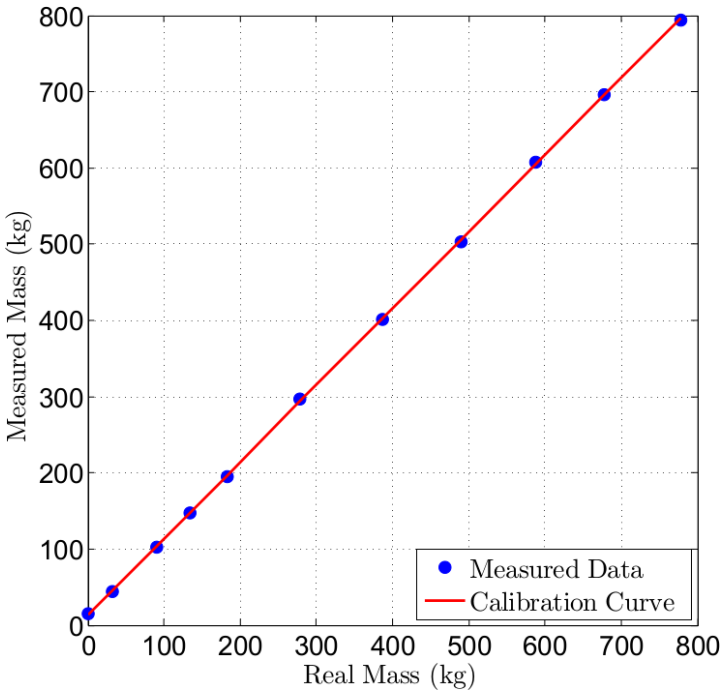

Figure A.2: Calibration curve for the load cell

Table A.3: Fluke 9142 metrology well specifications

Temperature Range at 23°C (°C)	-25 to 150
Display Accuracy (°C)	$\pm 0,2$ Full range
Stability (°C)	$\pm 0,01$ Full range

The platinum resistance thermometer was connected to the multimeter, with the 4-wire ohm function activated and placed inside the middle slot of the well insert. The thermocouples were then placed in the rest of the well insert slots. Next, the metrology well was set to a temperature of 25 °C and held there for 30 min for the temperature to stabilise. After that, the temperature was set to the first calibration value and again held there for 30 min for the temperature to stabilise. After the 30 min, the temperatures measured by the thermocouples was logged and the resistance value was collected. The steps were repeated for all the other calibration temperatures.

A.2.1 Air Flow Thermocouple

The temperature of the air flowing over the tire was measured using a WIKA TR10 RTD thermocouple assembly, with the specifications shown in Table A.4. The calibration curve for the air flow thermocouple is shown in Figure A.3 and the calibration function is shown in equation A.3.

$$T_t = 1,0124T_r - 0,4174 \tag{A.3}$$

where T_t is the temperature (°C) measured by the air flow thermocouple and T_r is the reference temperature (°C).

Table A.4: WIKA TR10 RTD thermocouple assembly specifications

Sensor Element	Pt100
Measuring Range (°C)	+5 to +50
Wiring Configuration	3 wire

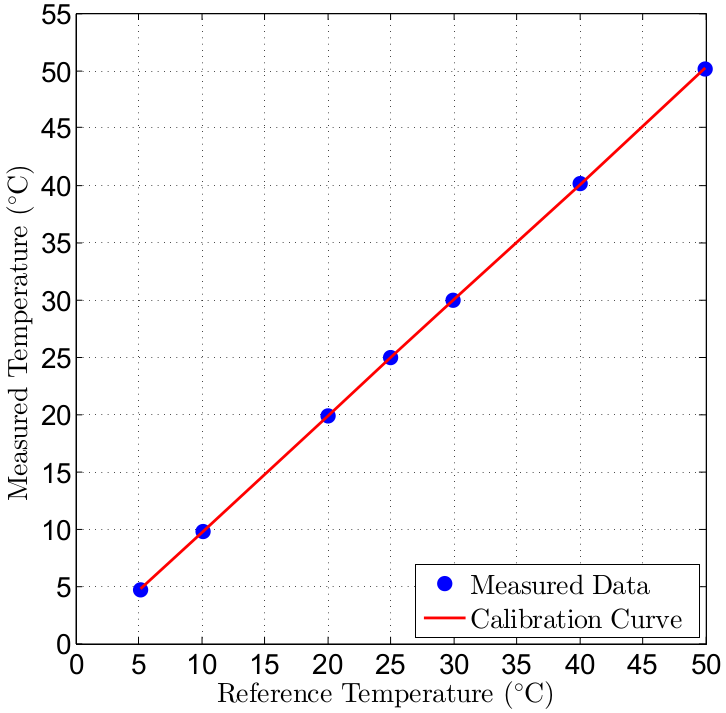

Figure A.3: Calibration curve for the air flow thermocouple

A.2.2 Inflation Air Thermocouple

The temperature of the air inside the tire was also measured using a WIKA TR10 RTD thermocouple assembly, with the specifications shown in Table A.4, only the measuring range change to, +5 to +150 °C. The calibration curve for the inflation air thermocouple is shown in Figure A.4 and the calibration function is shown in equation A.4.

$$T_t = 1,0114T_r - 1,2047 \tag{A.4}$$

where T_t is the temperature (°C) measured by the air flow thermocouple and T_r is the reference temperature (°C).

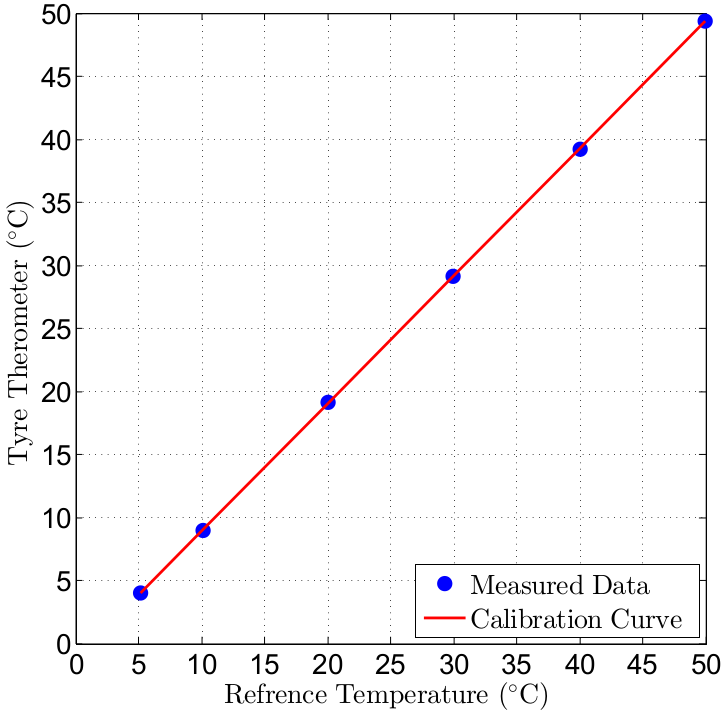

Figure A.4: Calibration curve for the thermocouple inside the tire

A.2.3 Tire Surface Thermocouples

To measure the temperature on the inside of the tire, type-T wire thermocouples were manufactured. Only the calibration curve for the first thermocouple is shown in Figure A.5. The rest of the calibration curves looks almost exactly the same. The calibration function of the nine thermocouples is shown in equation A.5, using constants for the curve fit parameters. The constants are summarised in Table A.5.

$$T_t = C_1 T_r - C_0 \tag{A.5}$$

where T_t is the temperature (°C) measured by the type-T wire thermocouple and T_r is the reference temperature (°C).

A.3 Differential Pressure Transmitter

The WIGA A2G-50 differential pressure transmitter was calibrated using a 500 Pa micro Betz Manometer. Specifications of the pressure transmitter are shown in Table A.6. One port of the Betz manometer and one port of the

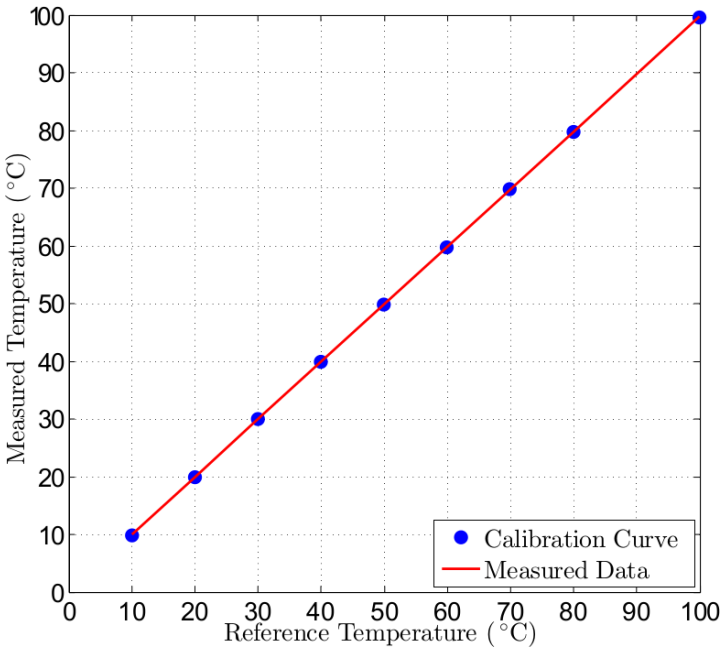

Figure A.5: Calibration curve for the first type-T wire thermocouple

Table A.5: Constants for the calibration curves of the type-T wire thermocouples

Thermocouple #	C_1	C_0
One	0,9975	-0,0015
Two	0,9978	-0,0403
Three	0,9972	0,0370
Four	0,9972	-0,0508
Five	0,9973	-0,0193
Six	1,0026	-0,1466
Seven	0,9943	0,0889
Eight	0,9937	0,1306
Nine	0,9958	-0,1331

pressure transmitter were open to ambient pressure. The other ports were connected to each other by a T-connector. A valve was connected to the last port of the T-connector. The valve was opened and the air sucked through it until the pressure of the Betz manometer was nearly 500 Pa. The valve was then closed and the pressure reading collected. The valve was then opened for the pressure to drop and then closed again. This was repeated until the pressure was zero. The calibration curve for the pressure transmitter is shown in Figure A.6 and the calibration function is shown in equationA.6.

$$P_t = 2,0068P_b - 1,8779 \tag{A.6}$$

where P_t is the Pressure (Pa) measured by the differential pressure transmitter and P_b is the Betz manometer pressure (Pa).

Table A.6: WIGA A2G-50 differential pressure transmitter specifications

Accuracy	±1,5 %
Measuring Range (Pa)	0 to 1000
Maximum Pressure (kPa)	25

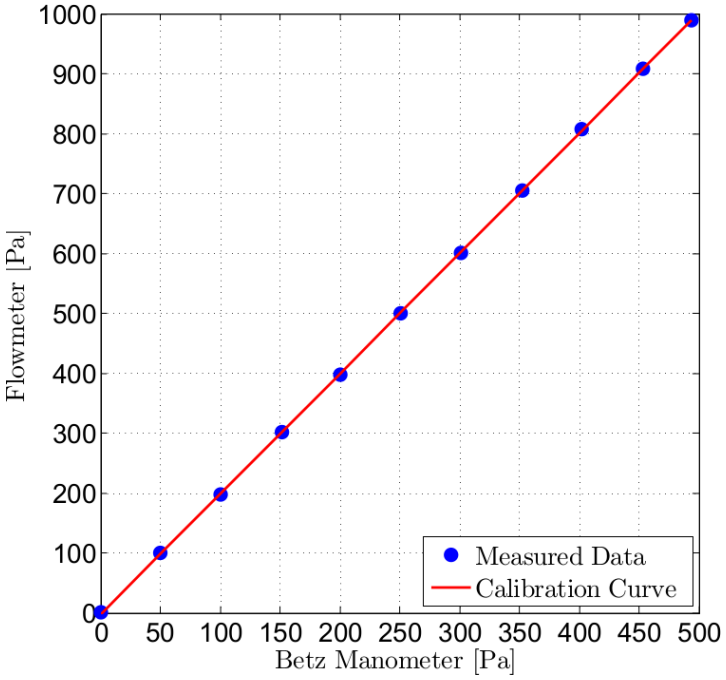

Figure A.6: Calibration curve for the differential pressure transmitter

A.4 Pressure Transmitter

The WIGA A-10 pressure transmitter was calibrated using a 1 000 kPa WIKA Master Gauge and a small bicycle pump. Specifications for the pressure transmitter is summarised in Table A.7 and for the Master Gauge in Table A.8. The pressure transmitter, Master Gauge and bicycle pump were connected to a T connector. The bicycle pump was used to increase the pressure in increments of 50 kPa, while the pressure is measured by the pressure transmitter and Master Gauge, to a maximum pressure of 500 kPa. Figure A.7 shows the calibration curve, while the calibration function is shown by equation A.7.

$$P_t = 0,9940P_m - 0,9955 \tag{A.7}$$

Where P_t is the Pressure (Pa) measured by the differential pressure transmitter and P_m is the Master Gauge pressure (Pa).

Table A.7: WIGA A-10 pressure transmitter specifications

Measuring Range (MPa)	0 to 1
Nonlinearity per BFSL	$\leq \pm 0,5$ % of span
Non-repeatability	$\leq 0,1$ % of span
Signal noise	$\leq \pm 0,3$ % of span

Table A.8: WIKA Master Gauge specifications

Measuring Range (kPa)	0 to 1 000
accuracy	0,3 %

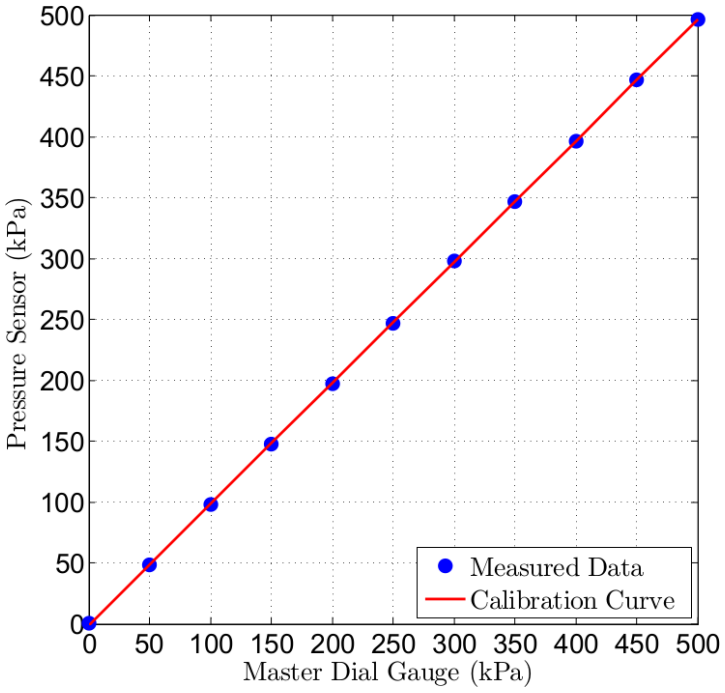

Figure A.7: Calibration curve for the pressure transmitter

List of References

Benoît, R., Lafrance, L., Malo, D. and Baron, J. (2009). Heavy vehicles tire blowout and explosion. Tech. Rep., IRSST and ASTE.

Chen, J.H., Chen, K.S. and Tong, L.Y. (2001). On the pyrolysis kinetics of scrap automotive tires. *Journal of Hazardous Materials*, vol. 84(1), pp. 43–55.

Cho, J.R., Lee, H.W., Jeong, W.B., Jeong, K.M. and Kim, K.W. (2013). Numerical estimation of rolling resistance and temperature distribution of 3-d periodic patterned tire. *International Journal of Solids and Structures*, vol. 50(1), pp. 86–96.

Dolez, P.I., Nohile, C., Ha Anh, T., Vu-Khanh, T., Benoît, R. and Bellavigna-Ladoux, O. (2008). Exploring the chemical aspects of truck tire blowouts and explosions. *Safety Science*, vol. 46(9), pp. 1334–1344.

Gent, A.N. and Walter, J.D. (2006). The pneumatic tire. Tech. Rep., National Highway Traffic Safety Administration.

Ghoreishy, M.H.R. (2008). A state of the art review of the finite element modelling of rolling tyres. *Iranian Polymer Journal*, vol. 17(8), pp. 571–597.

Ghoreishy, M.H.R., Firouzbakht, M. and Naderi, G. (2014). Parameter determination and experimental verification of bergström-boyce hysteresis model for rubber compounds reinforced by carbon black blends. *Materials and Design*, vol. 53, pp. 457–465.

Kelly, P.A. (2012). Solid Mechanics Part III: Foundations of Continuum Solid Mechanics [Online]. Available at: `http://homepages.engineering.auckland.ac.nz/${\sim}$pkel015/SolidMechanicsBooks/Part\_III/index.html` [2014, September 12].

Kováč, I. and Krmela, J. (2012). Fe analysis of automobile tire. In: *Advanced Research in Scientific Areas*, vol. 1, pp. 1809–1812.

LaVision (2014*a*). Digital Image Correlation [Online]. Available at: `http://www.lavision.de/en/techniques/digital-image-correlation.php` [2014, October 29].

LaVision (2014*b*). StrainMaster-Advanced Image based Tools for Optical Deformation and Strain Measurement [Online]. Available at: `http://www.lavision.de/en/download.php?id=323[2014,July22]`.

Lin, Y. and Hwang, S. (2004). Temperature prediction of rolling tires by computer simulation. *Mathematics and Computers in Simulation*, vol. 67(3), pp. 235–249.

Maxxis (2014). Maxxis Tire Diagram [Online]. Available at: `http://www.maxxistyres.com.au/images/pics/layered\_tyre.pdf` [2014, May 30].

MSC (2014). *Marc® 2014, Volume A: Theory and User Information*. MSC Software Co., Newport Beach, CA.

Nave, C.R. (2014). Friction and Automobile Tires [Online]. Available at: `http://hyperphysics.phy-astr.gsu.edu/hbase/mechanics/frictire.html` [2014, March 24].

PerkinElmer (2013). *Dynamic Mechanical Analysis (DMA)*. PerkinElmer, Waltham, MA.

Tang, T., Johnson, D., Smith, R.E. and Felicelli, S.D. (2014). Numerical evaluation of the temperature field of steady-state rolling tires. *Applied Mathematical Modelling*, vol. 38(5-6), pp. 1622–1637.

Tekscan (2009). *I-Scan®& High Speed I-Scan® User Manual*. Tekscan Inc., South Boston, MA.

Tekscan (2014). Sensor Model / Map: 5150N [Online]. Available at: `http://www.tekscan.com/5150N-pressure-sensor` [2014, July 04].